UNIVERSITÀ DEGLI STUDI DI TRIESTE

Sede Amministrativa del Dottorato di Ricerca

CHINESE ACADEMY OF SCIENCE, INSTITUTE OF GEOLOGY AND GEOPHYSICS

CHINESE EARTHQUAKE ADMINISTRATION, INSTITUTE OF GEOPHYSICS

Posto di dottorato attivato grazie al contributo del
Ministero dell'Istruzione, dell'Università e della Ricerca (MIUR) nell'ambito del progetto:
Advanced methodologies in the field of geophysics and geodynamics
Internationalization Program (D.M. 5 august 2004, n. 262, Art.23)
International University Cooperations, Program 2004-2006, Prot. II04A1CHC8

XXI CICLO DEL
DOTTORATO DI RICERCA IN
GEOFISICA DELLA LITOSFERA E GEODINAMICA

Deep structure beneath the Central-South Tibet crustal density modelling and azimuthal anisotropy variation inferred from Quasi-Love waves

Settore scientifico-disciplinare GEO/10

DOTTORANDO
SUFANG ZHANG

RESPONSABILE DOTTORATO DI RICERCA (Coordinatore)
PROF. *PETER SUHADOLC*
FIRMA: _____

RELATORE
PROF. *ZHONGJIE ZHANG (CAS)*
FIRMA: _____

SUPERVISORE
PROF. *GIULIANO PANZA*
FIRMA: _____

CORRELATORE
DR. *CARLA BRAITENBERG*
FIRMA: _____

ANNO ACCADEMICO 2008/2009

Acknowledgements

I am very grateful to many people who have helped me to complete this work, especially to those whom I regard as having been my main teachers in geophysics. I am particularly indebted to my adviser, Prof. Zhang Zhongjie, who accepted me to study the problem of the deep structure beneath Tibet at the Institute of Geology and Geophysics in the Chinese Academy of Sciences. His ideas about the theory and application of seismic anisotropy stimulated me to study surface wave propagation and the application of Quasi-Love wave.

I would like to thank very much Prof. G. F. Panza who invited me to study at the Department of Earth Science in the University of Trieste for over 10 months. In my stay, while supervising my work, he gave me many great ideas about the knowledge of geodynamics, also including the interaction of velocity, density, temperature and pressure. He provided me with significant comments about my work after monthly reporting which has improved my work greatly. He always tells me to be careful when researching.

I am appreciate very much Dr. Carla Braitenberg, Department of Earth Science, University of Trieste, who spared so many hours to teach me much about 3D gravity forward modeling and Moho undulation, geological setting in Tibet, and the importance of the relation between density and velocity of lithology. The study of crustal structure in Tibet from gravity modeling was developed under her supervision. She gave me advice that the final density model should consider the effect of lithosphere thickening and provided me the excellent ideas of evaluating the modeling results. I would also like to thank her efforts to improve the language and style of the manuscript of my monthly report. I am particularly grateful to Dr. Fabio Romanelli who helped me solve many practical things when I was in Trieste in the first days. He also spent so much time to explain everything about synthesizing seismograms to me thoroughly.

I appreciated very much my other teachers at the Department of Earth Science, University of Trieste, Dr. Franco Vaccari helped me using the synthetic seismograms package for flat earth and Dr. Mariangela Guidarelli taught me the knowledge about focal mechanism. All the graduate students in the seismology group of DST are thanked for their kindhearted help.

I particularly wish to thank all my colleagues at the Division of Tibetan Plateau, Institute of Geology and Geophysics, Chinese Academy of Sciences, for the pleasant working atmosphere in the group and for their critical comments on my work.

Finally, I would like to say many thanks to my family for their patience, and especially to my husband for his qualified assistance.

This project is supported by National Nature Science Foundation of China (40474034, 40721003). This work is also supported by Italian MIUR and University of Trieste in the framework of the Internationalization PhD Program (2004-2006): Advanced methodologies in the field of geophysics and geodynamics (Prot. II04A1CHC8) Coordinated by Giuliano F. Panza. Y. Wang and X. P. Ke from Institute of Geodesy and Geophysics, Chinese Academy of Sciences are appreciated for providing the gravity data. HansJürgen Götze and Sabine Schmidt are thanked for availability of IGMAS software and technical support.

Contents

Abstract

The area of the present study is the central part of southern Tibet. It consists of two accreted terranes, Lhasa and Himalaya terranes, which today record the deformation history that originated from the processes of collision between the Eurasia and India plates. Our study of the crust/mantle structure in terms of seismic velocity, density, anisotropy and petrologic composition are undoubtedly significant to deepen the understanding of the continent-continent collision and its dynamics.

This PhD thesis can be briefly summarized into four parts that are listed in the following. 1) In order to reveal the characteristics of the crust/mantle deformation that has been generated by the Indian/Eurasia collision in the southern Tibet plateau, we study the propagation of Quasi-Love (QL) waves. Our study is based on the results from numerical modeling, which proved that QL is sensitive to lateral variation of seismic anisotropy, rather than heterogeneity and other factors. The results we obtain from processing locally observed seismograms, reveal a West-East variation of crust/mantle deformation in each terrane of the plateau. 2) A 3D density model of central-south Tibet is produced by modeling the Bouguer gravity field using all existing constraints. 3) Integrating seismic velocity and density models of the crust in the Lhasa and Himalaya terranes, we infer crustal composition models in central and southern Tibet. 4) Combining crustal density, velocity and mineralogical composition models, some important issues, such as the Indian slab subduction angle, and the relationship between crustal density and earthquake occurrences are discussed.

Some results based on the gravity modeling are summarized as follows: 1) under the constraint of the geometrical structure defined by seismic data, a 3-D density model and Moho interface are proposed for central-south Tibet; 2) the lower crustal density, smaller than 3.2 g/cm^3, suggests the absence of eclogite or partial eclogitization due to delamination under the central-south Tibet; 3) seismicity is strong or weak in correspondence of the most negative Bouguer gravity anomaly, so there is not a relationship between them; 4) the composition of the lower crust,

determined after the temperature-pressure calibration of seismic P wave velocity, might be one or a mixture of: 1. amphibolite and greenschist facies basalt beneath the Qiangtang terrane; 2. gabbro-norite-troctolite and mafic granulite beneath the Lhasa terrane. When using the data set published by Rudnick & Fountain (1995), the composition of the middle crust turns out to be granulite facies and might be pelitic gneisses. Granulite facies used to be interpreted as residues of partial melting, which coincides with the previous study by Yang et al. (2002) on partial melting in the middle crust. Amphibolite facies are thought to be produced after delamination, when underplating works in the rebound of the lower crust and lithospheric mantle.

From the seismology study, I have made the following conclusions: 1) through numerical simulation of surface wave propagation in heterogeneous media, we find that amplitude and polarization of surface wave only change a little when considering heterogeneity and QL waves, generated by surface wave scattering, are caused by lateral variation of anisotropy. 2) QL waves have been identified from the seismograms of selected paths recorded by the Tibetan station CAD, and are utilized to determine the variation of the uppermost mantle anisotropy of the Tibetan plateau. The location of the azimuthal anisotropy gradient is estimated from the group velocities of Rayleigh wave, Love wave and QL wave. We find that a predominant south-north lateral variation of azimuthal anisotropy is located in correspondence of the Tanggula mountain, and a predominant east-west lateral variation of azimuthal anisotropy is found to the north of the Gandese mountain (near 85° E longitude and 30° N latitude) and near the Jinsha river fault (near 85° E longitude and 35° N latitude).

Chapter 1

Introduction

1.1 Motivations for this study

With the advent of the theories of continental drift and plate tectonics, it has become widely accepted that the Tibetan plateau is the product of the collision between the Indian subcontinent and the Eurasian continent and that this process of mountain building is still continuing today (Holmes, 1965; Dewey and Bird, 1970; Powell and Conaghan, 1973; Le Fort, 1975; Molnar et al., 1977). The Indian subcontinent is moving towards the Eurasian continent at a rate of 50 mm/yr (Minster and Jordan, 1978) with respect to the Eurasia plate. Owing to this ongoing tectonic evolution, the Tibet plateau has been an interesting area for geoscientists over a long time. The central-south Tibet is a key location to study the geodynamics of the Tibet plateau, as it comprises a record of the collision process. This dissertation will focus on the study of anisotropy of seismic velocity in the uppermost mantle and on the formulation of a crustal density model in central-south Tibet. The former subject will be treated by a seismological investigation and the latter by applying a gravity field inversion method.

1.1.1 Surface wave --seismology method

Park et al. (2002) have reviewed many studies of upper-mantle anisotropy and their relation to global plate motions, past and present. They have summarized four basic seismic wave characteristics that allow us to identify seismic anisotropy: direction-dependent travel time anomalies, shear-wave birefringence, surface-wave scattering, and direction-dependent conversion of compressional (P) to shear (S)

waves. Quasi-Love wave is one of the seismic phases caused by elastic anisotropy (Fig.1.1), which occurs due to the Love wave polarizing in not only the transverse component, but also in the vertical component.

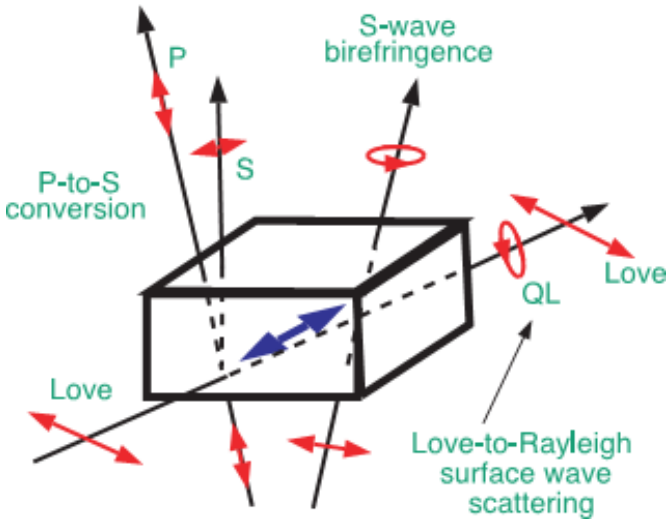

Fig.1.1 The illustration of birefringence and scattering effects caused by elastic anisotropy. Red arrows indicate rectilinear wave polarization. Red ellipses indicate elliptical wave polarization. (After Park et al., 2002)

He discovered The presence of quasi-Love waves on the vertical components of some long period records was discovered by Prof. Jeffrey Park (Yale University)[1] who explained them as effect of anisotropy (e.g., Park, 1996; Levin and Park, 1998). We adopt his remark "There are some examples where Love waves appear in the wrong component" and list the other reasons for which they can appear:

(1) Multipathing and path deviation. Lateral inhomogeneity of the Earth is responsible for many complications in surface wave propagation. One of them is the deviation of surface wave path from the shortest circle paths between the source and receiver. There are two techniques for detecting such deviations. One is based on measuring travel time delays of surface waves propagating across an array or a dense local network of seismic stations (e.g., Bungum and Capon, 1974). Another one is

[1] Levshin A L. Surface wave analysis and phenomenology. In 9th Workshop on Three-Dimensional Modelling of Seismic Waves Generation, Propagation and their Inversion. 22 September - 4 October, 2008

using three-component records to analyze polarization of surface waves (Lander, 1989; Paulssen et al., 1990; Levshin et al., 1992; Levshin et al., 1994; Laske, 1995). Effects of relatively smooth lateral inhomogeneity will manifest themselves in deviation of the vertical plane containing Rayleigh wave particle motion from the one passing through the great circle epicenter station. Particle motion in Love waves will be orthogonal to this new plane.

Besides deviations of the main train of surface waves from the shortest path we often observe another phenomenon, namely multipathing. Part of surface wave energy separates from the main train and propagates by its own way mostly tunneled by some laterally extended low velocity waveguide: the foredeep of some mountain range, a sedimentary basin, or the oceanic trench near the coast of a continent. It carries usually only a short-period part of the surface wave spectrum and by some (yet unclear) reason consists predominantly of Love waves (Levshin and Berteussen, 1979; Berteussen et al., 1983).

(2) Tectonic release. Theory predicts that Love waves as SH waves should not be observed in a laterally homogeneous Earth if the source is a center of dilatation or a vertical force.

I will study the lateral anisotropy variation by observing, collecting, and identifying QL waveforms, which propagate in the upper-mantle of Tibet.

1.1.2 Gravity modeling–potential field method

Detailed modeling of the present-day crustal structure is of paramount importance to understand the evolution of Tibet in the context of the Indian-Eurasian plate collision. The crustal layer can be constrained by field measurements and boreholes, which provide direct observations of the uppermost crust, while seismic techniques offer reliable data at greater depths, up to the crust-mantle boundary. Numerical modeling using the information provided by geophysical observables, such as elevation and gravity, is straightforward and is an effective procedure to improve our knowledge of the crust by modeling the crustal density structure.

The Earth's gravitational field gives us information about the 3D density variations within the planet. Thus, it provides valuable knowledge of the mass distribution at depths which together with other geophysical methods can be used to determine petrophysical and rheological properties.

Elevation reflects the average density of the lithospheric column under the assumption of local isostasy. Gravity anomalies depend on the inverse of the square of the distance to mass anomalies, whereas geoid anomalies diminish only inversely proportional to the distance. Hence, gravity anomalies are particularly sensitive to mass changes at crustal levels while the geoid anomaly is influenced by lateral density variations in a wider range of depths. Therefore, the second part of this thesis will focus on the modeling of gravity Bouguer anomaly data.

1.2 Outline

With the intention to understand the dynamics of the continental lithosphere at collision zones, this dissertation combines anisotropy of the uppermost mantle and the crustal density structure. In the first part of this dissertation, Chapter 2 deals with a study on the surface wave field and dynamic analysis for 3-D abnormal structure with homogeneous background velocity model. Based on the numerical experiment in Chapter 2 regarding the effect of small heterogeneities on surface wave propagation, QL waves, propagating in Lhasa Terrane and Qiangtang Terrane of Tibet, are studied in Chapter 3 in order to determine the lateral azimuthal anisotropy variation of the upper mantle.

In the second part, Chapter 4 provides a brief review of the composition of the lithosphere, concerning velocity, density, temperature and pressure. Chapter 5 presents gravity modeling results. The results obtained are discussed to explain the evolution of the Tibet region. Chapter 6 discusses seismicity and crustal composition based on Chapters 4 and 5.

Chapter 2

Effect of lateral heterogeneity of the structure on surface wave polarization

Abstract Modes coupling occurs between Love waves and Rayleigh waves under the condition of: 1) Coriolis force resulting from the earth rotation, 2) deviation from sphericity (earth ellipsoid); 3) lateral heterogeneity; 4) azimuthal anisotropy. This chapter will focus on studying how much each factor contributes to the surface wavefield. Among these four conditions, the former two factors have small relevance when the frequency is over 4.2 mHz, so this chapter will only discuss the effect on mode coupling of lateral heterogeneity, in order to determine whether lateral heterogeneity or azimuthal anisotropy contribute mostly to the mode coupling.

In addition to anisotropy, lateral heterogeneity of earth is another important factor affecting surface wave velocity. Based on the mode coupling and scattering theory of seismic wave propagation, amplitude and polarization anomalies are numerically computed when surface waves propagate in a simulated earth structure with lateral heterogeneous upper mantle. Surface wave propagation has been simulated for a wave incident with different periods, different back-azimuth by rotating the structure in the horizontal plane and different scales of heterogeneity, respectively. The numerical result of polarization anomalies of surface waves which is induced by lateral heterogeneity, suggests that the amplitudes and polarization anomalies of surface waves at short-period are more sensitive to lateral heterogeneity than at long-period. So we can conclude that mode coupling between Rayleigh waves and Love waves occurs on the transverse components in presence of lateral heterogeneity. Larger surface waves amplitude occurs at the boundary of lateral heterogeneity structure.

Keywords: Lateral heterogeneity, Surface wave, Polarization anomaly

2.1 Introduction

Van der Lee (1998) observed Rayleigh wave amplitude anomalies in North America that most probably arise from near-source scattering that may bias source parameter estimates. Laske et al. (1994) showed that polarization anomalies of Rayleigh waves at intermediate periods are more complex than in the long periods range. A careful analysis of their origin is necessary before they can be used, like the long-period ones, to improve the resolution of tomographic models.

These two examples illustrate the need to quantify the effect of different kinds of 3-D structures on surface wave propagation. They also indicate that a potential source of information lies in wavefield anomalies, which can become useful if appropriate data-analysis methods are developed.

Polarization anomalies of surface waves have been used to interpret the interior earth structure recently (Chen et al., 2005; 2006). In lateral homogeneous media, Rayleigh waves polarize in the vertical and radial direction and Love waves in the transverse direction. Although most observed fundamental mode surface waves follow this principle, polarization phenomena are not rare in many seismic surface wave records. That is to say, Rayleigh waves will also be recorded in the transverse component (quasi-Rayleigh waves), and Love waves also in the radial and vertical components (quasi-Love waves). The polarization anomalies of Love waves can be observed in seismograms more easily than quasi-Rayleigh waves.

There are three causes for the polarization phenomenon: 1) heterogeneity; 2) anisotropy; 3) deviation from the great circle path in laterally heterogeneous media. In order to study the scattering and coupling caused by lateral heterogeneity, amplitude and polarization of surface waves are calculated based on mode summation and scattering theory. Several numerical experiments are designed to study the polarization of surface waves in this study.

Surface wave propagation in 2-D Cartesian structures has been studied more extensively than in 3-D structures (Kennett, 1998). In 3-D structures, surface wave scattering was first studied by Snieder (1986). His formula, based on Born scattering

and the far-field approximation, is suitable to study the effect of small heterogeneities located far away from source and receiver, but invalid to study the effect of heterogeneities in the vicinity of a receiver. A more complete method which can cope with the near field and strong heterogeneity was developed by Bostock (1991) and Bostock & Kennett (1992). In this method, the model is composed of blocks with complex shapes. The fact that the structure inside each block must be laterally homogeneous in order to support a single set of local modes is the main limitation of this method. In addition, for complex 3-D structures, a large number of blocks have to be defined and their wavefields must interact with each other, which leads to heavy computations.

A multiple forward scattering formula was presented by Friederich et al. (1993). This method can calculate surface wave propagation in any 3-D structure in a very effective way. Maupin (2001) presented a very general scheme to synthesize surface waves propagating in 3-D Cartesian structures. It is based on multiple scattering and can simulate surface wavefield in 3-D isotropic and anisotropic structures embedded in a laterally homogeneous reference structure. It is similar to the multiple forward scattering method presented by Friederich et al. (1993). The main differences are that the former focuses on amplitude and polarization anomalies, and therefore multiple scattering is calculated in all directions. The mode coupling, especially between Rayleigh and Love waves, is emphasized in Maupin's method. His expressions satisfy the boundary conditions at tilted interfaces. Based on Maupin's theory, the specific features associated with propagation of surface waves in isotropic and lateral heterogeneous 3-D structures are examined in this study.

2.2 Modeling theory of surface wave propagation based on mode summation and scattering theory

Maupin's method (2001) has been used to model the propagation of surface waves in 3-D isotropic heterogeneous Cartesian structures. It is assumed that the

background structure is laterally homogeneous and that the heterogeneity acts as a secondary source producing multiple scattering and coupling between the surface wave modes of the background structure. This method was developed based on the same formulation used by Friederich et al. (1993). The structure is separated into a reference homogeneous structure and heterogeneity superimposed on the background structure. The wavefield is expressed as a sum of modes and amplitude and phase of each mode in the horizontal plane are described using potential field.

In 3-D structure, the elastic wave equation can be expressed as following (Maupin, 2001)

$$(-\partial_j C_{ijkl}\partial_l - \rho\omega^2\delta_{ik})u_k = f_i \text{ ,} \qquad (2.1)$$

Where u is the displacement, f stands for the source function, C_{ijkl} is the elastic module. Considering heterogeneity as a secondary source, it generates multiple scattering and mode coupling to the unperturbed wavefield. The structure is divided into reference model and perturbed model. So we have $C_{ijkl} = C^0_{ijkl} + \varepsilon\gamma_{ijkl}, \rho = \rho^0 + \delta\rho,$ where γ_{ijkl} , $\delta\rho$ are the perturbed parts of the elastic coefficient and density, respectively. ρ^0 and C^0_{ijkl} are parameters in the reference model. ε is a variable factor on the strength of heterogeneity.

We can rewrite Eq. (2.1)as

$$(-\partial_j C^0_{ijkl}\partial_l - \rho^0\omega^2\delta_{ik})u_k = -(-\partial_j(\varepsilon\gamma_{ijkl}\partial_l) - \varepsilon\delta\rho\omega^2\delta_{ik})u_k + f_i, \qquad (2.2)$$

when applying multiple scattering to wave propagation (Liu et al., 2000), and setting boundary condition (which is suitable for layered boundary and perturbed model): $[u_i] = 0$, $[n_j C_{ijkl}\partial_l u_k] = 0$, the p-order scattering displacement wavefield can be expressed as

$$u^{(p)}_q(X) = \int(-\partial_{j'} G_{qi}(X, X'))(\gamma_{ijkl}(X')\partial_{l'} + \delta\rho(X')\omega^2\delta_{ik})u^{(p-1)}_k(X')dX', \qquad (2.3)$$

where X is the coordinate of the observation point, X' is the coordinate of the scattering point. 0-order scattering wavefield can be thought as the wavefield in the reference model, and then

$$u_q^{(0)}(X) = \int G_{qi}(X, X^{'}) f_j(X^{'}) dX^{'}, \tag{2.4}$$

Eq. (2.4) is obtained from retaining first order terms in Eq. (2.3) and stands for Born approximation wavefield.

Green function for surface waves is given by (Takeuchi et al., 1972)

$$G_{qi}(X, X^{'}) = \sum_m Z_q^m(z) g_i^m(x, y, X^{'}), \tag{2.5}$$

where

$$Z_q^m(z) = \begin{pmatrix} 1/k_m(-V^m(z)\partial/\partial x + W^m(z)\partial/\partial y) \\ 1/k_m(-W^m(z)\partial/\partial x + V^m(z)\partial/\partial y) \\ U^m(z) \end{pmatrix}, \tag{2.6}$$

$$g_i^m(x, y, X^{'}) = \frac{-i}{8 c_m u_m J_1^m} Z_i^m(z^{'}) H_0^{(2)}(k_m R), \tag{2.7}$$

U^m 、 V^m are eigenfunction of the m-order higher Rayleigh mode. W^m is the eigenfunction of m-order higher Love mode. k_m、 c_m、 u_m、 J_1^m are wavenumber, phase velocity, group velocity and energy integral, respectively. R is the distance between X and $X^{'}$. $H_0^{(2)}$ is 0-order secondary Hankel function.

Insert Eq. (2.5) to Eq. (2.3), the p-order scattering wavefield can be expressed as multiple modes summation:

$$u_i^{(p)}(X) = \sum_m Z_i^m(z) \Phi_m^{(p)}(x, y), \tag{2.8}$$

using the advantage of mode summation (Snieder, 1986; Friederich et al., 1998), m-order higher mode and p-order scattering potential function $\Phi_m^{(p)}(x, y)$ can be written iteratively as

$$\Phi_m^{(p)}(x, y) = \sum_n \int K_{mn}(x, y; x', y') \Phi_n^{(p-1)}(x', y') dx' dy', \tag{2.9}$$

where

$$K_{mn}(x, y; x', y') = \int (-\partial_{j'} g_i^m(x, y; x^{'})) \times (\gamma_{ijkl}(x^{'}) \partial_{l'} + \delta\rho(x^{'}) \varpi^2 \delta_{ik}) Z_k^n(z^{'}) dz' \tag{2.10}$$

is coupling coefficient between Rayleigh wave and Love wave. Its physical meaning is that the energy of mode n and m transfers from point (x', y') to point (x, y).

In the case of isotropic heterogeneity, the potential function of mode m scattering at order p, the term of $\Phi_m^{(p)}(x,y)$ can be written as:

$$\begin{aligned}\Phi_m^{(p)}(x,y) &= \Phi_{m,2\phi,RR}^{(p)}(x,y)+\Phi_{m,2\phi,LL}^{(p)}(x,y)+\Phi_{m,2\phi,LR}^{(p)}(x,y)+\Phi_{m,2\phi,RL}^{(p)}(x,y)\\ &+\Phi_{m,\phi,RR}^{(p)}(x,y)+\Phi_{m,\phi,LL}^{(p)}(x,y)+\Phi_{m,\phi,LR}^{(p)}(x,y)+\Phi_{m,\phi,RL}^{(p)}(x,y)\\ &+\Phi_{m,const,RR}^{(p)}(x,y)\end{aligned} \qquad (2.10)$$

where $\Phi_{m,2\phi}^{(p)}(x,y)$、$\Phi_{m,\phi}^{(p)}(x,y)$ and $\Phi_{m,const}^{(p)}(x,y)$ contain the term of 2ϕ、ϕ and constant (only non zero elements are listed). Expressions for Rayleigh-to-Rayleigh coupling are (Maupin, 2001):

$$
\begin{aligned}
&\Phi^{(p)}_{m,2\phi,RR}(x,y)\\
&=\frac{-i}{8c_m u_m J_1^m}\int_S H_2^{(2)}(k_m R)\sin(2\phi)\sum_n \frac{k_m}{k_n}\\
&\times\{-\int V^m \gamma_{1112} V^n dz' \frac{\partial^2 \Phi_n^{(p-1)}(x',y')}{\partial^2_{x'^2}}\\
&-\int 2V^m \gamma_{1212} V^n dz' \frac{\partial^2 \Phi_n^{(p-1)}(x',y')}{\partial^2_{x'y'}}\\
&-\int V^m \gamma_{2212} V^n dz' \frac{\partial^2 \Phi_n^{(p-1)}(x',y')}{\partial^2_{y'^2}}\\
&+\int V^m \gamma_{1213} \widetilde{U}^n k_n dz' \frac{\partial \Phi_n^{(p-1)}(x',y')}{\partial x'}\\
&+\int V^m \gamma_{1223} \widetilde{U}^n k_n dz' \frac{\partial \Phi_n^{(p-1)}(x',y')}{\partial y'}\\
&+\int V^m \gamma_{1233} \frac{\partial U^n}{\partial z'} k_n dz' \Phi_n^{(p-1)}(x',y')\}dx'dy'\\
&+\frac{-i}{8c_m u_m J_1^m}\int_S H_2^{(2)}(k_m R)\cos(2\phi)\sum_n \frac{k_m}{k_n}\\
&\times\{\int V^m(\gamma_{1122}-\gamma_{1111})V^n dz' \frac{\partial^2 \Phi_n^{(p-1)}(x',y')}{\partial^2_{x'^2}}\\
&+\int V^m(\gamma_{2212}-\gamma_{1112})V^n dz' \frac{\partial^2 \Phi_n^{(p-1)}(x',y')}{\partial^2_{x'y'}}\\
&-\int \frac{1}{2}V^m(\gamma_{2222}-\gamma_{1122})V^n dz' \frac{\partial^2 \Phi_n^{(p-1)}(x',y')}{\partial^2_{y'^2}}\\
&+\int \frac{1}{2}V^m(\gamma_{1113}-\gamma_{2213})\widetilde{U}^n k_n dz' \frac{\partial \Phi_n^{(p-1)}(x',y')}{\partial x'}\\
&+\int \frac{1}{2}V^m(\gamma_{1123}-\gamma_{2223})\widetilde{U}^n k_n dz' \frac{\partial \Phi_n^{(p-1)}(x',y')}{\partial y'}\\
&+\int \frac{1}{2}V^m(\gamma_{1133}-\gamma_{2233})\frac{\partial U^n}{\partial z'} k_n dz' \Phi_n^{(p-1)}(x',y')\}dx'dy' \qquad (2.11)
\end{aligned}
$$

$$
\begin{aligned}
&\Phi^{(p)}_{m,\phi,RR}(x,y)\\
&=\frac{-i}{8c_m u_m J_1^m}\int_S H_1^{(2)}(k_m R)\sin(\phi)\sum_n \frac{k_m}{k_n}\\
&\times\{\int \widetilde{U}^m \gamma_{1123} V^n dz' \frac{\partial^2 \Phi_n^{(p-1)}(x',y')}{\partial_{x'^2}^2}\\
&+\int 2\widetilde{U}^m \gamma_{1223} V^n dz' \frac{\partial^2 \Phi_n^{(p-1)}(x',y')}{\partial_{x'y'}^2}\\
&+\int \widetilde{U}^m \gamma_{2223} V^n dz' \frac{\partial^2 \Phi_n^{(p-1)}(x',y')}{\partial_{y'^2}^2}\\
&-\int \widetilde{U}^m \gamma_{1323} \widetilde{U}^n k_n dz' \frac{\partial \Phi_n^{(p-1)}(x',y')}{\partial x'}\\
&-\int (\widetilde{U}^m \gamma_{2323} \widetilde{U}^n k_n - \delta\rho\varpi^2 \frac{1}{k_m} V^m V^n) dz' \frac{\partial \Phi_n^{(p-1)}(x',y')}{\partial y'}\\
&-\int \widetilde{U}^m \gamma_{3323} \frac{\partial U^n}{\partial z'} k_n dz' \Phi_n^{(p-1)}(x',y')\} dx' dy'\\
&+\frac{-i}{8c_m u_m J_1^m}\int_S H_1^{(2)}(k_m R)\cos(\phi)\sum_n \frac{k_m}{k_n}\\
&\times\{\int \widetilde{U}^m \gamma_{1113} V^n dz' \frac{\partial^2 \Phi_n^{(p-1)}(x',y')}{\partial_{x'^2}^2}\\
&+\int 2\widetilde{U}^m \gamma_{1213} V^n dz' \frac{\partial^2 \Phi_n^{(p-1)}(x',y')}{\partial_{x'y'}^2}\\
&+\int \widetilde{U}^m \gamma_{2213} V^n dz' \frac{\partial^2 \Phi_n^{(p-1)}(x',y')}{\partial_{y'^2}^2}\\
&-\int (\widetilde{U}^m \gamma_{1313} \widetilde{U}^n k_n - \delta\rho\varpi^2 \frac{1}{k_m} V^m V^n) dz' \frac{\partial \Phi_n^{(p-1)}(x',y')}{\partial x'}\\
&-\int \widetilde{U}^m \gamma_{1323} \widetilde{U}^n k_n dz' \frac{\partial \Phi_n^{(p-1)}(x',y')}{\partial y'}\\
&-\int \widetilde{U}^m \gamma_{3313} \frac{\partial U^n}{\partial z'} k_n dz' \Phi_n^{(p-1)}(x',y')\} dx' dy'
\end{aligned}
\qquad (2.12)
$$

$$
\begin{aligned}
&\Phi^{(p)}_{m,const,RR}(x,y)\\
&=\frac{-i}{8c_m u_m J_1^m}\int_S H_0^{(2)}(k_m R)\sum_n \frac{k_m}{k_n}\\
&\times\{\int[\frac{1}{2}V^m(\gamma_{1122}+\gamma_{1111})V^n+\frac{1}{k_m}\frac{\partial U^m}{\partial z'}\gamma_{1133}V^n]dz'\frac{\partial^2\Phi_n^{(p-1)}(x',y')}{\partial^2_{x'^2}}\\
&+\int[V^m(\gamma_{2212}+\gamma_{1112})V^n+\frac{2}{k_m}\frac{\partial U^m}{\partial z'}\gamma_{3312}V^n]dz'\frac{\partial^2\Phi_n^{(p-1)}(x',y')}{\partial^2_{x'y'}}\\
&+\int[\frac{1}{2}V^m(\gamma_{2222}+\gamma_{1122})V^n+\frac{1}{k_m}\frac{\partial U^m}{\partial z'}\gamma_{2233}V^n]dz'\frac{\partial^2\Phi_n^{(p-1)}(x',y')}{\partial^2_{y'^2}}\\
&-\int[\frac{1}{2}V^m(\gamma_{1113}+\gamma_{2213})+\frac{1}{k_m}\frac{\partial U^m}{\partial z'}\gamma_{3313}]\widetilde{U}^n k_n dz'\frac{\partial\Phi_n^{(p-1)}(x',y')}{\partial x'}\\
&-\int[\frac{1}{2}V^m(\gamma_{1123}+\gamma_{2223})+\frac{1}{k_m}\frac{\partial U^m}{\partial z'}\gamma_{3323}]\widetilde{U}^n k_n dz'\frac{\partial\Phi_n^{(p-1)}(x',y')}{\partial y'}\\
&-\int[\frac{1}{2}V^m(\gamma_{1133}+\gamma_{2233})\frac{\partial U^n}{\partial z'}k_n+\frac{1}{k_m}\frac{\partial U^m}{\partial z'}\gamma_{3333}\frac{\partial U^n}{\partial z'}k_n-\delta\rho\varpi^2\frac{k_n}{k_m}U^m U^n]dz'\Phi_n^{(p-1)}(x',y')\}dx'dy'
\end{aligned}
$$

（2.13）

Love-to-Love coupling：

$$
\begin{aligned}
&\Phi^{(p)}_{m,2\phi,LL}(x,y)\\
&=\frac{-i}{8c_m u_m J_1^m}\int_S H_2^{(2)}(k_m R)\sin(2\phi)\sum_n \frac{k_m}{k_n}\\
&\times\{\int\frac{1}{2}W^m(\gamma_{1112}-\gamma_{2212})W^n dz'\frac{\partial^2\Phi_n^{(p-1)}(x',y')}{\partial^2_{x'^2}}\\
&+\int\frac{1}{2}W^m(-\gamma_{1111}-\gamma_{2222}+2\gamma_{1122})W^n dz'\frac{\partial^2\Phi_n^{(p-1)}(x',y')}{\partial^2_{x'y'}}\\
&+\int\frac{1}{2}W^m(\gamma_{2212}-\gamma_{1112})W^n dz'\frac{\partial^2\Phi_n^{(p-1)}(x',y')}{\partial^2_{y'^2}}\\
&+\int\frac{1}{2}W^m(\gamma_{1123}-\gamma_{2223})\frac{\partial W^n}{\partial z'}dz'\frac{\partial\Phi_n^{(p-1)}(x',y')}{\partial x'}\\
&+\int\frac{1}{2}W^m(\gamma_{2213}-\gamma_{1113})\frac{\partial W^n}{\partial z'}dz'\frac{\partial\Phi_n^{(p-1)}(x',y')}{\partial y'}\}dx'dy'\\
&+\frac{-i}{8c_m u_m J_1^m}\int_S H_2^{(2)}(k_m R)\cos(2\phi)\sum_n \frac{k_m}{k_n}\\
&\times\{-\int\frac{1}{2}W^m\gamma_{1212}W^n dz'\frac{\partial^2\Phi_n^{(p-1)}(x',y')}{\partial^2_{x'^2}}\\
&+\int W^m(\gamma_{1112}-\gamma_{2212})W^n dz'\frac{\partial^2\Phi_n^{(p-1)}(x',y')}{\partial^2_{x'y'}}\\
&+\int W^m\gamma_{1212}W^n dz'\frac{\partial^2\Phi_n^{(p-1)}(x',y')}{\partial^2_{y'^2}}\\
&-\int W^m\gamma_{1223}\frac{\partial W^n}{\partial z'}dz'\frac{\partial\Phi_n^{(p-1)}(x',y')}{\partial x'}\\
&+\int W^m\gamma_{1213}\frac{\partial W^n}{\partial z'}dz'\frac{\partial\Phi_n^{(p-1)}(x',y')}{\partial y'}\}dx'dy'
\end{aligned}
\qquad (2.14)
$$

$$
\begin{aligned}
&\Phi_{m,\phi,LL}^{(p)}(x,y)\\
&=\frac{-i}{8c_m u_m J_1^m}\int_S H_1^{(2)}(k_m R)\sin(\phi)\sum_n \frac{k_m}{k_n}\\
&\times\{\int \frac{1}{k_m}\frac{\partial W^m}{\partial z'}\gamma_{1213}W^n dz'\frac{\partial^2\Phi_n^{(p-1)}(x',y')}{\partial_{x'^2}^2}\\
&+\int \frac{1}{k_m}\frac{\partial W^m}{\partial z'}(\gamma_{2213}-\gamma_{1113})W^n dz'\frac{\partial^2\Phi_n^{(p-1)}(x',y')}{\partial_{x'y'}^2}\\
&-\int \frac{1}{k_m}\frac{\partial W^m}{\partial z'}\gamma_{1213}W^n dz'\frac{\partial^2\Phi_n^{(p-1)}(x',y')}{\partial_{y'^2}^2}\\
&+\int \frac{1}{k_m}\frac{\partial W^m}{\partial z'}\gamma_{1323}\frac{\partial W^n}{\partial z'}dz'\frac{\partial\Phi_n^{(p-1)}(x',y')}{\partial x'}\\
&-\int (\frac{1}{k_m}\frac{\partial W^m}{\partial z'}\gamma_{1313}\frac{\partial W^n}{\partial z'}-\delta\rho\varpi^2\frac{1}{k_m}W^m W^n)dz'\frac{\partial\Phi_n^{(p-1)}(x',y')}{\partial y'}\}dx'dy'\\
&+\frac{-i}{8c_m u_m J_1^m}\int_S H_1^{(2)}(k_m R)\cos(\phi)\sum_n \frac{k_m}{k_n}\\
&\times\{-\int \frac{1}{k_m}\frac{\partial W^m}{\partial z'}\gamma_{1223}W^n dz'\frac{\partial^2\Phi_n^{(p-1)}(x',y')}{\partial_{x'^2}^2}\\
&+\int \frac{1}{k_m}\frac{\partial W^m}{\partial z'}(\gamma_{1123}-\gamma_{2223})W^n dz'\frac{\partial^2\Phi_n^{(p-1)}(x',y')}{\partial_{x'y'}^2}\\
&+\int \frac{1}{k_m}\frac{\partial W^m}{\partial z'}\gamma_{1223}W^n dz'\frac{\partial^2\Phi_n^{(p-1)}(x',y')}{\partial_{y'^2}^2}\\
&-\int (\frac{1}{k_m}\frac{\partial W^m}{\partial z'}\gamma_{2323}\frac{\partial W^n}{\partial z'}-\delta\rho\varpi^2\frac{1}{k_m}W^m W^n)dz'\frac{\partial\Phi_n^{(p-1)}(x',y')}{\partial x'}\\
&+\int \frac{1}{k_m}\frac{\partial W^m}{\partial z'}\gamma_{1323}\frac{\partial W^n}{\partial z'}dz'\frac{\partial\Phi_n^{(p-1)}(x',y')}{\partial y'}\}dx'dy'
\end{aligned}
\qquad (2.15)
$$

Rayleigh-to-Love coupling:

$$
\begin{aligned}
&\Phi^{(p)}_{m,2\phi,RL}(x,y)\\
&=\frac{-i}{8c_m u_m J_1^m}\int_S H_2^{(2)}(k_m R)\sin(2\phi)\sum_n \frac{k_m}{k_n}\\
&\times\{\int \frac{1}{2}W^m(\gamma_{1111}-\gamma_{1122})V^n dz'\frac{\partial^2\Phi_n^{(p-1)}(x',y')}{\partial^2_{x'^2}}\\
&+\int W^m(\gamma_{1112}-\gamma_{2212})V^n dz'\frac{\partial^2\Phi_n^{(p-1)}(x',y')}{\partial^2_{x'y'}}\\
&+\int \frac{1}{2}W^m(\gamma_{1122}-\gamma_{2222})V^n dz'\frac{\partial^2\Phi_n^{(p-1)}(x',y')}{\partial^2_{y'^2}}\\
&+\int \frac{1}{2}W^m(\gamma_{2213}-\gamma_{1113})\widetilde{U}^n k_n dz'\frac{\partial\Phi_n^{(p-1)}(x',y')}{\partial x'}\\
&+\int \frac{1}{2}W^m(\gamma_{2223}-\gamma_{1123})\widetilde{U}^n k_n dz'\frac{\partial\Phi_n^{(p-1)}(x',y')}{\partial y'}\\
&+\int \frac{1}{2}W^m(\gamma_{2233}-\gamma_{1133})\frac{\partial U^n}{\partial z'}k_n dz'\Phi_n^{(p-1)}(x',y')\}dx'dy' \qquad (2.16)
\end{aligned}
$$

The term of $\sin(\phi)$ in the potential of $\Phi^{(p)}_m(x,y)$:

$$
\begin{aligned}
&\Phi^{(p)}_{m,\phi,RL}(x,y)\\
&=\frac{-i}{8c_m u_m J_1^m}\int_S H_1^{(2)}(k_m R)\sin(\phi)\sum_n \frac{k_m}{k_n}\\
&\times\{\int \frac{1}{k_m}\frac{\partial W^m}{\partial z'}\gamma_{1113}V^n dz'\frac{\partial^2\Phi_n^{(p-1)}(x',y')}{\partial^2_{x'^2}}\\
&+\int \frac{2}{k_m}\frac{\partial W^m}{\partial z'}\gamma_{1213}V^n dz'\frac{\partial^2\Phi_n^{(p-1)}(x',y')}{\partial^2_{x'y'}}\\
&+\int \frac{1}{k_m}\frac{\partial W^m}{\partial z'}\gamma_{2213}V^n dz'\frac{\partial^2\Phi_n^{(p-1)}(x',y')}{\partial^2_{y'^2}}\\
&-\int (\frac{1}{k_m}\frac{\partial W^m}{\partial z'}\gamma_{1313}\widetilde{U}^n k_n+\delta\rho\varpi^2\frac{1}{k_m}W^m V^n)dz'\frac{\partial\Phi_n^{(p-1)}(x',y')}{\partial x'}\\
&-\int \frac{1}{k_m}\frac{\partial W^m}{\partial z'}\gamma_{1323}\widetilde{U}^n k_n dz'\frac{\partial\Phi_n^{(p-1)}(x',y')}{\partial y'}\\
&-\int \frac{1}{k_m}\frac{\partial W^m}{\partial z'}\gamma_{3313}\frac{\partial U^n}{\partial z'}k_n dz'\Phi_n^{(p-1)}(x',y')\}dx'dy' \qquad (2.17)
\end{aligned}
$$

Love-to-Rayleigh coupling:

$$
\begin{aligned}
&\Phi^{(p)}_{m,2\phi,LR}(x,y)\\
&=\frac{-i}{8c_m u_m J_1^m}\int_S H_2^{(2)}(k_m R)\sin(2\phi)\sum_n \frac{k_m}{k_n}\\
&\times\{-\int V^m \gamma_{1212} W^n dz' \frac{\partial^2 \Phi_n^{(p-1)}(x',y')}{\partial_{x'^2}^2}\\
&+\int V^m(\gamma_{1112}-\gamma_{2212}) W^n dz' \frac{\partial^2 \Phi_n^{(p-1)}(x',y')}{\partial_{x'y'}^2}\\
&+\int V^m \gamma_{1212} W^n dz' \frac{\partial^2 \Phi_n^{(p-1)}(x',y')}{\partial_{y'^2}^2}\\
&-\int V^m \gamma_{1223} \frac{\partial W^n}{\partial z'} dz' \frac{\partial \Phi_n^{(p-1)}(x',y')}{\partial x'}\\
&+\int V^m \gamma_{1213} \frac{\partial W^n}{\partial z'} dz' \frac{\partial \Phi_n^{(p-1)}(x',y')}{\partial y'}\}dx'dy'
\end{aligned}
\qquad (2.18)
$$

$$
\begin{aligned}
&\Phi^{(p)}_{m,\phi,LR}(x,y)\\
&=\frac{-i}{8c_m u_m J_1^m}\int_S H_1^{(2)}(k_m R)\sin(\phi)\sum_n \frac{k_m}{k_n}\\
&\times\{\int \widetilde{U}^m \gamma_{1223} W^n dz' \frac{\partial^2 \Phi_n^{(p-1)}(x',y')}{\partial_{x'^2}^2}\\
&+\int \widetilde{U}^m(\gamma_{2223}-\gamma_{1123}) W^n dz' \frac{\partial^2 \Phi_n^{(p-1)}(x',y')}{\partial_{x'y'}^2}\\
&-\int \widetilde{U}^m \gamma_{1223} W^n dz' \frac{\partial^2 \Phi_n^{(p-1)}(x',y')}{\partial_{y'^2}^2}\\
&+\int (\widetilde{U}^m \gamma_{2323} \frac{\partial W^n}{\partial z'} + \delta\rho\varpi^2 \frac{1}{k_m} V^m W^n) dz' \frac{\partial \Phi_n^{(p-1)}(x',y')}{\partial x'}\\
&-\int \widetilde{U}^m \gamma_{1323} \frac{\partial W^n}{\partial z'} dz' \frac{\partial \Phi_n^{(p-1)}(x',y')}{\partial y'}\}dx'dy'
\end{aligned}
\qquad (2.19)
$$

where $\widetilde{U}^m = U^m - (1/k_m)(\partial V^m/\partial z')$, $\widetilde{U}^n = U^n - (1/k_n)(\partial V^n/\partial z')$; ϕ is the azimuth of (x,y) as seen from (x',y'), counted positively clockwise from the x-direction; H is Hankel function.

Concerning the azimuthal variation of the scattering, Rayleigh-Love and Love-Rayleigh coupling have azimuthal dependence on $\sin(2\phi)$ and $\sin(\phi)$ only. Therefore, the expressions for Rayleigh-Love and Love-Rayleigh coupling are different with respect Rayleigh-Rayleigh or Love-Love coupling. After calculating the coupling coefficients between all the modes, then the surface wavefield of lateral heterogeneous structure can be simulated.

2.3 Polarization anomalies in laterally heterogeneous structures

Reference velocity and density models are shown in Fig. 2.1. Shear wave velocities come from surface wave diffraction tomography and Monte-Carlo inversion result of LSA block in Tibet. In addition, shear wave velocities derived from deep seismic sounding (Zhang et al., 2002, 2005) in LSA block are also considered. P-wave velocities and densities are calculated from shear wave velocities ($Vp= 1.7684Vs+0.2482$, $\rho = 1.8377Vp^{0.03625}*Vs^{0.2981}$). Polarization anomalies for surface wave propagation are modeled with the following two steps: 1) compute each mode's eigen functions in the background model firstly. 2) compute displacements of the three components of motion using mode coupling and boundary integral equation method.

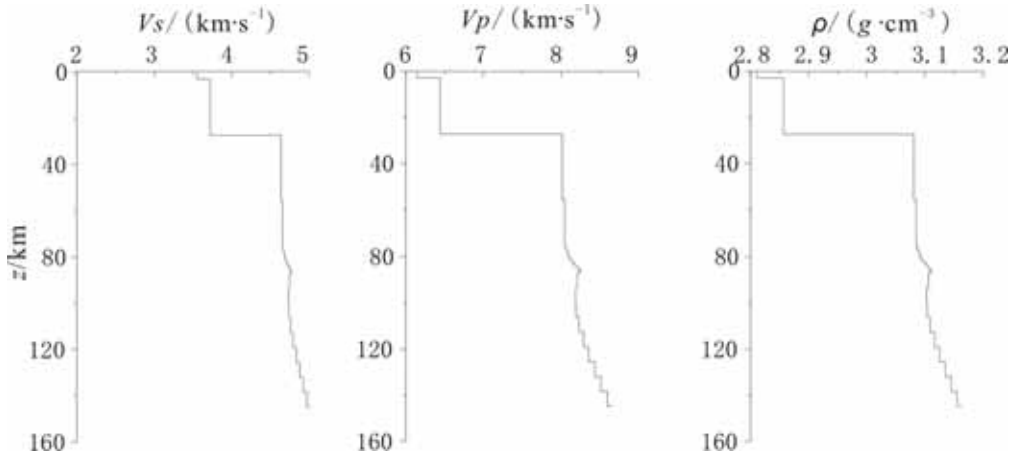

Fig.2.1 Velocity and density model for the background structure. Shear wave velocities is from the surface wave diffracted tomography and Monte-Carlo inversion model and deep seismic sounding data for Lhasa block in Tibet. P wave velocities and densities are transformed from shear wave velocities.

The 3D heterogeneous velocity model (Fig.2.2) is made up of a reference velocity model and a perturbation velocity model. In the perturbation velocity model velocities decrease with depth and have a maximum value of 10% shear wave velocity in the reference velocity model. The size of this heterogeneous area is 400 km × 300 km × 40 km from the depth of 60 km to 100 km. The size of the grid size is 20 km × 20 km. Since the heterogeneity scale is smaller than the wave length, in order to obtain the exact solution of the wave equation, multiple scattering theory will be used in modeling surface wave propagation.

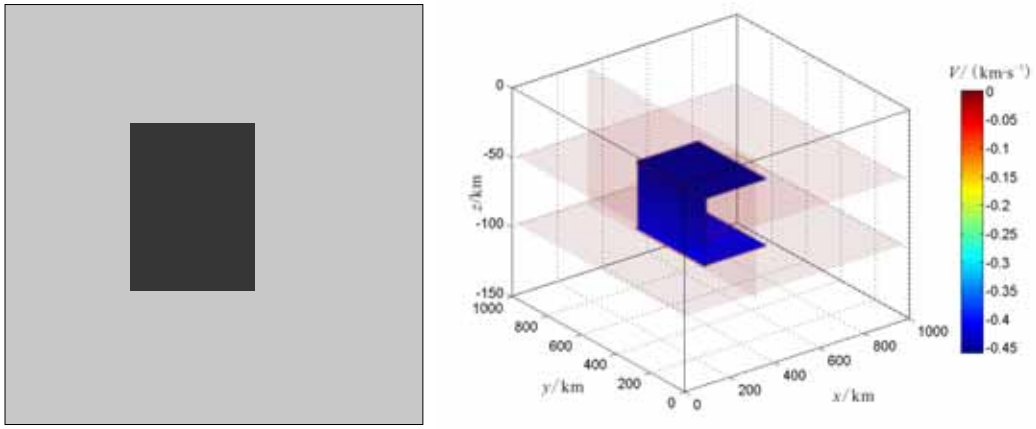

（a） （b）

Fig.2.2 (a) Velocity model is shown in the horizontal plane. Gray stands for reference velocity model, black square shows the perturbation area. (b) Graph of the 3D lateral heterogeneity structure. Blue cube shows the perturbation velocity model. The size of this heterogeneous area is 400 km×300 km×40 km from a depth of 60 km to 100 km.

The solution of the wavefield converges well after iterating three times. Fig.2.3 represents the radial displacement (a) and the transverse displacement (b) with incident wave of period 50s fundamental mode Rayleigh wave. The energy of the radial component is larger than that of the transverse component. It implies that the motion of surface wave depends on the direction of wave propagation; the amplitude is small in the transverse component. Displacements of the decomposed modes for the radial component with incident wave of period 50s fundamental Rayleigh wave is shown in Fig.2.4. Fundamental mode displacement contributes more to radial component than higher modes.

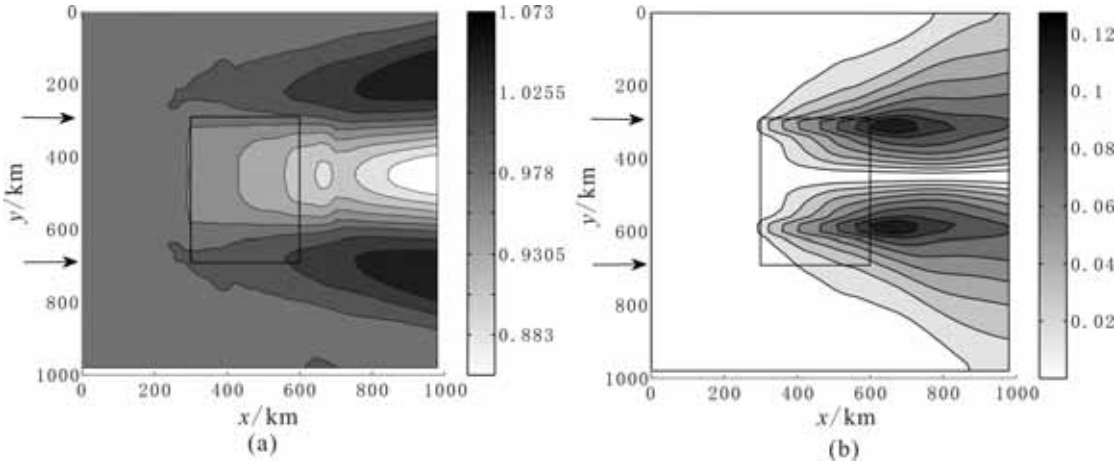

Fig.2.3 Radial component (a) and transverse component (b) of total wavefield for fundamental mode Rayleigh wave with 50 s incident period. The energy of radial component is larger than that of the transverse component.

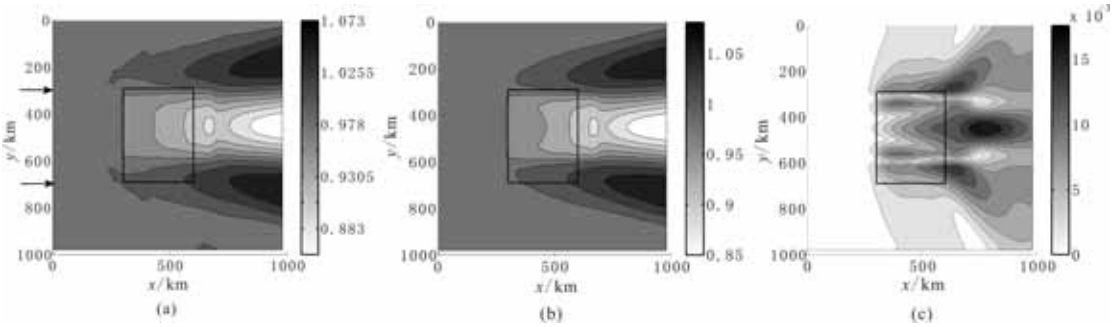

Fig.2.4 Displacements of decomposed modes of Radial component (a) fundamental mode Rayleigh wave with 50 s incident period. (b) Radial component only contains fundamental mode. (c) Radial component only contains higher modes. Fundamental mode contributes more to radial component than higher modes.

2.4 The effects on surface wave propagation of frequency, incidence angle and heterogeneity scale

2.4.1 Different frequency of incident wave

As shown in table 2.1, when the period of the incident wave decreases to 35 s, the transition energy of radial and transverse component grows. Exactly speaking, radial component varies by 6% and transverse component varies by 50%. When the period further decreases to 25 s, the transition energy continues to increase. As to the radial

component, the variation is 9%. The energy of the transverse component is two times the energy at 50 s period. Fig.2.5 is same as Fig.2.3 for displacements with incident wave of 25 s period fundamental mode Rayleigh wave.

Table 2.1 Maximum amplitudes for models with different physical parameters

Heterogeneity scale（km）	Period（s）	Incident angle（°）	Max. amplitude of radial component	Max. amplitude of transverse component
300×400	50	0	1.073	0.1275
	35	0	1.137	0.184
	25	0	1.1696	0.2844
		15	1.1563	0.301
		30	1.1603	0.297
200×300	50	0	1.02	0.093
	35	0	1.101	0.125
	25	0	1.135	0.252
		15	1.1164	0.2446
		30	1.142	0.258

When increasing the frequency of incident wave, the amplitude of the radial component changes a little. However, amplitude of transverse component varies significantly. As a result, the ellipticity of particle motion has a notable change.

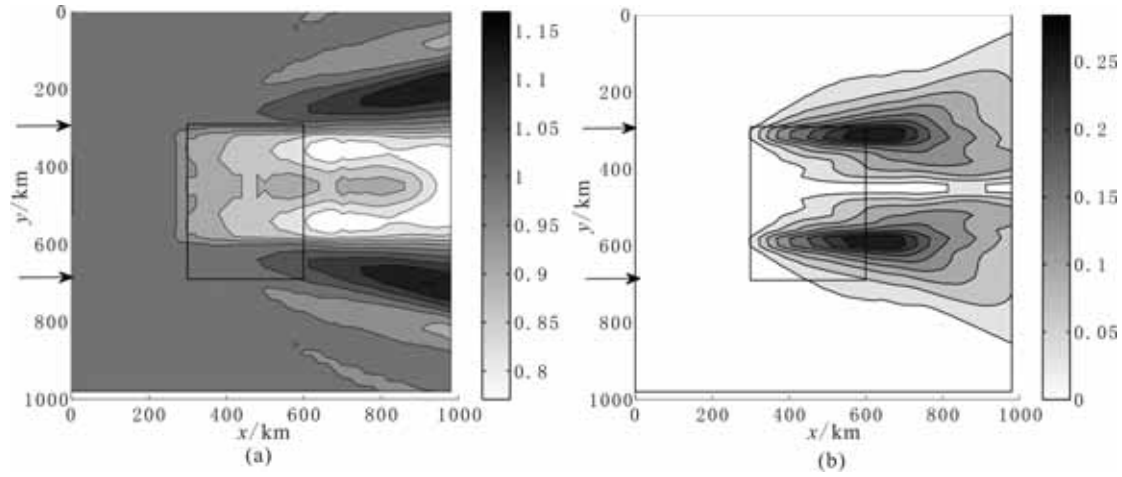

Fig.2.5 Radial component (a) and transverse component (b) of total wavefield for fundamental mode Rayleigh wave with 25 s period.

2.4.2 Different angle of incident wave

The amplitudes of the two horizontal components change by 1% under the variation of incident angle. Fig.2.6 is same as Fig.2.3 for displacements but for incident wave with 25 s period fundamental mode Rayleigh wave and 15° backazimuth. Likewise, when the angle of the incident wave is 30°, transition energies of radial and transverse components have little change.

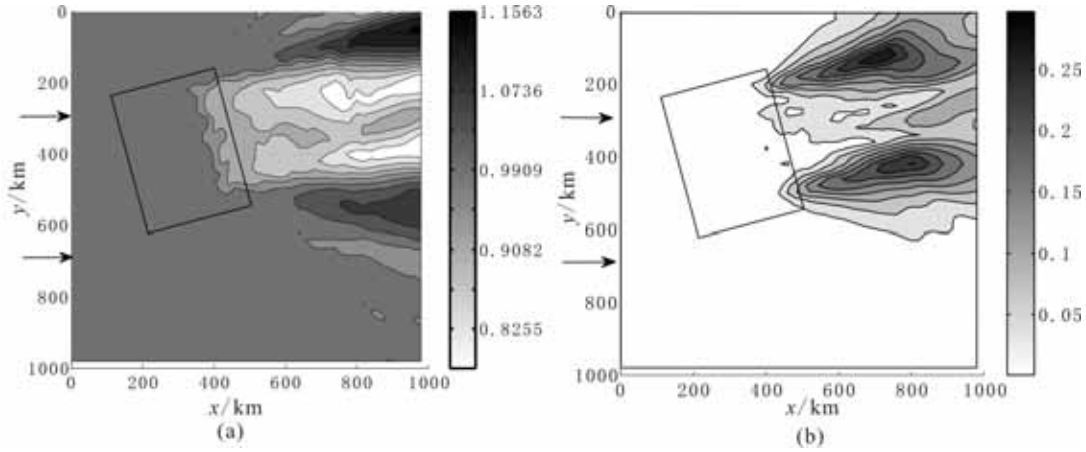

Fig.2.6 Radial component (a) and transverse component (b) of total wavefield for fundamental mode Rayleigh wave with 25 s period and 15° backazimuth incident.

2.4.3 Different heterogeneity scale

In order to analyse the effect on the wavefield of the size of heterogeneity, we have designed model 2, where length and width of the heterogeneity domain are decreased by 100 km. Fig.2.7 is the same as Fig.2.3 for displacements with incident wave of period 25 s fundamental mode Rayleigh wave and small scale lateral heterogeneity. As seen from Fig.2.7, in the case of same period and angle of incident wave, maximum amplitudes decrease from 1.1696 for large size of heterogeneity to 1.1164 for small size heterogeneity. That is to say, it varies by 5%.

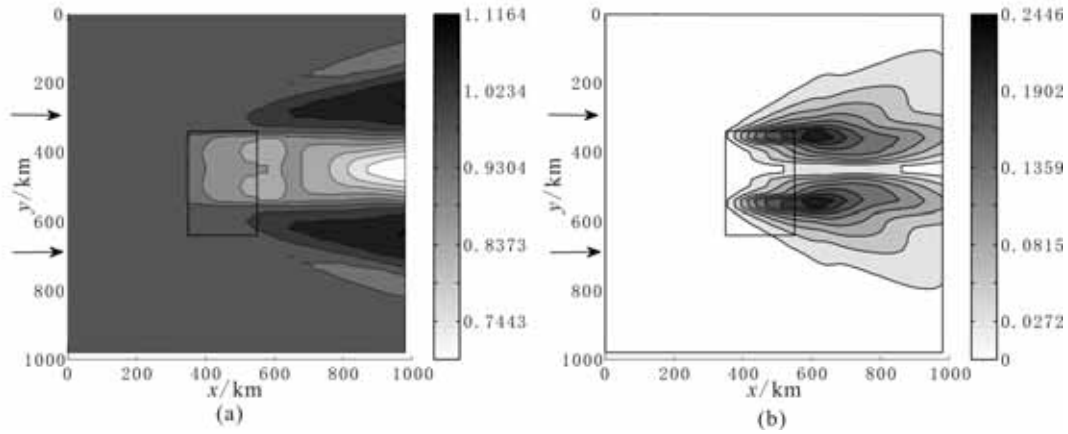

Fig.2.7 Radial component (a) and transverse component (b) of total wavefield for fundamental mode Rayleigh wave with 25 s period incident, but for small scale lateral heterogeneity.

In addition, through the numerical simulation of two horizontal components, we can detect the front of the heterogeneity zone from the position where the amplitude of the transverse component begins to increase. Meanwhile, the size of the heterogeneity zone can be found from the position of the maximum amplitude in the radial component.

Fig.2.8 shows the polarization in the horizontal plane under four different conditions. By comparing the four sets of partical motion, we find that shorter period incident wave has stronger polarization. Polarization anomaly distributes in and behind the heterogeneity domain. Although amplitude variation is small under different incident angles, particle motion changes a lot. From the above analysis, we can conclude that amplitude and polarization of surface waves can be used to determine the size of the heterogeneity zone.

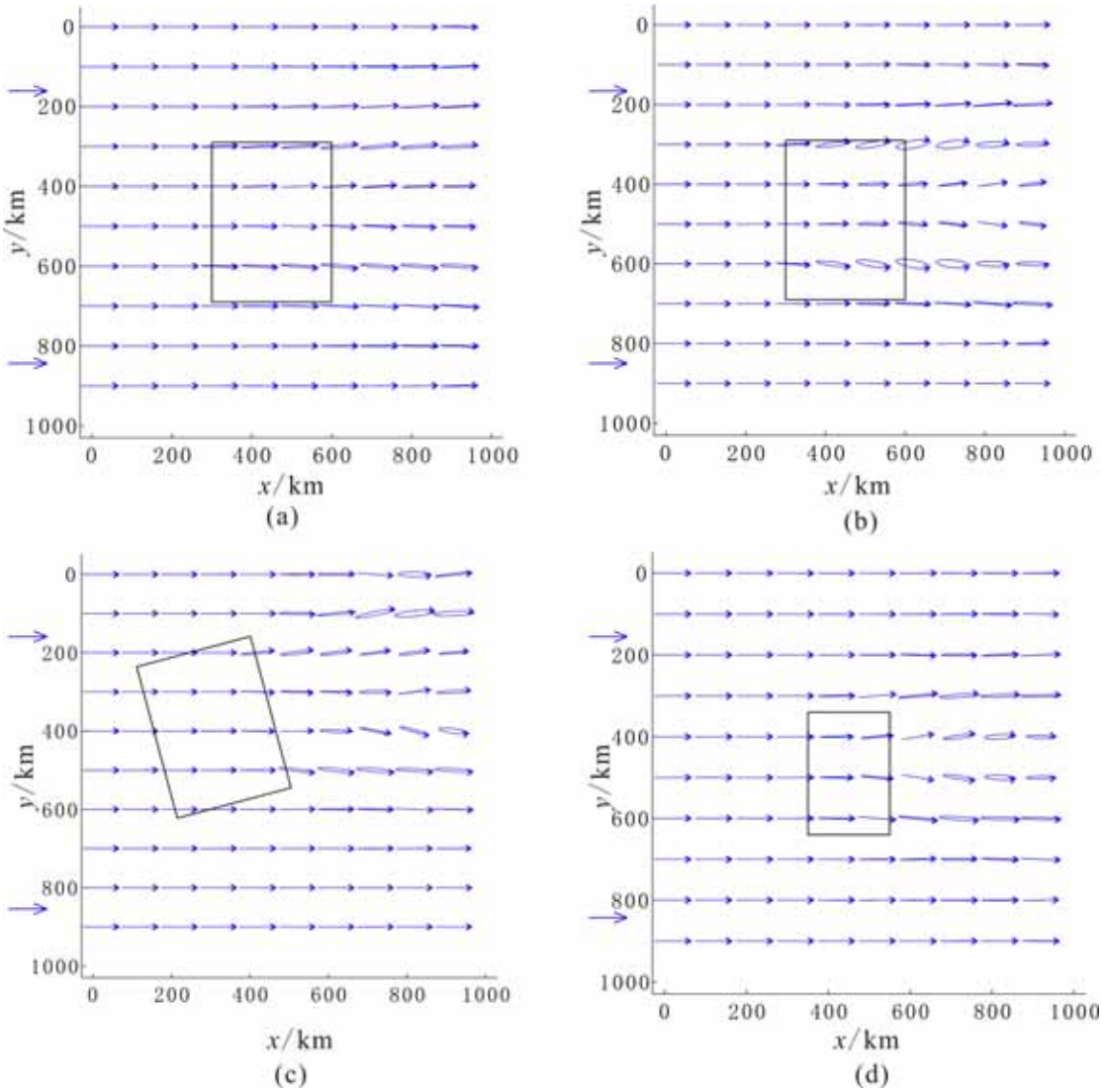

Fig.2.8 Polarization in the horizontal plane under four different conditions. (a) The incident fundamental mode Rayleigh wave with 50 s period; (b) The incident fundamental mode Rayleigh wave with 25 s period; (c) The incident fundamental mode Rayleigh wave with 25 s period and 15° backazimuth; (d) The incident fundamental mode Rayleigh wave with 25 s period and small scale lateral heterogeneity.

2.5 Conclusions

Through modeling the displacements of three components for surface waves, we reach the following conclusions:

1) When making fundamental mode Rayleigh wave as incident wave, the seismogram records fundamental mode Rayleigh wave in the radial component. The shorter the period of the incident surface wave, the stronger the energy of the

wavefield it generates. We can infer that the degree of mode coupling is stronger when incidented at shorter period than at longer period. Amplitude is hardly affected by different backazimuths, but polarization anomaly is affected significantly.

2) The transverse component contains Rayleigh-Love coupled modes. However, their amplitude is very small. We infer that isotropic heterogeneity has weak effect on the polarization anomaly.

3）Max amplitude exists at the boundary of the perturbation area in the heterogeneous velocity model. Particle motion shows ellipse trace in the horizontal plane, which infers that quasi-surface wave generate. Amplitude has positive relationship with size of heterogeneity structure.

As can be seen from the results of modeling surface waves in isotropic heterogeneity in this work, amplitude and polarization only change a little when considering heterogeneity. Since anisotropy is common in real earth structure, we should consider anisotropic media in further research.

Chapter 3

Lateral variation of upper mantle anisotropy beneath the Tibetan Plateau: observations, simulations and Quasi-Love waves

3.1 Abstract

Seismic anisotropy can be studied considering four basic seismic wave properties: direction-dependent travel time anomalies, shear-wave birefringence, surface- wave scattering, and direction-dependent Vp-Vs conversions. In this study, Quasi-Love (QL) waves, generated by surface wave scattering, are utilized to determine the variation of anisotropy of the uppermost mantle of the Tibet plateau. Firstly, QL waves are identified from the seismograms of the selected paths recorded by the CAD station. The observed QL waves are confirmed by distinguishing them from higher mode Rayleigh waves or other body waves, which are absent in synthetic seismograms. Furthermore, the location of azimuthal anisotropy gradient is estimated from the group velocities of Rayleigh wave, Love wave and QL wave. Finally, the characteristics of azimuthal anisotropy of upper mantle in Tibet plateau are summarized. The existence of the azimuthal anisotropy gradient can be explained by an east-west variation of the properties of the tectonic units. Another cause is the force due to the global upper mantle flow (Panza et al., 2010), which has led to the deformation of extensive volumes of rocks.

3.2 Introduction

In a spherical Earth, seismic motion can be separated into spheroidal and toroidal motions. Toroidal modes ${}_nT_l$ sum to form Love waves, which appear primarily on

the transverse component of seismic records. Spheroidal modes ${}_nS_l$ sum to form Rayleigh waves, which appear primarily on the vertical and radial components (Yu et al., 1994). However, the Earth's asphericity can couple the two types of free oscillation into hybrid motion. As a result, 'Quasi-Love' waves may appear on the vertical and radial components and 'quasi-Rayleigh' waves on the transverse component.

Lateral variations in azimuthal anisotropy cause significant waveform anomalies in long-period surface waves, as a result of coupling between fundamental branch Rayleigh and Love waves (Yu et al., 1994). These anomalies, termed "quasi-Love" (QL) waves, have elliptical polarization and arrive slightly behind the Love wave but prior to the Rayleigh wave. Such QL studies (Yu et al., 1994) have illuminated localized regions of mantle strain near several plate boundaries and other geodynamic features. QL waves have been observed along many propagation paths in the Pacific Ocean region (Yu et al., 1994; Kobayashi et al., 1998, 2002), in particular, near Hawaii and seaward of the Tonga-Kermadec, Kurile and Marianas-Izu-Bonin subduction zones, in southern Tibet (Yu et al., 1995) and in the northern Apennines (Levin et al., 2007). Quasi-Love waves are observed in Hawaii, presumably generated by the bow shock gradient in mantle flow (Levin et al., 1998). Surface wave tomography finds a broad concentration of vertical axis anisotropy and strong variations in azimuthal anisotropy near the Hawaii hot spot, which is consistent with a disturbance in shallow mantle flow.

In this study, surface waves that propagate in the central Tibet region are investigated in order to determine the anisotropic properties of the underlying upper mantle and to understand how the anisotropic structure might be caused by tectonic processes. Firstly, examples of QL waves observed in the central Tibet region are presented to illustrate their distinguishing properties. Based on the theoretical modeling of surface wave propagation in a simple Earth model, the anomalous phases are confirmed to be QL waves, but not other body waves (such as SS, SnSn) or higher mode Rayleigh waves. Finally, this chapter discusses what seismological and tectonic

inferences can be made from the observations of the QL wave. Many rocks develop anisotropic elastic properties due to deformation. Mantle anisotropy is sufficient to explain QL wave observations qualitatively as long as the fast axis of symmetry is approximately horizontal. QL wave observations for several propagation paths beneath Tibet are consistent with either flow variations in the mantle or variations in the direction of fossil spreading in older parts of the Eurasia plate (Yu et al., 1995).

3.3 Quasi-Love wave observation

3.3.1 Data pre-processing

To prepare data for this study, seismograms are used which are recorded at station CAD and generated by events at epicentral distances between 10° and 20° (Fig.3.1). The minimum distance was chosen to ensure that the surface wave modes are well separated in time. The maximum distance was chosen to ensure rather uniform propagation paths, mainly in the continental lithosphere of Tibet.

Nine broad-band recordings made at CAD between 2004 and 2007 of shallow earthquakes in western Tibet have been analyzed. Information about the events can be found in Table 3.1.

Table 3.1 Earthquakes used in this study, listed with increasing distance from station CAD

Event	Lat. (°)	Lon. (°)	Depth (km)	Mb	Dist. (°)	BackAz. (°)	Azim. (°)	quasi-Love obs.*
20051031	28.39	84.86	10	4.9	11	99.65	74.04	+
20050407	30.32	83.76	10	5.1	11	88.72	84.23	−
20050408	30.53	83.67	10	5.1	11	88.93	83.99	+
20051214	30.12	78.83	34.2	5.3	15	87.42	83.25	−
20041026	30.88	80.97	12	6	14	85.98	85.58	?
20070722	30.88	78.24	19	5.1	16	85.22	84.87	−
20070506	34.17	82.02	13	5	13	72.32	99.35	−
20060911	35.51	78.2	14	5.5	16	69.29	100.09	−
20050825	36.94	79.17	17	5.5	16	63.79	105.94	+

* + means clear quasi-Love wave (QL) on the seismogram, ? means unidentified QL, - means no QL.

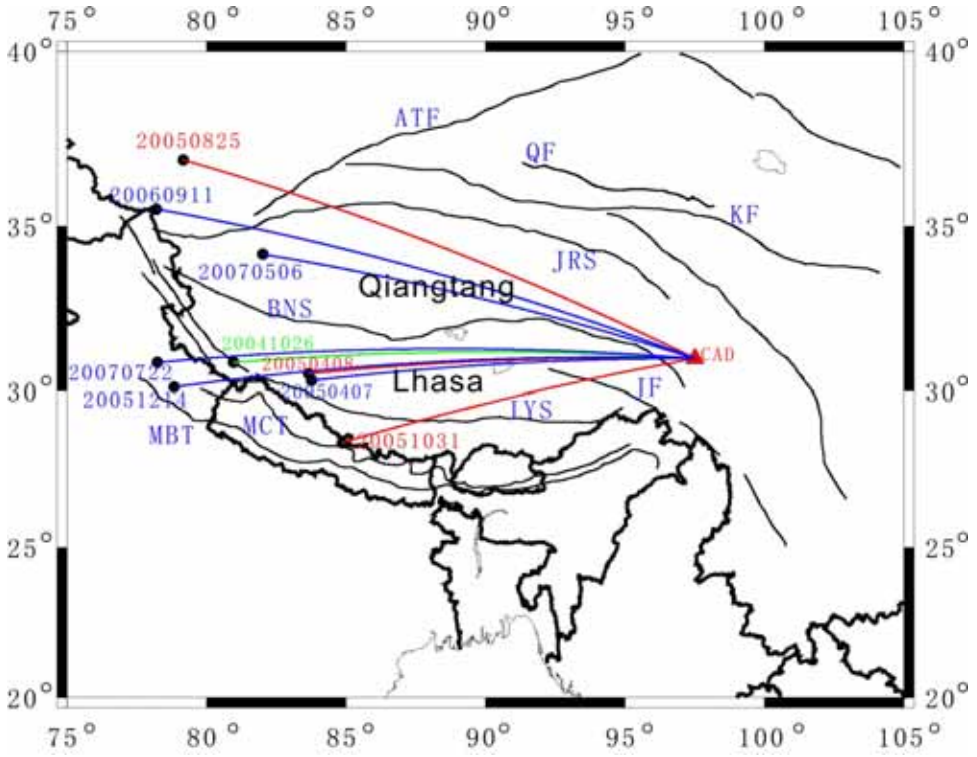

Fig.3.1 An overview map of the distribution of epicenters for all the events used in this work.

Before rotating to radial and transverse components, the instrumental response must be removed. The displacement seismograms are band passed between 0.01Hz and 0.1Hz. Fig.3.2 is the amplitude spectrum of the filtered seismograms for event 20041026.

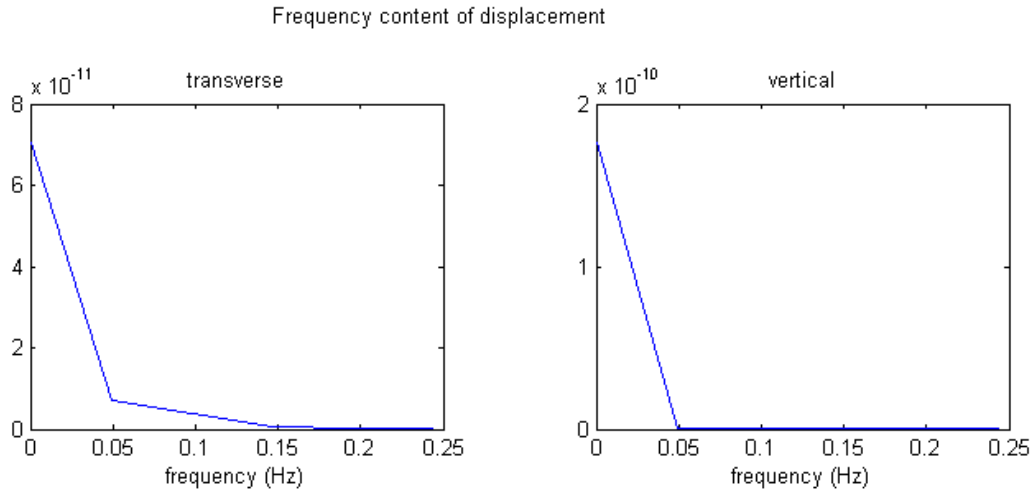

Fig.3.2 Amplitude spectrum for observed displacement of seismic records after applying a band pass filter from 0.01Hz to 0.1Hz

3.3.2 Observed waveforms

Velocity seismograms, acquired by differentiation of displacement seismograms, are very suitable to identifying quasi-Love waves. Fig.3.3 shows the transverse and vertical components recorded at CAD of all events. The paths shown in red correspond to seismograms in which we find the appearance of quasi-Love waves. Likewise, green paths show unidentified and blue paths events lacking quasi-Love waves. By observing the recorded waveforms, the anomalous phases can be easily determined as QL waves on the paths of events 20050825, 20050408 and 20051031. Between the time window of Love wave and Rayleigh wave, no phases or no QL waves occur in the paths of events 20060911, 20070506, 20070722, 20051214 and 20050407. In particular, the anomalous phases of event 20041026 cannot be identified at the first sight. Synthetic seismograms will be used to distinguish the QL wave from other body wave phases or higher mode Rayleigh waves in the next section.

3.3.3 Synthetic velocity seismograms based on mode summation method

The modal summation technique for 1D layered structural models, developed by Panza (1985), Florsch et al. (1991) and Panza et al. (2000), is used to compute synthetic seismograms in this section.

Program **ray** generates the modes for Rayleigh (P-SV waves), and program **lov** generates the modes for Love (SH) waves. The modes are computed for a layered anelastic, laterally homogeneous model. Each layer is defined by its thickness, density, P- and S-wave velocity and attenuation. For computational reasons, thick layers must be split into thinner “numerical” layers characterized by the same elastic and anelastic parameters. Also, low velocity layers, if present in the structural model, require a careful definition in the input file for programs **lov** and **ray**. The thickness of the numerical layers depends on the cut-off frequency chosen for the computation of the normal modes: typically 1 Hz or 10 Hz.

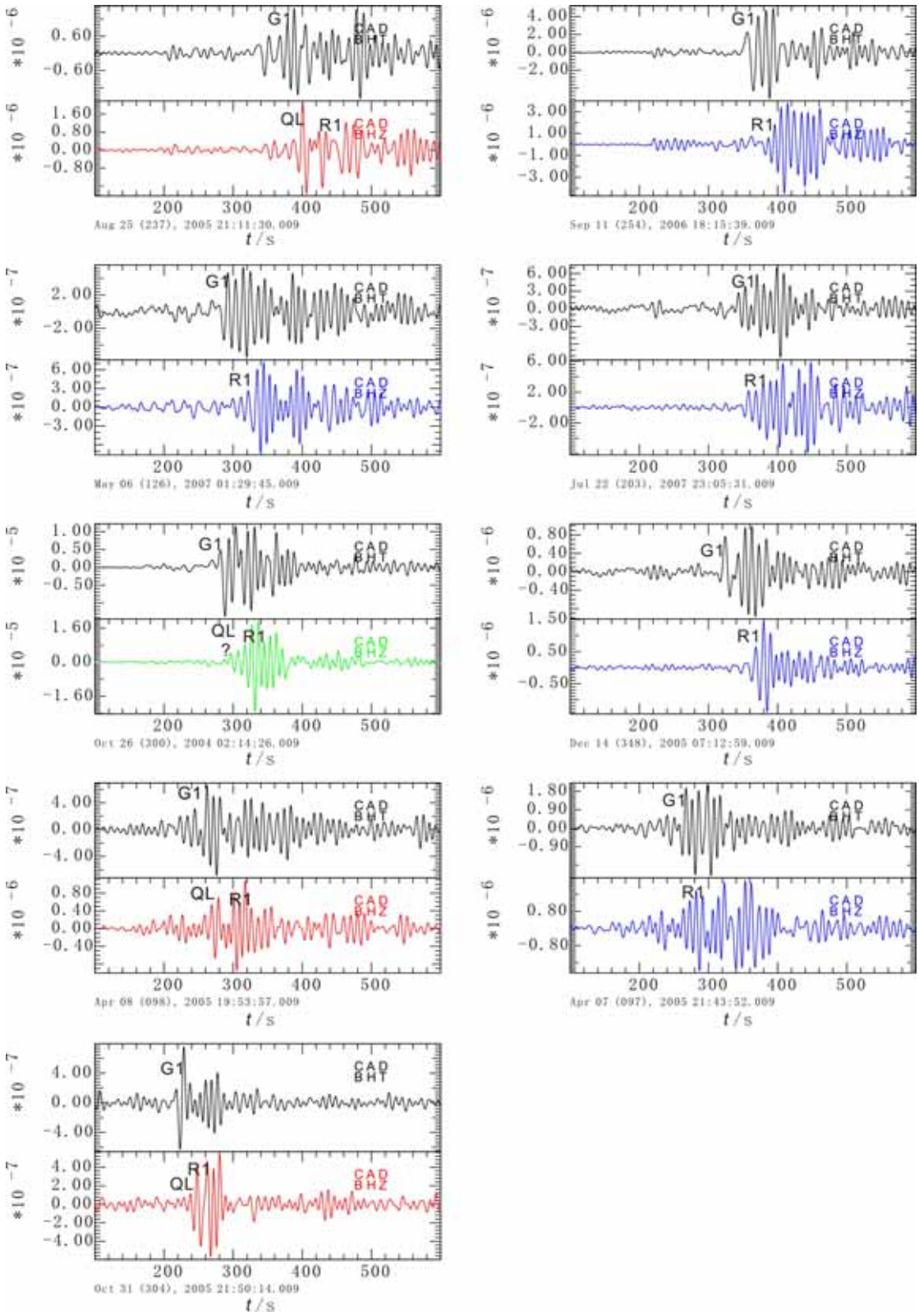

Fig.3.3 Transverse and vertical component records (unit: m/s), at CAD station, for all nine events. Seismograms are corrected for instrument response, rotated and band-pass filtered at 0.01Hz and 0.1Hz. Red seismograms show that QL appears in the time window between Love waves and Rayleigh waves. Green for unidentified QL and Blue for absence of QL.

QL wave (SV-polarized phases), arriving slightly behind the Love wave and before the Rayleigh wave appears to be present in the vertical and radial components, and may be explained either as body waves or as mode-converted surface waves. Detailed synthetic seismogram modeling of representative events reveals several waveforms where the body wave explanation is inadequate, even when unrealistic source parameters are taken into account.

A vertical heterogeneous model (Fig.3.4) from the surface to 90km of depth was formulated from deep seismic sounding data interpretation (Zhang et al., 2002, 2004, 2005) and surface wave dispersion inversion (Rapine, 2003). The depth interval from 90 km to 1200 km was taken from the ak135 model (Kennett et al., 1995). Synthetic seismograms have been calculated by summing all the modes of Rayleigh waves with period T≥20s. The source parameters are taken from the global centroid moment tensor catalog (http://www.globalcmt.org/CMTsearch.html).

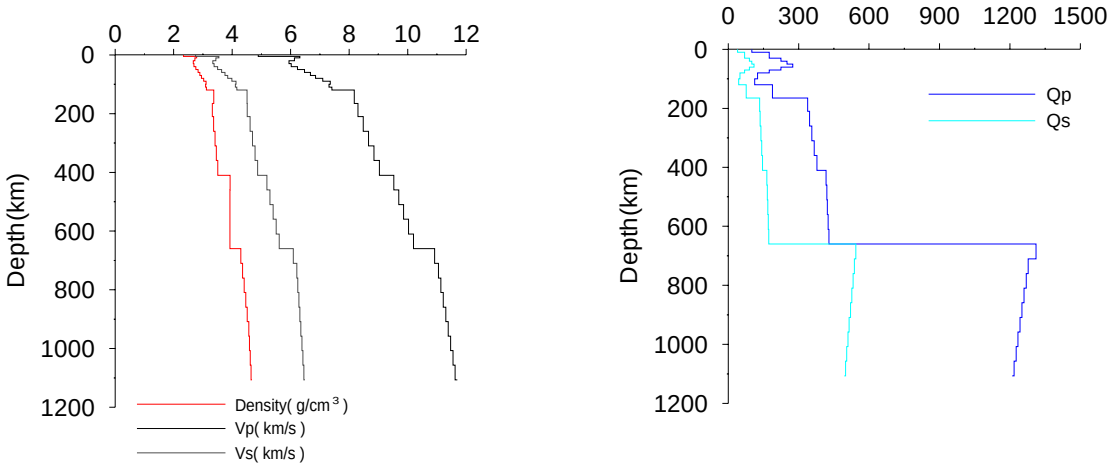

Fig.3.4 Left panel is for velocity and density variation with depth; right panel for anelastic parameters.

Synthetic seismograms (Fig.3.5 and 3.6) are calculated using the synthetic seismograms computer package on the DST Mac-machine. It permits to compute three component synthetic seismograms from the summation of modes of Rayleigh waves and Love waves. Eigenvalues and eigenfunctions of Rayleigh waves for a flat layered anelastic earth-model can be computed efficiently. It is feasible to model any

sort of gradient through fine layering of the elastic and anelastic properties. Given the geometry of observations (two shallow sources with epicentral distance ~15°), the records could contain body waves such as SS, SSS or SnSn.

We find that no phases are modeled in the synthetic vertical component for the events 20051031 and 20041026. Therefore, the observed "anomalous" phases can be identified as QL waves in the path of events 20041026 and 20051031.

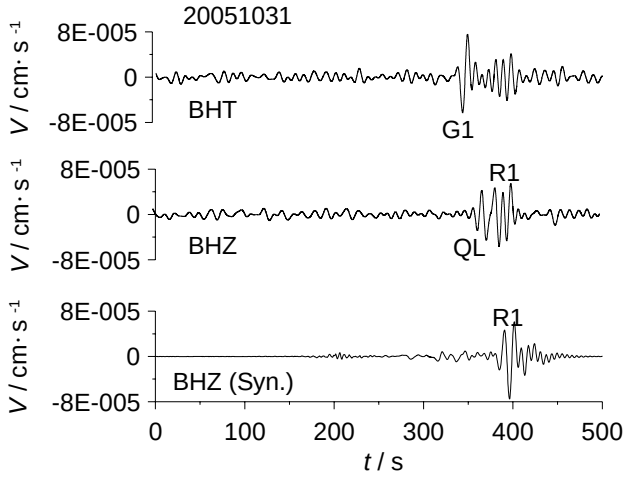

Fig.3.5 Observed transverse and vertical component and synthetic seismograms of the vertical component using modal summation method for the event 20051031.

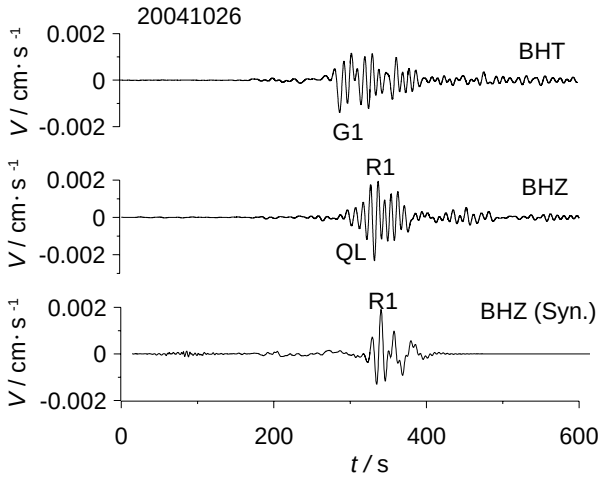

Fig.3.6 Observed transverse and vertical component and synthetic seismograms of the vertical component using modal summation method for the event 20041026.

In the process of synthesizing, if the waveform present in the Love wave window is a body wave, it should also be present in synthetic seismograms computed for a

laterally homogeneous Earth model. Synthetic seismograms in a laterally homogeneous structure including a low velocity zone are computed. Two large events with source mechanism oriented to excite Rayleigh waves of significant amplitude are used in the synthetic computations. These are compared with the observed waveforms of real events.

As for event 20051031, the synthetic seismograms are computed by summing 203 Rayleigh modes and 197 Love modes. Following the theory of seismic strong motion synthetics (Panza, 1987), some parameters have been changed to improve the fit of the synthetic seismograms with observations.

I) Since the difference of the amplitudes between the early and later parts of the recording are large, the depth of the source is adjusted to decrease the difference. It may reflect uncertainties in the location of this event. Observed seismograms and calculated traces with a source depth of 12km are shown in Fig.3.5.

II) Since the synthetic seismogram has not shown a high frequencies phase, source time function and source duration are not changed.

III) Different Q factors are also tested, and finally we choose the Q factors shown in the right panel of Fig.3.4.

IV) From the observation, since the amplitudes of the early arrivals are similar to those of surface waves, there is no need to change the single point source to an extended source, such as a line source or two point source. If necessary, we can use a line source with 10km finiteness factor for this event with epicentral distance larger than 1000km, or a two point source by superposition of two seismograms from a pair of single point sources. Finally, synthetic seismograms with 12km source depth fit well. No higher mode Rayleigh wave, arriving simultaneously with or slightly after the fundamental Love wave, appears in the synthetic seismogram. Therefore, we can conclude that the phase within the Love wave time window in the vertical component is not a body wave or a higher mode Rayleigh wave.

3.3.4 Polarization of Quasi-Love wave

Fig.3.7 illustrates the particle motion of the QL waves. As theoretically proven by Tanimoto (2004) the particle motion of the QL wave is either clockwise or counter-clockwise.

The Love wave vertical polarization is defined by the ratio of the vertical to the transverse displacement (Tanimoto, 2004). This is given by

$$\varepsilon = E_1 \cos 2\theta + E_2 \sin 2\theta + E_3 \cos 4\theta + E_4 \sin 4\theta \tag{3.1}$$

Where

$$E_i = \frac{U(H)}{W(H)} \frac{\int_{-\infty}^{H} M_i dz}{\int_{-\infty}^{H} (R_0 - L_0) dz} \tag{3.2}$$

Since there is no isotropic term E_0 in Eq. (3.1), the particle motion must occur within 360°.

Expressions for the coupling (M_i), Love wave azimuthal terms L_i and Rayleigh wave azimuthal terms R_i are as follows,

$$M_0 = 0$$

$$M_1 = (C_{xxxx} + C_{yyyy})k^2 WV/2 - C_{zzxy} kU'W + C_{xzyz} W'(V' + kU)$$

$$M_2 = (-C_{xxxx} + C_{yyyy})k^2 WV/4 + (C_{xxzz} - C_{yyzz})kU'W/2 + (-C_{xzyz} + C_{yzyz})W'(V' + kU)/2$$

$$M_3 = (C_{xxxy} - C_{yyxy})k^2 WV/2$$

$$M_4 = [-(C_{xxxx} + C_{yyyy})/8 + C_{xxyy}/4 + C_{xyxy}/2]k^2 WV$$

$$L_0 = [(C_{xxxx} + C_{yyyy})/8 - C_{xxyy}/4 + C_{xyxy}/2]k^2 W^2 + (C_{xzsz} + C_{yzyz})W'^2/2$$

$$R_0 = [3(C_{xxxx} + C_{yyyy})/8 + C_{xxyy}/4 + C_{xyxy}/2]k^2 V^2$$

$$-(C_{xxzz} + C_{yyzz})kU'V + C_{zzzz} U'^2 + (C_{xzsz} + C_{yzyz})(V' + kU)^2/2 . \tag{3.3}$$

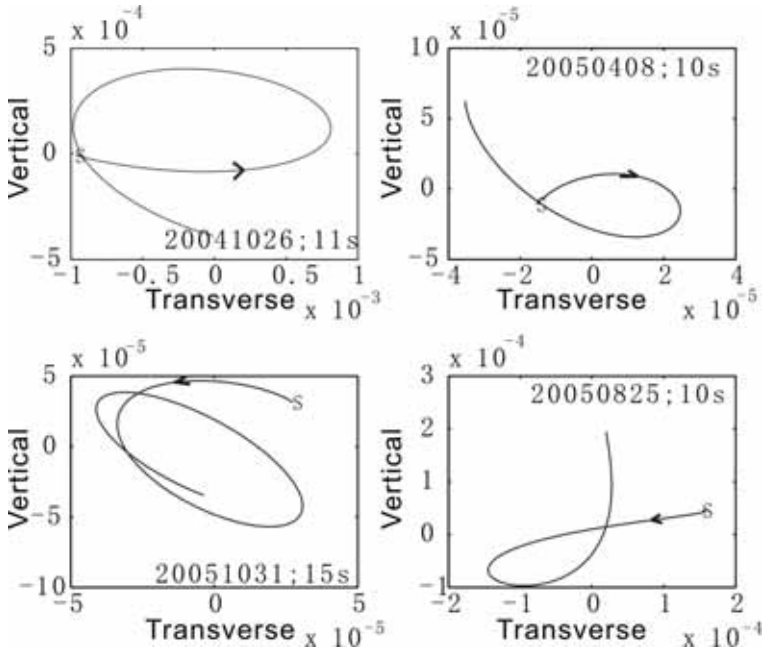

Fig. 3.7 Particle motion for QL waveforms recorded at CAD. For each plot the length of the time interval is given. The starting points are indicated by character S and motion direction is marked by arrow. (unit of x and y axis is m/s)

3.4 Analysis of the focal mechanism

The SV-polarized phase is prominent if the observation is made near the Rayleigh wave radiation node of the source, where it is similar in amplitude to the Rayleigh wave. Usually, large, shallow, predominantly strike-slip events will give better observation of QL waves (Yu et al., 1995; Park et al., 1994).

However, in this study, a strike-slip event (20041026), a thrust event (20051031, 20050825) and a normal event (20050408) have all generated QL waves. So the type of focal mechanism is not a necessary condition for the existence of QL waves.

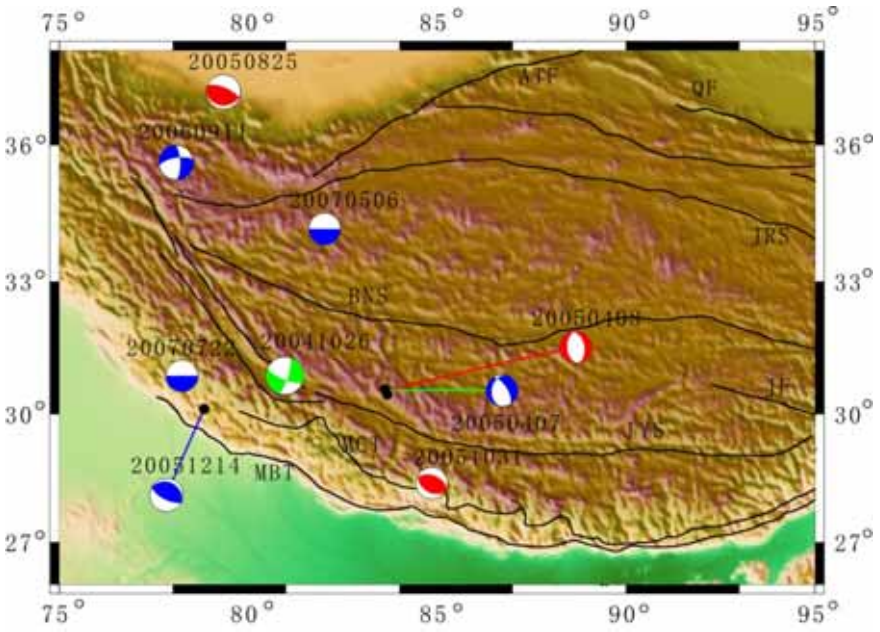

Fig.3.8 Distribution of events. We have colored the focal mechanism with the same color-code as that used in Fig. 3.1, which depends on the appearance of the QL wave.

3.5 Identification of Love-to-Rayleigh conversion areas

The QL wave propagates as a Love wave with the group velocity U_L from the source to the conversion area, and as a Rayleigh wave with the group velocity U_R from the conversion area to the station. If the conversion continuously occurs over a finite interval along the great circle path, the QL wave should show a long wave packet (Kobayashi et al., 1998). In this study, the conversion area for QL wave is assumed to occur at a point. Since the QL wave propagates with the Rayleigh wave group velocity after the Love-to-Rayleigh conversion, the apparent group traveltime of the QL wave for an epicentral distance Δ is expressed as

$$\frac{\Delta}{U_{qL}} = \frac{\Delta - \delta\Delta}{U_L} + \frac{\delta\Delta}{U_R} \quad . \tag{3.4}$$

Note that U_{qL} is nearly equal to U_R for $\Delta = \delta\Delta$ and that U_{qL} is nearly equal to U_L for a small value of $\delta\Delta$.

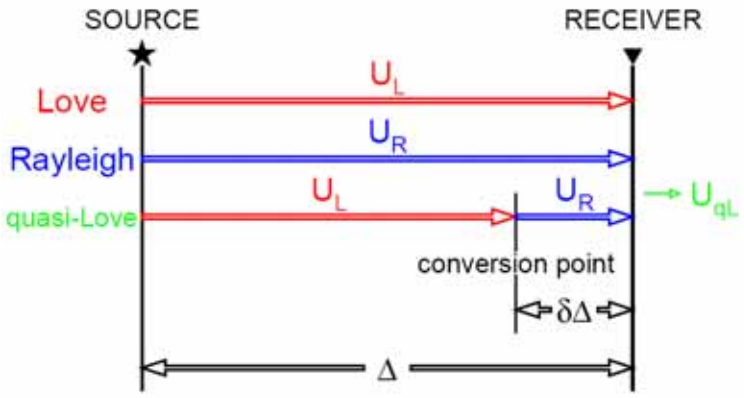

Fig.3.9 Schematic map of the velocity of the QL wave.

In the following formula (3.4), the distance $\delta\Delta$ between the conversion point and the station is given:

$$\delta\Delta = \frac{U_{qL}^{-1} - U_L^{-1}}{U_R^{-1} - U_L^{-1}}\Delta \tag{3.4}$$

$\delta\Delta$ represents the distance between the conversion point and the station. U_L, U_R, U_{qL}, Δ are observed group velocities of Love waves, Rayleigh waves, apparent group velocity of quasi-Love waves and epicentral distance, respectively.

The group velocities are measured by a method based on the multiple filter analysis (Dziewonski et al., 1969) and described by Herrmann and Ammon (2002) using the program **surf**. Following Herrmann and Ammon (2002), data preparation began by rotating and correcting waveforms for the instrument response maintaining the Seismic Analysis Code (SAC) format. All surface wave SAC files must have the time of the first sample, origin time, distance, azimuth and back azimuth. Next step is to run the do_mft program to do the multiple filter analysis (MFT). MFT selects filter parameters for SAC files, identifies modes interactively, chooses phase filtering and stores the processing result in files. MFT is important for the separation of various modes when they arrive simultaneously at the seismic station (multipathing). We can assume a dispersed surface wave mode be represented by

$$s(t) = \frac{1}{2\pi}\int_{-\infty}^{\infty} A(\varpi)e^{i(\varpi t - kr + \phi)}d\varpi \tag{3.5}$$

where t is time, ϖ is the angular frequency, k is the horizontal wave number, r is epicentral distance, and ϕ is phase advance due to source. A filtered signal, resulting from the action of the filter $H(\varpi)$ on $s(t)$ is

$$g(t) = \frac{1}{2\pi}\int_{-\infty}^{\infty} H(\varpi)A(\varpi)e^{i(\varpi t - kr + \phi)}d\varpi \quad , \tag{3.6}$$

where the filter is defined with a center frequency ϖ_0 as

$$H(\varpi) = \exp[-\alpha(\varpi - \varpi_0)^2 / \varpi_0^2] \tag{3.7}$$

Choice of α is not trivial, and Levshin et al. (1992) suggest that the spectral amplitude estimate is good only when α is set larger with increasing distance. In general, it is recommended (Herrmann et al., 2002) to use α = 25 for distances of less 1000 km and α =50 for distances of less than 2000 km. In this study, α is equal to 12.5 and the dispersive curves are shown in Fig.3.10. The bandwidth is chosen so that the QL waves are clearly separated from the Rayleigh waves in time domain in the vertical component. Next step was to select the fundamental mode from the displayed menu using the pick box and visually selecting the dispersion values a single point at a time with the mouse. The selected picks are saved in a file called disp.d to be used as the group velocity values.

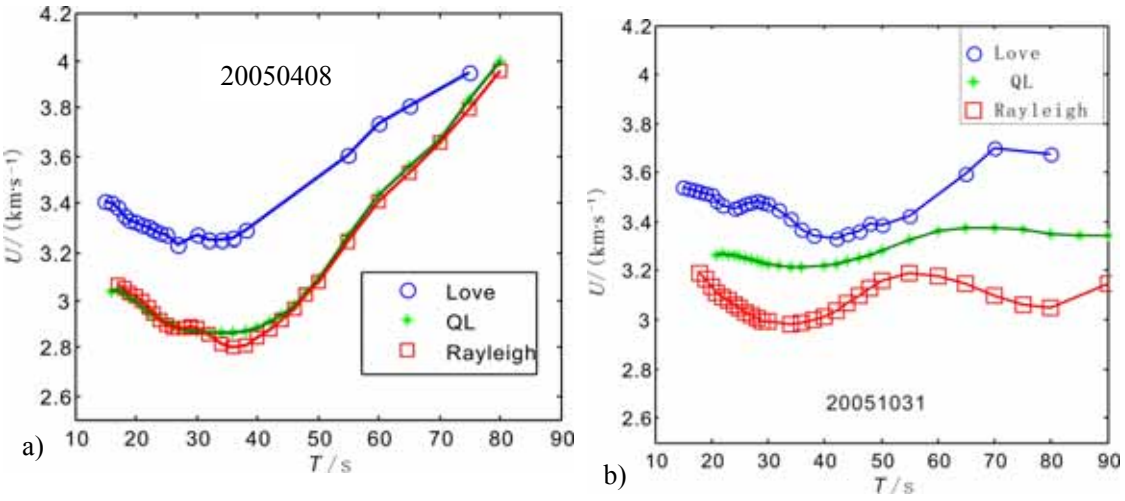

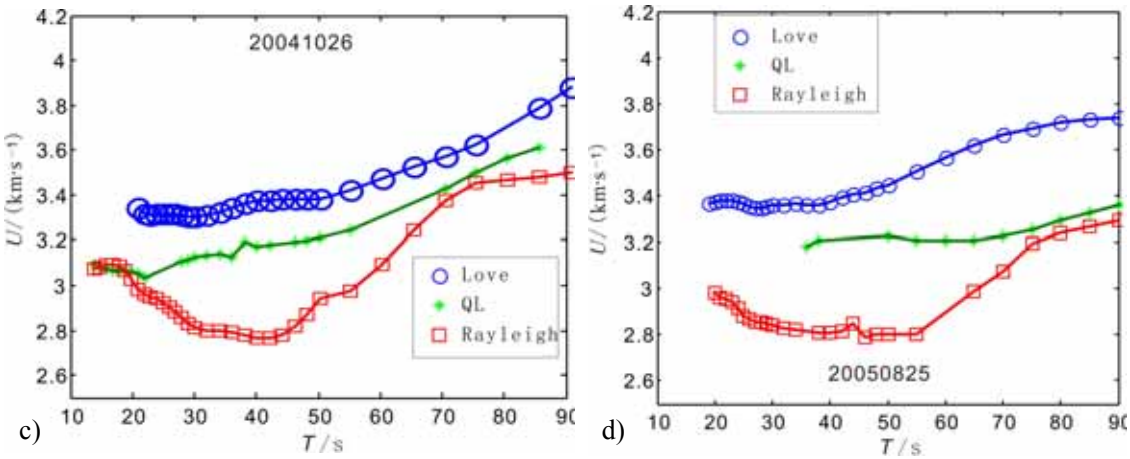

Fig. 3.10 a)-d) Dispersion curve of Love, QL and Rayleigh wave for the event 20050408, 20051031, 20041026 and 20050825, respectively.

In the Lhasa terrane, we find that an anisotropy gradient exists in the western and eastern part, but not in the central part and that it is depth-dependent. Yu and Park (1995) had detected an anisotropy gradient zone in the window 91°E-98°E and 28°N-32°N. The result of our study regarding the anisotropy gradient in the eastern part agrees with their study.

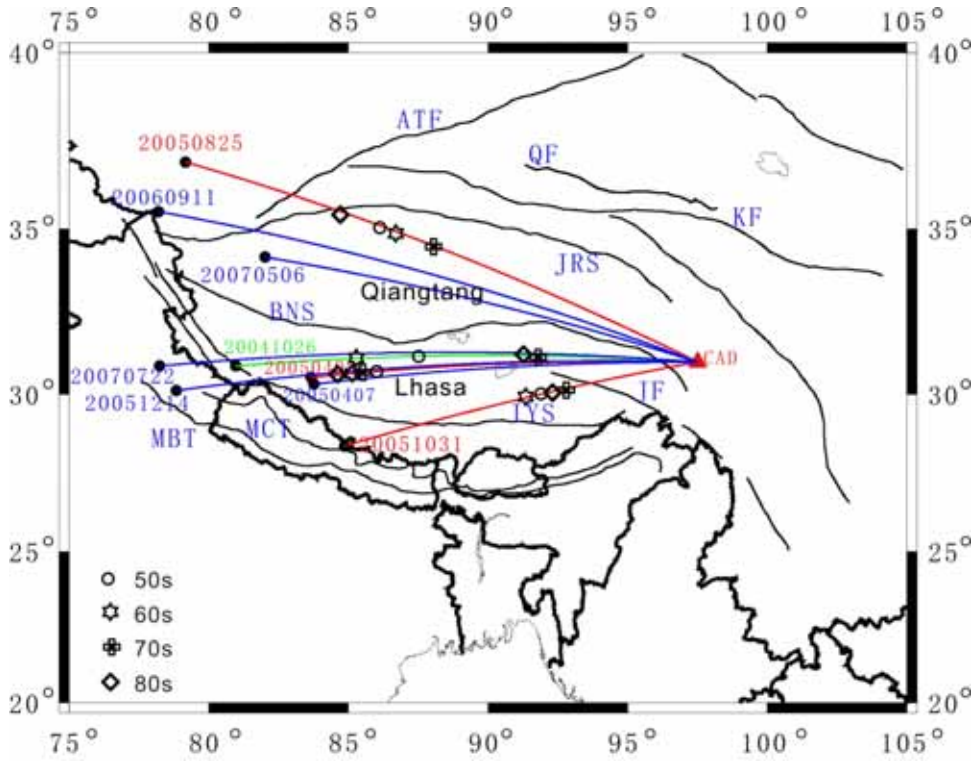

Fig. 3.11 Location of transition points of frequency-dependent azimuthal anisotropy.

3.6 Discussion and Conclusion

Shear wave splitting, inversion of surface wave dispersion and tomography of Pn traveltimes are the main techniques for studying azimuthal anisotropy in Tibet. The results from the study of SKS splitting (McNamara et al, 1994; Liu et al., 2001; Jiang et al., 2001) showed that the polarization direction of anisotropy varies from NNE -to- NE -to- NEE -to- EW starting from the IYS northward and passing through the south and north Tanggula mountain, and ending north of the Kunlun mountain. According to a surface wave study resolving lateral heterogeneity and azimuthal anisotropy of Rayleigh wave group velocities simultaneously in the period range 10-184 s in East Asia (Huang et al., 2004), the anisotropy distribution in the 63s period (Fig. 3.12) shows variation in central Tibet, which is consistent with our QL waves observation, indicating that the anisotropy is caused by convectional flow in the mantle. Pei et al. (2007) obtained velocity images and Pn anisotropy (Fig.3.12) of the uppermost mantle beneath China by performing tomographic inversion of both Pn and Sn traveltimes. Beneath the India-Eurasia collision zone, the Pn anisotropy direction is parallel to the collision arc and nearly perpendicular to both the direction of maximum compression and crustal movement resulting from pure shear deformation.

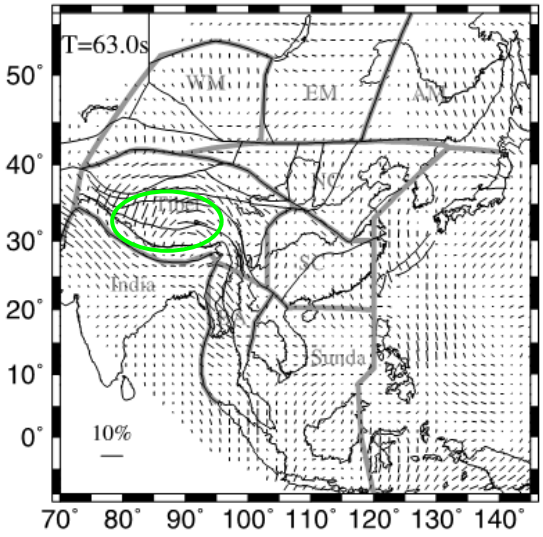

Fig.3.12 Anisotropy distribution at period T=63 s. Thick gray lines demarcate tectonic domains. WM-West Mongolia; EM-East Mongolia; AM - Amuria; NC - North China; SC - South China; BA-Burma and Andaman Sea. Green ellipse marks the studied area in this chapter. (After Huang et al., 2004)

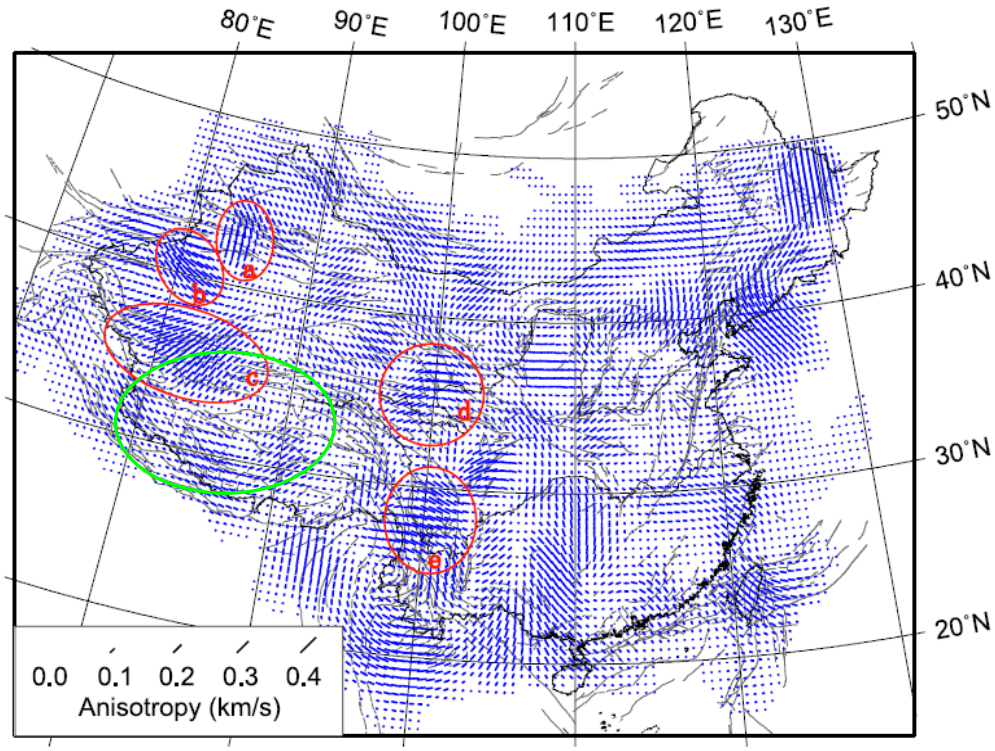

Fig.3.13 Tomographic image of Pn velocity anisotropy. Line segments are drawn parallel to the direction of highest velocity, with their length proportional to the magnitude of anisotropy. Regions exhibiting large anisotropy and possessing dense ray coverage are marked with red circles and labeled as a, b, c, d and e. Green ellipse marks the studied area in this chapter. (After Pei et al., 2007)

The green ellipse, in Fig. 3.12 and 3.13, indicates the studied area in this chapter. The amplitude and direction of anisotropy have obvious variation. The positions of the anisotropy gradient are consistent with our location from the observation of QL waves.

The Love to Rayleigh conversion by surface wave scattering at long period, indicates anisotropy gradient existing in the depth of 100~300 km (Oda et al., 2001; Yu et al., 1994). The seaward sides of several Pacific subduction zones (Tonga-Kermadec, Japan-Kurile, and the central Aleutians) exhibit QL wave observations that are consistent with strong trench-parallel flow and/or extension in the asthenosphere beneath the subducting slab (Yu et al., 1994; Kobayashi et al., 1998). There is a rough correlation between quasi-Love amplitude, backarc spreading, and inferred trench rollback. Large quasi-Love amplitudes are observed near Tonga-Kermadec (Park et al., 1993; Yu et al., 1994), where back-arc spreading and rollback are large, and smaller

amplitudes are observed at Kamchatka, where back-arc activity is ambiguous. Quasi-Love waves are generated in the mantle beneath the Tangula-Shan mountains (Fig. 3.13), a convergence zone at the southern edge of the Tibetan Plateau (Yu et al., 1995). The surface waves suggest a concentration of compressive pure shear in the mantle beneath the southern edge of the plateau, perhaps in response to the collision of the Indian subcontinent from the south (Yu et al., 1995). Hot spots in the mantle may generate predictable flow patterns beneath moving lithosphere, with a bow shock gradient forward of the rising plume and a long sheared tail (Ribe et al., 1994).

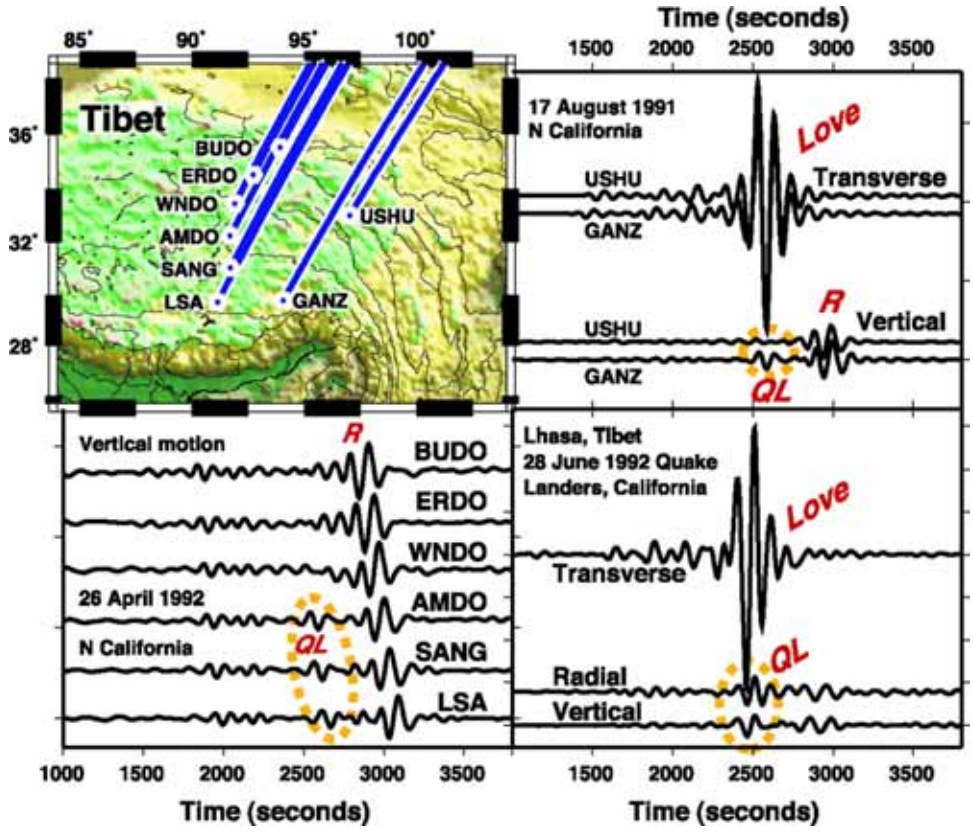

Fig.3.14 Love-to-Rayleigh surface-wave scattering in the Tibetan Plateau. Portable seismological stations are marked, with propagation paths of surface waves from California earthquakes. The QL scattered phase was generated by the Love wave as it passed through the southern plateau, between stations USHU and GANZ to the east and between stations WNDO and AMDO in the central plateau. Seismic signals are low-passed at 100 s and rotated to radial and transverse horizontal coordinates to isolate the Love wave. The QL wave diagnoses a sharp lateral gradient in anisotropic properties in the southern plateau. The waveforms can be modeled with localized 4% Vs anisotropy at 100 to 300 km depth with an east-west horizontal fast symmetry axis. (After Park et al., 2002)

Yu et al. (1995) observed QL waves in Tibet after the large Landers earthquake of southern California in 28 June 1992, a strike-slip event with NEIC epicenter distance ~100° (NEIC). Among all the available stations, QL wave can be observed in the southeast but is absent in northeast and southwest of Tibet. By modeling the long-period surface-wave propagation using anisotropic Earth models, they considered two upper mantle models for the Tibetan Plateau. One model is based on the assumption that anisotropy is purely induced by mantle deformation which is due to a north-south compression associated with the continental collision; the other is based on the results of SKS splitting observations. The modeled waveforms mismatched with the observed waveforms. Possibly, there are at least 3 causes for this discrepancy: significant P-wave anisotropy exists under the plateau, or the S-wave anisotropy does not possess a uniformly horizontal symmetry axis, or strong east-west gradients in anisotropy bias their comparison of observations and synthetic calculations.

Combining our results of Fig. 3.10 with those of Yu et al. (1995), we think that the south-north lateral variation of azimuthal anisotropy is located in the Tanggula mountain, and that the east-west lateral variation is found at longitude 85° to the north of the Gandese mountain and near the Jinsha river fault.

The reasons for the south-north lateral variation of azimuthal anisotropy possibly are: 1) the deformation of upper mantle is brittle in the southern Tibet and ductile in northern Tibet based on a focal mechanism research (Lev et al., 1997); 2）The direction of ductile upper mantle flow rotates clockwise from south to north. The variation of anisotropy perhaps is connected to the strength of the flow, which is weaker in the south than in the north. Another possibility is that the thickness of the anisotropic layer is smaller in the south than in the north; 3) many studies proposed low Pn velocity and the absence of Sn wave in north Tibet. The fact that Cenozoic volcanic rock is pervasive in the crust and magmatism is still active, demonstrate the existence of hot lithospheric mantle and partial melting under the Moho in the northern Tibet, which will increase the amplitude of anisotropy (Yang et al., 2002).

The explanations for the east-west lateral variation of azimuthal anisotropy are: 1)

the variation of deep structure, in the sense that the Moho interface is shallow in the west and deep in the east (Zhang et al., 2002). The Poisson ratio is smaller in the middle part compared to that in the east and west (Zhang et al., 2004). A east-west oriented wide-angle reflection seismic profile in northern Tibet (Zhang et al., 2002) has revealed that the rheology is elastic in the west and somewhat viscous in the eastern part of the profile; 2) the direction of strain changes from NW to EW (Zhang et al., 2004); 3) the velocity of the mantle is higher in northwestern Tibet compared to eastern Tibet (longitude 87° E marking the dividing line) as emerged from teleseismic SS and S waves traveltimes (Dricker et al., 2002); 4) in Tibet, there is not only a majority of east-west oriented mega-geotectonic structures, but also two important south-north megageotectonic lines and many mesoscopic structures (Zhang et al., 2004). The western mega-geotectonic line is oriented south-north and is centered near longitude 84° －85° E and the eastern north-south oriented megageotectonic trend is centered on longitudes 92° -94° E. The two megageotectonic lines divide Tibet into three parts. In the results stemming from tomography of body waves, the east-west separation can be seen in the velocity at 120km depth, and it continues to the depth of 360-410km in the upper mantle; 5) as the consequence of the Indian subcontinental northward underthrust, deformation occurs by upper mantle flow in Tibet. The complex collision between the Indian plate and the Eurasian plate possibly has generated different intensities of east-west deformation, and hence causes lateral variation of azimuthal anisotropy.

Among the nine events we have considered, the paths of event 20041026, 20050825, 20050408 and 20051031 generate QL waves. No QL waves occur in the paths of events 20060911, 20070506, 20070722, 20051214 and 20050407. There are two possible causes for the absence of the QL waves: 1) multiple lateral variations under the path and it will interfere the QL waves so that the QL waves can't be observed; 2）the QL waves could mainly contain higher mode Rayleigh waves converted from the fundamental Love waves, and might decay in the low-Q upper mantle, where the energy of higher mode Rayleigh waves concentrate. From the azimuthal anisotropy image at 63 s period of the surface wave dispersion inversion

(Huang et al., 2004), lateral variation of azimuthal anisotropy is obvious in the Qiangtang terrane. QL waves should be easily generated. But no QL waves in the paths of events 20060911 and 20070506 are found. It might be the interference due to the multiple lateral variations.

Further consideration: Quasi-Love waveforms, however, are sensitive primarily to the gradient, not to the absolute level of anisotropic properties. The details of upper mantle anisotropy, such as its amplitude and orientation, its depth dependence, are not yet considered well. It needs further forward modeling of the waveforms.

Chapter 4

Determination of the composition of the lithosphere: relationship between density, velocity, temperature and pressure

4.1 Introduction

The structure and petrology of the continental crust and uppermost mantle is of great importance in understanding the generation and evolution of the lithosphere. Fortunately, many compressional wave velocities have been acquired from tomography and refraction studies (Mitra et al., 2005, Hauck et al., 1998, Haines et al., 2003, Meissner et al., 2004, Zhao et al., 2001). The results can be used to deduce the relation between compressional wave velocities, shear wave velocities or densities and depth, temperature and pressure.

In using velocities to place constraints on lithosphere petrology, it is important to understand how velocities and densities vary with depth, temperature and pressure. In addition, studies based on the correlations between density, shear wave velocity, and compressional wave velocity are much more powerful than merely glancing uncritically at a single seismic cross-section (Anderson, 2007). On the other hand, the influence of aluminum on elastic properties is not yet known (Yagi et al., 2004), but the effect of calcium is probably small (Shim et al., 2000; Deschamps et al., 2003). With a caveat concerning aluminum, it is thus reasonable to assume that most of the 3D structure seen by seismic data is due to spatial variations in iron, silicon, and temperature. Density variations allow us to distinguish between perovskite and iron effects (Forte et al., 2001), so independent constraints on density prove crucial to infer correct temperature and compositional variations.

4.2 Density as a function of velocity for different rock types

The essence of tectonics is the crustal deformation and the movement of lithospheric material. The tectonic history has been recorded by the rocks, from which it is possible to recover the continental dynamics. The properties of the rocks we may consider are rock type, mineralogical composition, age, temperature and pressure conditions of formation. In this context, the key physical properties are density and seismic velocity and their mutual relation.

According to Brocher's compilation (Brocher, 2005), based on published laboratory measurements of ρ and V_P values the non-linear relationship between density and velocity for different rock types and for the range of V_P between 1.5 and 8.5 km/sec. can be summarized as follows:

$$\rho\,(\mathrm{g/cm^3}) = 1.6612V_P - 0.4721V_P^2 + 0.0671V_P^3 - 0.0043V_P^4 + 0.000106V_P^5 \quad . \quad (4.1)$$

Eq. (4.1) is the polynomial regression fit of the Nafe-Drake curve. It can be used for all rock types except mafic crustal and calcium-rich rocks.

For sedimentary rocks and V_P between 1.5 and 6.1 km/sec, Gardner's rule (1974) should be applied:

$$\rho\,(\mathrm{g/cm^3}) = 1.74V_P^{0.25} . \quad (4.2)$$

The linear relation (4.3) proposed by Christensen and Mooney (1995) is appropriate for all crystalline rocks except volcanic and monomineralic rocks at 10km depth and for V_P between 5.5 and 7.5 km/sec:

$$\rho\,(\mathrm{g/cm^3}) = 0.541 + 0.3601V_P \quad . \quad (4.3)$$

Following Christensen and Mooney (1995), Godfrey et al. (1997) analyzed the rock types in detail and gave the linear relation (4.4) for basalt, diabase and gabbro at 10km depth and for V_P between 5.9 and 7.1km/sec.

$$\rho\,(\mathrm{g/cm^3}) = 2.4372 + 0.0761V_P \quad . \quad (4.4)$$

The above four relations between density and V_P are shown in Fig. 4.1.

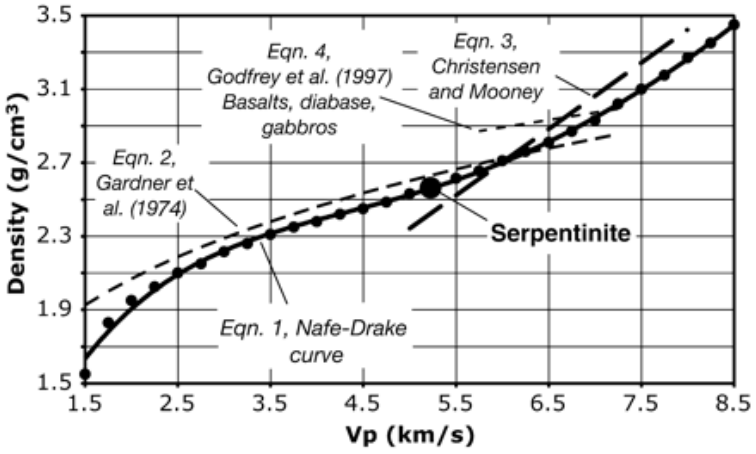

Fig.4.1 Four different relations of density versus V_P depending on rock types and V_P range. Filled circles show values from the curve published by Ludwig *et al.* (1970).The big filled circle shows the global average for serpentinites at 10 km depth. Solid line (equation 1) represents the Nafe–Drake curve. Other labeled lines show relations for sedimentary rocks and crystalline rocks, respectively (after Brocher, 2005).

Table 4.1 ρ and V_P values used to determine the empirical relation (Eq. 4.1) and V_S calculated by Eq. (4.5) (after Brocher, 2005)

V_P (km/sec)	ρ (g/cm^3)	V_S (km/sec)	V_P (km/sec)	ρ (g/cm^3)	V_S (km/sec)
1.5	1.55	0.34	5.25	2.57	3.16
1.75	1.83	0.46	5.5	2.62	3.3
2	1.95	0.61	5.75	2.66	3.43
2.25	2.03	0.79	6	2.71	3.55
2.5	2.1	0.98	6.25	2.76	3.66
2.75	2.15	1.19	6.5	2.81	3.77
3	2.22	1.41	6.75	2.87	3.88
3.25	2.26	1.63	7	2.93	4
3.5	2.31	1.86	7.25	3.02	4.12
3.75	2.35	2.07	7.5	3.1	4.26
4	2.38	2.28	7.75	3.18	4.42
4.25	2.42	2.48	8	3.27	4.61
4.5	2.45	2.67	8.25	3.35	4.84
4.75	2.49	2.85	8.5	3.45	5.1
5	2.53	3.01			

Based on data from wireline borehole logs for a variety of rocks, vertical seismic

profiles (VSP), laboratory or field measurements on hand samples and seismic tomography studies, Brocher found the new empirical relationship (4.5) for V_S as a function of V_P.

$$V_S \text{ (km/sec)}=0.7858-1.2344V_P+0.7949V_P^2-0.1238V_P^3+0.0064V_P^4. \qquad (4.5)$$

The regression fit of Brocher (2005) is valid for V_P between 1.5-8 km/sec. According to data from shallow boreholes, young saturated sediments having a V_P close to 1.5km/sec yield V_S close to 0.1km/sec (Boore, 2003). Quaternary alluvium and older sedimentary rocks have V_P between 1.5-2.5km/sec with a rapid increase in V_S (De et al., 1994; Newhouse et al., 2004). Older or coarser-grained sedimentary rocks have V_P between 2.5-3.5km/sec with further increases in V_S based on VSP data tomography and averages of laboratory measurements on sedimentary rocks and volcanic tuffs (Mavko et al., 1998). Brocher's regression fit (4.5) matches well with the result of Castagna et al. (1985) for V_P between 1.5-4.25km/sec.

Particularly, for calcium-rich rocks (including dolomites and anorthosites), mafic rocks and gabbros the linear relation (4.6) can be defined for $5.25<V_P<7.25$ km/sec.

$$V_S \text{ (km/sec)} = 2.88+0.52(V_P-5.25). \qquad (4.6)$$

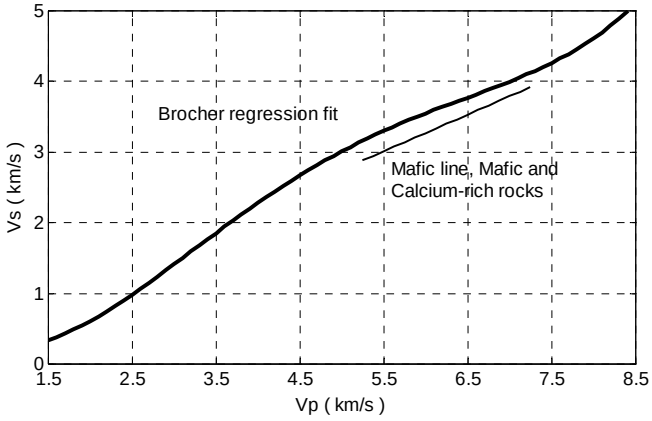

Fig.4.2 V_S as a function of V_P for common lithologies.

4.3 Density and velocity at different depths

Christensen and Mooney (1995) had summarized the structure of the continental crust based on the results of seismic refraction profiles and laboratory data. They inferred crustal composition as a function of depth by comparing seismic results with high-pressure laboratory measurements of seismic velocity for a wide range of rocks that are commonly found in the crust. From the compilation of 560 determinations of the velocity-depth relation they found average velocities for increasing depths, at 5 km depth interval, for different tectonic provinces and for an average continental crust, as seen in Table 4.2.

Density and V_S according to (4.1) and (4.5) are given in Table 4.3 and Table 4.4, respectively.

We can set the density contrast values at the Moho discontiunity in gravity modeling following the rule of Table 4.5.

Table 4.2 Vp and crustal thickness for tectonic provinces and average continental crust (unit : km/s for velocity and km for thickness) (Christensen and Mooney, 1995)

	Orogens	Shields and Platforms	Continental Arcs	Rifts	Extended Crust	Average Crust
Vp(5 km)	5.69±0.67	5.68±0.81	5.80±0.34	5.64±0.64	5.59±0.88	5.95±0.73
Vp(10 km)	6.06±0.39	6.10±0.40	6.17±0.34	6.05±0.18	6.02±0.45	6.21±0.27
Vp(15 km)	6.22±0.32	6.32±0.26	6.38±0.33	6.29±0.19	6.31±0.32	6.31±0.27
Vp(20 km)	6.38±0.34	6.48±0.26	6.55±0.28	6.51±0.23	6.53±0.34	6.47±0.28
Vp(25 km)	6.53±0.39	6.65±0.27	6.69±0.28	6.72±0.35	6.69±0.30	6.64±0.29
Vp(30 km)	6.68±0.43	6.80±0.27	6.84±0.30	6.94±0.37	6.89±0.40	6.78±0.30
Vp(35 km)	6.81±0.40	6.96±0.30	6.99±0.29	7.12±0.33	6.93±0.46	6.93±0.32
Vp(40 km)	6.92±0.44	7.11±0.33	7.14±0.25	7.12±0.30		7.02±0.32
Vp(45 km)	6.96±0.43	7.22±0.39				7.09±0.35
Vp(50 km)	6.99±0.52					7.14±0.38
Crustal thickness	46.3±9.5	41.5±5.8	38.7±9.6	36.2±7.9	30.5±5.3	41.0±6.2

Table 4.3 Density for tectonic provinces and average continental crust (unit : g/cm^3), deduced after the model of Christensen and Mooney (1995), see text for details.

	Orogens	Shields and Platforms	Continental Arcs	Rifts	Extended Crust	Average Crust
Rho(5 km)	2.65±0.92	2.65±1.07	2.68±0.51	2.64±0.89	2.63±1.14	2.71±0.99
Rho(10 km)	2.73±0.58	2.74±0.59	2.75±0.51	2.73±0.28	2.72±0.66	2.76±0.42
Rho(15 km)	2.77±0.49	2.79±0.40	2.80±0.50	2.78±0.30	2.79±0.49	2.79±0.42
Rho(20 km)	2.80±0.51	2.83±0.40	2.85±0.43	2.84±0.36	2.84±0.51	2.83±0.43
Rho(25 km)	2.84±0.58	2.87±0.42	2.88±0.43	2.89±0.53	2.88±0.46	2.87±0.44
Rho(30 km)	2.88±0.63	2.91±0.42	2.92±0.46	2.95±0.55	2.94±0.59	2.91±0.46
Rho(35 km)	2.91±0.59	2.96±0.46	2.97±0.44	3.00±0.50	2.95±0.67	2.95±0.49
Rho(40 km)	2.95±0.65	3.00±0.50	3.01±0.39	3.00±0.46		2.97±0.49
Rho(45 km)	2.96±0.63	3.03±0.58				2.99±0.53
Rho(50 km)	2.97±0.75					3.01±0.57

Table 4.4 Vs for tectonic provinces and average continental crust (unit : km/s), deduced after the model of Christensen and Mooney (1995), see text for details.

	Orogens	Shields and Platforms	Continental Arcs	Rifts	Extended Crust	Average Crust
Vs(5 km)	3.40±0.28	3.39±0.24	3.45±0.45	3.37±0.29	3.35±0.23	3.53±0.26
Vs(10 km)	3.58±0.42	3.60±0.41	3.63±0.45	3.57±0.59	3.56±0.38	3.64±0.51
Vs(15 km)	3.65±0.47	3.69±0.52	3.72±0.46	3.68±0.58	3.69±0.47	3.69±0.51
Vs(20 km)	3.72±0.45	3.76±0.52	3.79±0.50	3.78±0.54	3.79±0.45	3.76±0.50
Vs(25 km)	3.79±0.42	3.84±0.51	3.86±0.50	3.87±0.45	3.86±0.48	3.83±0.49
Vs(30 km)	3.85±0.39	3.91±0.51	3.92±0.48	3.97±0.43	3.95±0.41	3.90±0.48
Vs(35 km)	3.91±0.41	3.98±0.48	3.99±0.49	4.06±0.46	3.97±0.37	3.97±0.47
Vs(40 km)	3.96±0.39	4.05±0.46	4.07±0.52	4.06±0.48		4.01±0.47
Vs(45 km)	3.98±0.39	4.11±0.42				4.04±0.45
Vs(50 km)	3.99±0.34					4.07±0.42

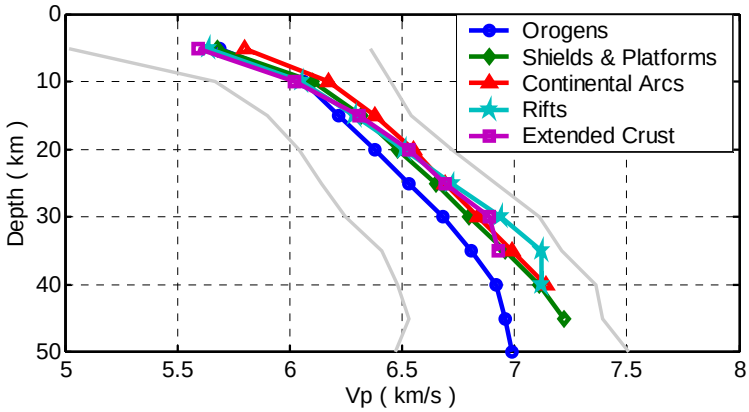

Fig.4.3 Depth versus average compressional wave velocities for five tectonic provinces. Calculations were made at 5km depth intervals. Grey line shows the bounds for Vp values of orogens area (Christensen and Mooney, 1995).

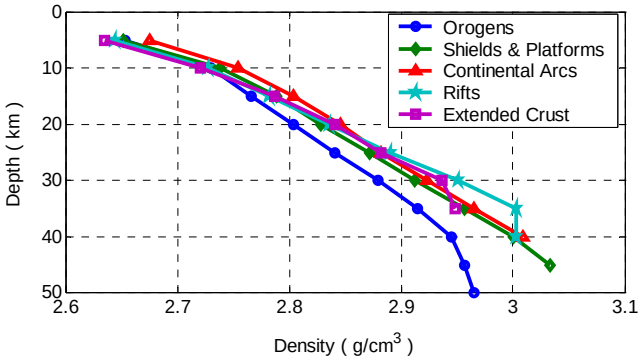

Fig.4.4 Depth versus average densities versus depth for five tectonic provinces. Calculations were made at 5km depth intervals (Christensen and Mooney, 1995).

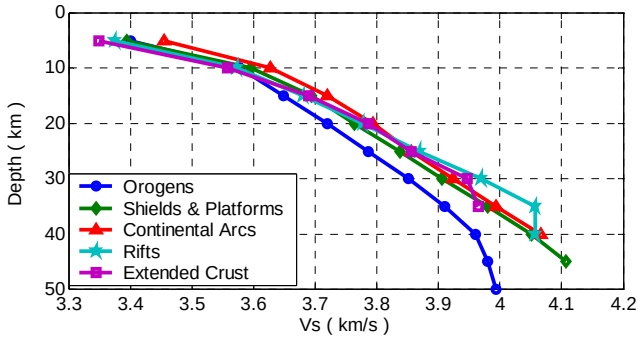

Fig.4.5 Depth versus average shear wave velocities versus depth for five tectonic provinces. Calculations were made at 5km depth intervals (Christensen and Mooney, 1995).

Table 4.5 Density contrast at Moho as a function of depth for orogens (Braitenberg et al., 2000)

Depth(km)	Density contrast(g/cm^3)
25	0.35
30	0.35
35	0.4
40	0.45
45	0.5

4.4 Density as a function of velocity and in situ temperature

The dependency of rock velocity on temperature, pressure and composition can be calculated using mineral physics data and the equation of state (EOS). Many methods for solving the EOS have been proposed and used for Earth studies (e.g. Trampert et al., 2004).

The relationship of average velocities and densities, taking into account the

geotherms and the pressure conditions, allows us to develop a model for the composition of the continental crust and uppermost mantle. Only velocities and densities of orogens for different temperatures are listed here (Table 4.6). Shear wave velocity and density are calculated from compressional wave velocity following Eq. (4.1) and (4.5). Temperatures are converted from depths following Christensen and Mooney (1995), specially for the case of high heat flow.

Table 4.6 Velocities and densities as functions of temperature
(After Christensen and Mooney, 1995)

Temperature(°C) for Orogens	V_P (km/sec)	V_S (km/sec)	ρ (g/cm^3)
138	5.69±0.67	3.40±0.28	2.65±0.92
263	6.06±0.39	3.58±0.42	2.73±0.58
381	6.22±0.32	3.65±0.47	2.77±0.49
501	6.38±0.34	3.72±0.45	2.80±0.51
645	6.53±0.39	3.79±0.42	2.84±0.58
786	6.68±0.43	3.85±0.39	2.88±0.63
925	6.81±0.40	3.91±0.41	2.91±0.59
1065	6.92±0.44	3.96±0.39	2.95±0.65
1204	6.96±0.43	3.98±0.39	2.96±0.63
1344	6.99±0.52	3.99±0.34	2.97±0.75

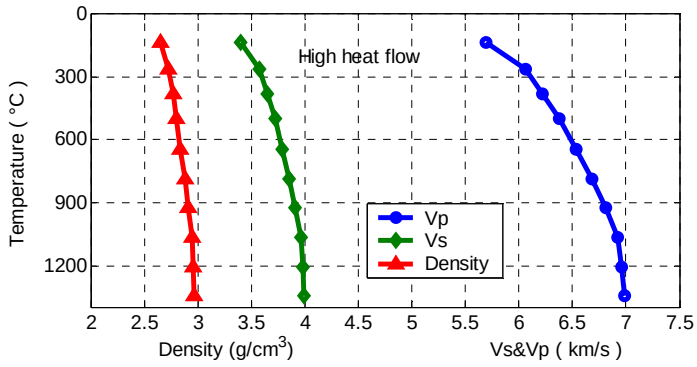

Fig.4.6 Average velocities and densities versus temperature for orogens.

4.5 Physical properties of rocks for different pressure conditions

The values of compressional and shear wave velocity of rocks at confining pressures above 200MPa are primarily controlled by mineralogy (Zhang et al., 1999; Oganov et al., 2001). The results can help us to interpret lithosphere seismological

data better (Kosarev, 1999).

Stacey (1998) has re-examined the thermal and elastic properties of a mineral composite. He gave special emphasis to the gradients of incompressibility with respect to pressure and temperature. Moreover he showed that the thermodynamic estimates of these properties can be applied to the lower mantle. His conclusion is inconsistent with a simple thermal interpretation of tomographic observations of lower mantle velocity anomalies. Seismic experiments that give superior resolution in particular areas, i.e., high-frequency, high-resolution studies, reveal a much more complex mantle than tomography does, and produces a mantle that is not well explained by simplistic, conventional models (Anderson, 2007). The more sophisticated models must include compositional variations, as it is done when considering the composition of lithologies in the crust and mantle. Densities and velocities of eight lithologies as function of pressure (Christensen, and Mooney, 1995) are listed in Table 4.7. Upper crust is considered to be made of serpentinite and granite-gneiss (specifically for Tibet, it has been argued that the main upper-crustal layer is rich in quartz, the compressional velocity of which is between serpentinite and granite-gneiss), middle crust is granite-granodiorite and diorite, lower crust is basalt and gabbro-norite-troctolite, upper mantle is dunite and mafic-eclogite. It should be noted that eclogite has the highest density but not highest velocity. Actually, the velocity of eclogite is lower than the velocity of dunite.

Table 4.7 Densities for different rock types and velocities as function of pressure

(After Christensen and Mooney, 1995)

Rock	ρ (g/cm^3)	200MPa		400MPa		600MPa		800MPa		1000MPa	
		V_P (km/sec)	V_S (km/sec)	V_P	V_S	V_P	V_S	V_P	V_S	V_P	V_S
SER	2.566	5.308	2.588	5.421	2.61	5.497	2.625	5.557	2.636	5.607	2.646
GGN	2.643	6.01	3.501	6.145	3.553	6.208	3.583	6.245	3.607	6.271	3.627
QTZ	2.652	5.963	4.035	6.012	4.048	6.045	4.052	6.070	4.053	6.091	4.054
GRA	2.652	6.246	3.669	6.296	3.692	6.327	3.706	6.352	3.717	6.372	3.726
DIO	2.810	6.497	3.693	6.566	3.717	6.611	3.733	6.646	3.745	6.675	3.756

BAS	2.882	5.914	3.217	5.992	3.246	6.044	3.264	6.084	3.279	6.118	3.291
GAB	2.968	7.138	3.862	7.2	3.888	7.241	3.905	7.273	3.918	7.299	3.929
DUN	3.310	8.299	4.731	8.352	4.759	8.376	4.771	8.39	4.778	8.399	4.783
ECL	3.485	8.001	4.481	8.078	4.524	8.127	4.553	8.166	4.575	8.198	4.594

Serpentinite (SER), Granite-gneiss (GGN), Quartzite (QTZ), Granite-granodiorite (GRA), Diorite (DIO), Basalt (BAS), Gabbro-norite-troctolite (GAB), Dunite (DUN), Mafic-eclogite (ECL).

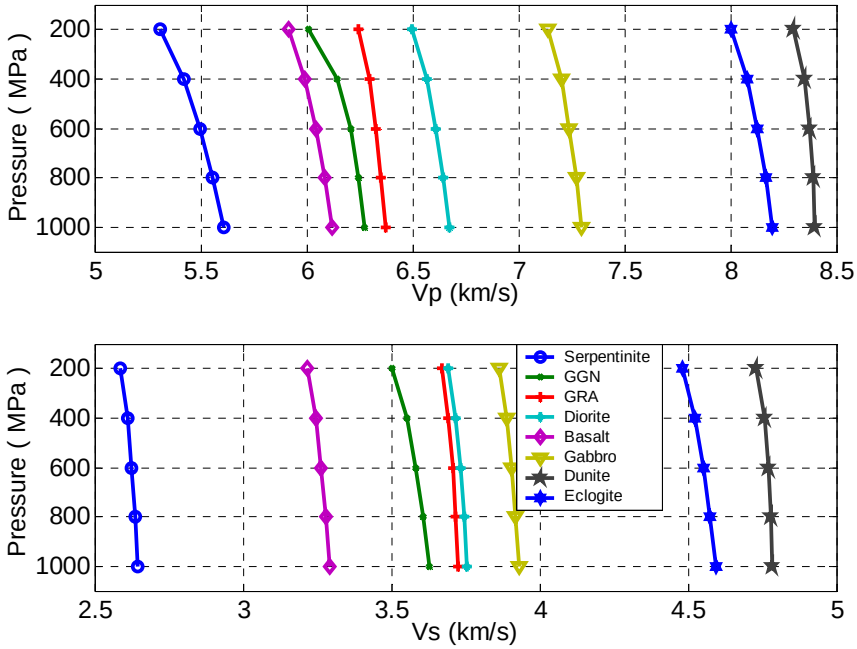

Fig.4.7 Velocities in function of pressure for eight selected rock types

Chapter 5

Crustal density structure beneath the central-south Tibet inferred from gravity modelling

5.1 Abstract

The crustal structure of the Tibet plateau, in the area of latitude 26° – 34° N and longitude 82° – 92° E is investigated by three-dimensional (3-D) gravity modeling constrained by deep seismic surveys. The calculated gravity field (Bouguer anomaly) of the initial density model (model I), which depends on the velocity structure linearly, misfits the observed data. By iterative changes in density and geometry of the interfaces (less than 2 km), the produced second density model (model II) matches better with the observed Bouguer anomaly data. Furthermore, since higher densities than global average densities are found in model II, lower-crustal partial eclogitization is considered in the final model (model III). Model III is designed to determine the absence or presence of partial eclogite in the lower crust beneath the Lhasa terrane. The presence of eclogite has been used in support of the theory of mass transfer from the lower crust to the underlying mantle by previous studies (Bousquet et al., 1997; Henry et al., 1997; Cattin et al., 2001; Tiwari et al., 2006; Hetenyi, 2007 (Fig.5.18)). The presence of eclogite might also influence the topography of mountain ranges and plateaus in Tibet (Bousquet et al., 1997; Henry et al., 1997; Cattin et al., 2001). Seven north-south trending density profiles are investigated by a 3-D gravity forward modeling method with geometry controlled by seismic data. The model implies large variations of the crustal structure from the western to the eastern part of central-south Tibet. The final model shows that dip angles of the Moho interface are near to 8.5° in the eastern and western part of the study area, which is smaller than the one found

in the central part (~16.7°). We may infer that the Indian lithosphere underthrusts the Tibetan lithosphere gently in the eastern and western part of the central-south Tibet, while it is steeper in the central part, which indicates increased flexural rigidity of the lithosphere in the eastern and western part of the study area. Our final model indicates the absence of eclogite in the lower crust of central-south Tibet. This study also provides a realistic crustal density structure as the basis for analyzing the petrologic properties in the crust of central-south Tibet.

5.2 Introduction

With the advent of the theories of continental drift and plate tectonics, it has become widely accepted that the Tibet plateau is the product of the collision between the Indian subcontinent and the Eurasian continent and that this process of mountain building is still continuing today (Holmes, 1965; Dewey and Bird, 1970; Powell and Conaghan, 1973; Le Fort, 1975; Molnar et al., 1977). The Indian subcontinent is moving towards the Eurasian continent at a rate of 50 mm/yr (Minster and Jordan, 1978) with respect to Eurasia plate. Owing to this ongoing tectonic evolution, the Tibet plateau has attracted the interest of geoscientists over many decades.

The structure beneath the Tibetan Plateau started to be delineated with the results of the Sino–American PASSCAL broadband experiment (Owens and Zandt, 1997; McNamara et al., 1997), the international and multidisciplinary INDEPTH experiments (Nelson et al., 1996; Zhao et al., 2001), and the series of Sino–French seismic studies (Hirn et al., 1995; Galvé et al., 2002; Jiang et al., 2006). A large number of geophysical methods have been used to study the lithosphere of the Himalaya and Tibet regions, such as deep seismic investigations (Hauck et al., 1998; Galvé et al., 2002; Haines et al., 2003; Meissner et al., 2004; Zhang et al., 2005; Jiang et al., 2006), seismic tomography (McNamara et al., 1997; Villasenor et al., 2001), magnetotellurics (Wei et al., 2001; Unsworth et al., 2004), gravimetry (Jin et al., 1996; Braitenberg et al., 2000, 2003; Shin et al., 2007), receiver functions (Kind et al., 1995) seismology (Mitra et al., 2005) and geothermics (Chung et al., 2005). These

geophysical studies have played an important role in helping us to understand the crustal structure.

With the use of potential field methods in Tibet and using terrestrial data, Braitenberg et al. (2000) proposed a map of 3-D oscillations of the Moho and discussed the properties along four profiles cutting the Tibet plateau longitudinally and transversally. They applied an inversion-method of the gravity field throughout the entire plateau and later showed (Braitenberg et al., 2003) that there are considerable flexural rigidity variations when going from the Tibet plateau to the cratonic Tarim basin. Shin et al. (2007) presented a 3-D model of the Moho undulations over the entire Tibetan plateau derived from gravity inversion using the Gravity Recovery and Climate Experiment (GRACE) potential field, which has been integrated with terrestrial data. This Moho model is characterized by a sequence of troughs and ridges with a semi-regular pattern, which could reflect the continent–continent collision between the Indian and Eurasian plates.

Generally speaking, the higher the resolution of the seismic information is, the more details on the crustal density structure can be recovered. In this study, the application of a 3-D gravity modeling based on the interpretation of seismic and seismological data, will address the problem whether the crustal structure of the eastern part of central-south Tibet is different from the western part. The study also investigates the deep structure of the collision belt in southern Tibet. The final product of this study is the 3-D density structure beneath central-south Tibet. Since the topography and supporting crustal root are the major contributions to gravity anomalies, the lithosphere-asthenosphere boundary generally contributes with only a small signal in the orogenic tectonic province. The main objective is to model the crustal structure and discuss geodynamic evolution of the Tibet plateau.

5.3 Previous work on the density structure of Tibet

Lyon-Caen et al. (1983) studied the Indian-Eurasia plate collision zone and

examined the effects of each of the following parameters on the configuration of the elastic plate and on the gravity anomalies: the flexural rigidity, the position of the northern end of the elastic plate (the amount of underthrusting of such a plate beneath the Himalaya range), and the density contrasts between the crust and the mantle and between the sediments and the crust. A plate with a constant flexural rigidity of about 0.7×10^{25} Nm allows a good fit to the data from the Lesser Himalaya and the Ganga Basin. However, such a plate cannot underthrust the entire Himalaya. Instead, the gravity anomalies show that the Moho steepens from an inclination of about only 3° beneath the Lesser Himalaya to about 15° beneath the Greater Himalaya. This implies a smaller flexural rigidity beneath the Greater Himalaya than beneath the Ganga Basin and the Lesser Himalaya. They predict rapid uplift only in the Greater Himalaya and at the foot of the Lesser Himalaya.

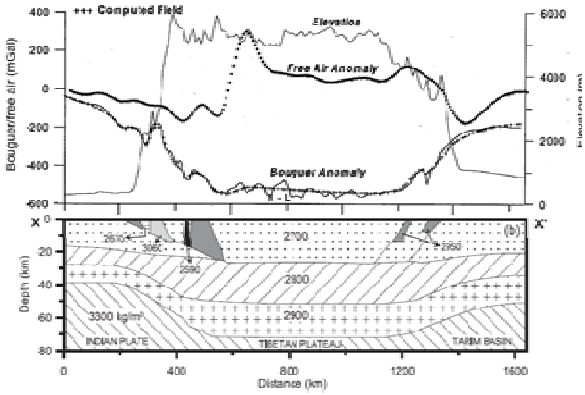

Fig.5.1 Free air gravity anomaly and elevation along longitude 90° E over the Himalaya and Tibet. A positive correlation between the free air anomaly and elevation, and their negative correlation with the Bouguer anomaly suggest isostatic compensation. The crustal model and the corresponding computed gravity field are shown for comparison with the Bouguer anomaly. Densities of various layers are given in the model. Body numbers 1, 5, 6 and 7 represent shallow sources of density 2.950 g/cm^3 and bodies 2, 3 and 4 are of density 2.670, 3.060 and 2.590 g/cm^3 respectively. (After Rajesh, 2003)

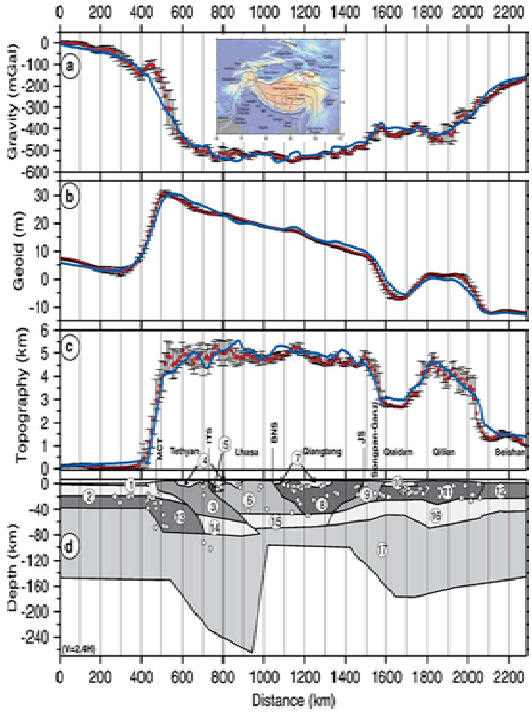

Fig.5.4 Modelling results from elevation, gravity and geoid anomalies. The top three graphs (a-c) show data and results predicted from the model. d) Lithospheric model with a vertical exaggeration of 2.4. (After Jiménez -Munt et al., 2008)

Many 2-D gravity models have been proposed recently. Rajesh (2003) models the Bouguer anomaly along longitude 90° E for latitude 25° –40° N across Himalaya and Tibet and uses the results of INDEPTH seismic profiles across Tibet. In this work it is suggested that the crustal thickness varies from 40 km under the Indo-Gangetic Plains to 70 km under the Indus Tsangpo Suture Zone (ITSZ), remains almost constant at 70 km under the Tibet and reduces to 40 km north of Altyn Tagh Fault (ATF) (Fig.5.1). The crustal vertical section is divided into three layers of bulk densities (2.7, 2.8 and 2.9 g/cm^3), with two low-density layers (2.65 and 2.69 g/cm^3) at the base of the upper and middle crusts respectively, which are layers with low seismic velocities.

Hetényi et al. (2007) combined seismological and Bouguer anomaly data with 2-D thermo-kinematic and petrological modelling to constrain the extent and kinetics of the eclogitization process in the Indian lower crust underthrusting Tibet. Based on Airy-type isostasy gravity modelling, they showed that the presence of denser material (eclogite) is required beneath the Lhasa terrane. Three profiles (Fig.5.2) perpendicular to the Himalayan arc with multilayer density-models suggest that the process of eclogitization of the Indian lower crust is completed where the maximal depth of its descent is reached. The petrologic modeling results of Hetenyi et al. (2007) (Fig.5.3a)–c)) showed many similarities but also some differences in the three profiles. The similarities lie in the fact that, at the very first order, the geometry of the Moho is quite similar along each profile: it starts at 35 km of depth in the South and ends at about 75 km of depth beneath the Tibetan plateau. The major density-change of the Indian lower crust occurs once it reaches its maximum depth. The differences between the three profiles are also linked to the geometries: the steepness and the localization of the lower crust's descent are particular to each profile. Between profile P1 and P2, the differences are small: profile P2 shows a somewhat steeper dip, located closer to the front of the range compared to profile P1, but both profiles reach their maximum depth in one ramp. This is not the case for profile P3: there is a flat part in the descent of the lower crust between two ramps, and constraints on the geometry (even if they are less tight) suggest that it plunges at a lower angle and on a longer distance than

profiles P1 and P2. Thus the gradual change of density also takes place on a larger distance. One additional difference is the geometry of the foreland basin: while data are well explained by a flexural form at profiles P1 and P2, it is better represented with a shallower, flat-bottom basin at profile P3, as previously mentioned by Tiwari et al. (2006).

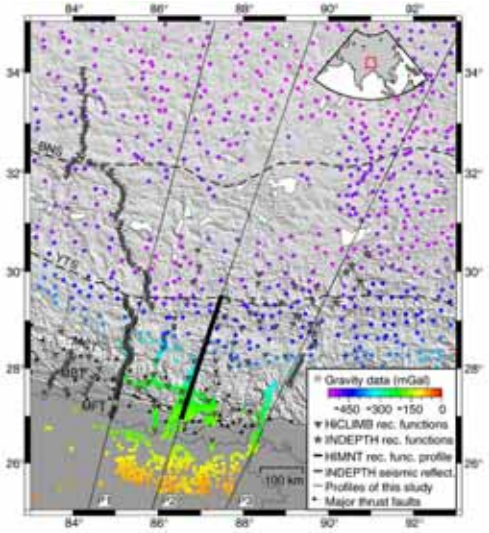

Fig.5.2 Topographic map showing the location of the seismological and gravity data, and the profiles used in Hetenyi's study(2007). The crosses indicate the origin of profiles with the following co-ordinates and orientations: P1 (27.2829°N, 84.9885°E, N14°E); P2 (26.873°N, 86.517°E, N17.8°E); and P3 (26.8°N, 88.5°E, N25°E).

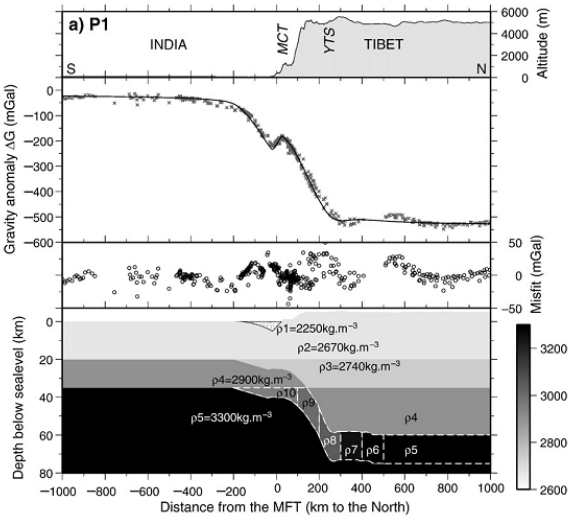

Fig.5.3 a)-c) Three models corresponding to the best fit solutions at profiles P1, P2 and P3 (shown in Fig.5.2). Density values that are not given in the figures are the following: (a) ρ_6 =3300, ρ_7 =3250, ρ_8 =3050, ρ_9 =3000, and ρ_{10} =2950 kg m^{-3} . (b) ρ_6 =3300, ρ_7 =3100, and ρ_8 =3050 kg m^{-3} . (c) ρ_6 =3200, ρ_7 =3100, andρ_8 =3000 kg m^{-3} . (After Hetenyi, 2007)

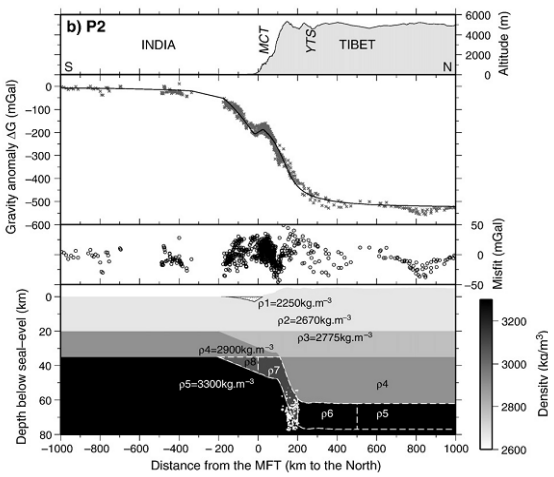

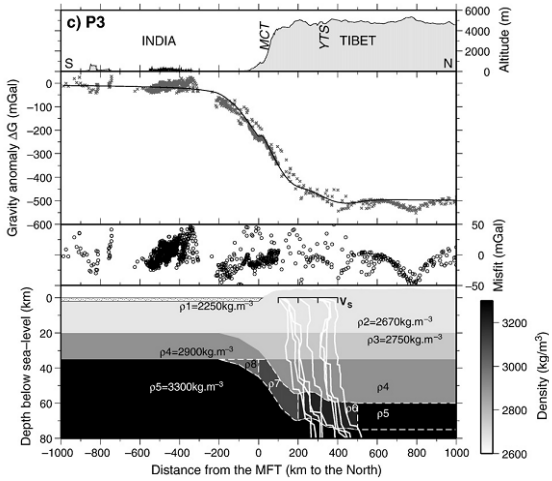

Jiménez-Munt et al. (2008) presented a 2-D lithospheric temperature structure and density model along a transect from the Indian plate to Asia, crossing the Himalaya front and the Tibetan Plateau (Fig.5.4). The model is based on the assumption of local (Airy) isostatic equilibrium, and it is constrained by the topography, gravity and geoid anomalies and by thermal data within the crust. Their results suggest that the height of the Tibetan Plateau is compensated by thick crust in the south and by hot upper mantle to the north. The Tibetan Plateau as a whole cannot be supported isostatically only by thickened crust; a thin and hot lithosphere beneath the northern plateau is required to explain the high topography, gravity, geoid and crustal temperatures. The lithosphere reaches a maximum depth of ~260 km beneath the southern Plateau, and thins abruptly northward to ~100 km under the central and northern Plateau. The lithosphere depth increases again beneath the Qaidam basin and the Qilian Shan to ~160 km.

As mentioned above, the structure of the Tibet is being investigated with manifold different approaches and at different sites. The 2D gravity models have given promising results, which can be expanded by a full 3D modeling. Furthermore, the density structures of the published studies have low lateral and vertical resolution, which we intend to improve in our 3D study. We integrate seismic with the gravity modeling, in order to obtain an improved understanding of petrological properties from the rock densities and velocities. This will allow us to have a better understanding of the actual physical state of the crust in this continent-continent collisional area. Many high-resolution seismic studies in Tibet (Xiong et al., 1985; Xiong et al., 1997; Zhao et al., 2001; Liu et al., 2003; Li, 2003; Zhang et al., 2002; Zhang et al., 2005) provide very good constraints on the geometry of crustal structure and the seismic wave velocity profiles which we use in our gravity modelling. In this study, Bouguer anomaly data are used to: 1) obtain the crustal density structure and to delineate the regional variations of the crustal structure in the subduction zone, 2) verify the eclogitization of the Indian lower crust, and 3) define the depth of the Moho and the flexure of the Indian shield.

5.4 Gravity anomaly datasets

The gravity data used in this study mainly are 10’×10’ gridded Bouguer anomalies, which are the same as used in Braitenberg et al. (2003). The grid data was based on the Chinese gravity network 85, with height reference of the Yellow Sea (Sun, 1989). The gravity data were reduced using the Helmert gravity formula. A complete terrain correction was made, with a maximum radius of 166.7 km and using a topographic density of 2.67 g/cm^3. In order to obtain data coverage over a rectangular grid, which necessarily goes beyond the Chinese border, the data were integrated with Bouguer gravity values derived from the IGG97L (Institute of Geodesy and Geophysics, CAS, Wuhan) earth gravity model (Hsu and Lu, 1995).

The gridded data have been integrated outside the Chinese territory with gravity data derived from the GRACE potential field (Shin et al., 2007) which is combined with the satellite derived gravity field and terrestrial gravity data.

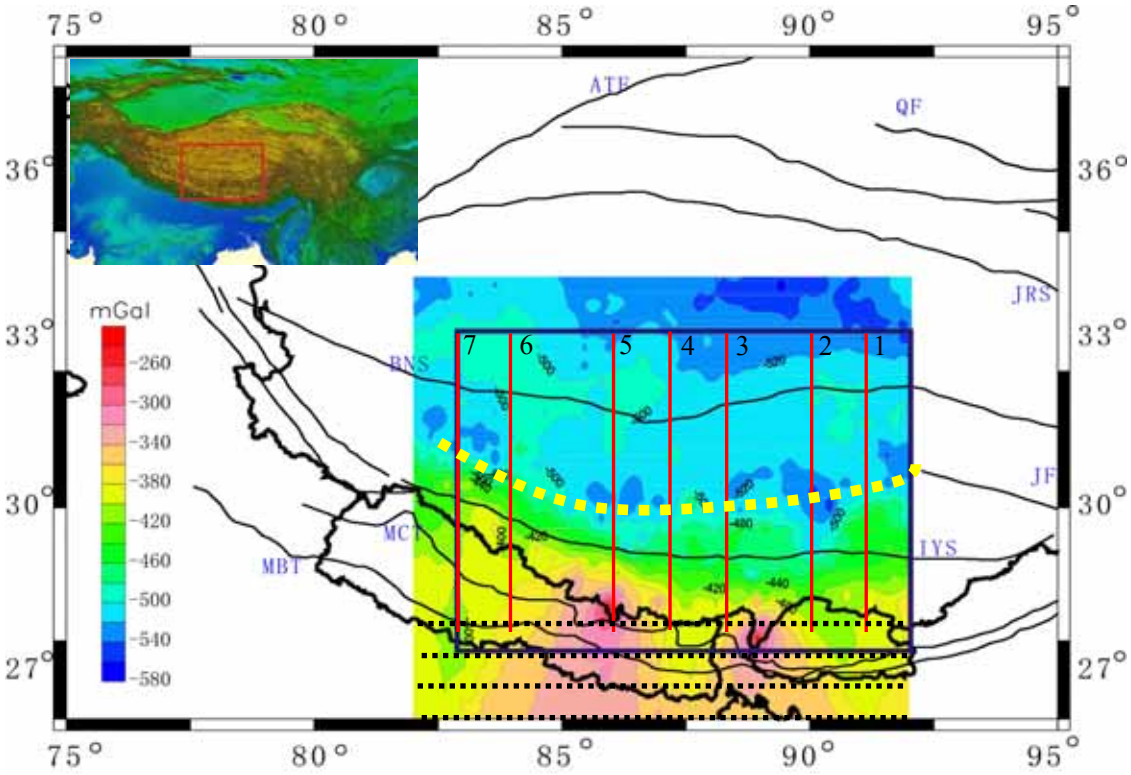

Fig.5.5 Bouguer anomaly data of the central-south Tibet. The black dotted lines mark the area where the terrestrial gravity data are unavailable. The yellow curve connects a series of gravity lows, which are placed above the supposed northern margin of the Indian plate (see Fig. 5.8)

The Bouguer anomaly varies between -574 mGal and -247 mGal in the study area. The difference reaches 327 mGal, which indicates large-scale variations in the crustal structure of the area. An extensive gravity low (longitude 86° -92° E and latitude 32 ° N-34° N) is located in the north-east of the study area. Four limited gravity lows are located in the Lhasa terrane, around (83° E, 31° N), (86° E, 30° N), (90° E, 30 ° N) and (82° E, 34° N), respectively. The gravity data along seven ~1000 km long profiles give similar trends with a ~500 mGal Bouguer anomaly decrease from the Himalaya crossing southern Tibet to the central Tibet.

5.5 Construction of the 3-D crustal density structure

5.5.1 Modelling technique

Forward modelling of the Bouguer anomaly was performed using the IGMAS software (Interactive Gravity and Magnetic Application System; see http://www.gravity.uni-kiel.de/igmas). The modelling software (Götze, 1984; Götze and Lahmeyer, 1988; Schmidt and Götze, 1998; Breunig et al., 2000) makes use of an interoperable 3-D Geoinformation System (IOGIS) and its functionality. The model is formed by 3-D bodies that are constructed using polyhedrals whose geometry is predefined by the user on a series of parallel vertical cross-sections, the 3-D structure is achieved in IGMAS by defining several vertical 2-D planes on which geological bodies are geometrically defined in the form of polygons (Schmidt, 1996). The 2-D vertical planes are connected via triangulation, thereby forming the 3-D structure. The geometry of the geological bodies is defined along the 2-D cross-sections, whereas the geometry in the area between them is interpolated. Hence, in order to perform more detailed modelling, a great number of 2-D cross-sections must be included.

Fig.5.6 illustrates the fundamentals of 3-D model construction. The starting model of the density structure follows the geometry of the seismic results and is defined by nodal points (with x, y, z-coordinates and density values) within cross sections arranged parallel to each other and covering the study area. The nodal points

define lines separating the density bodies within a certain cross section. The nodal points of corresponding lines within neighboring cross sections are automatically connected by triangulation, giving the surfaces of the density bodies. As another input, I have used the gravity data with a grid data file. In the south most part of the profiles, the Chinese gravity data are unavailable but have been integrated with published global data sets (Shin et al., 2007). In order to retain the measured information, the gravity effect of the modelled structures is calculated at the measurement points. The design of a 3-D density model in IGMAS incorporates three important decisions: the definition of the initial structure, the selection of density values for the bodies forming the model and the choice of a reference model.

The gravity effect of each 3-D (polyhedral) body is computed and added to the effect of the other ones, giving the anomaly value of the model structure for a given observation point. Generally, the levels of measured and computed gravity fields are different. To enable the comparison between the two fields an automatically determined constant shift value is added to the computed anomalies.

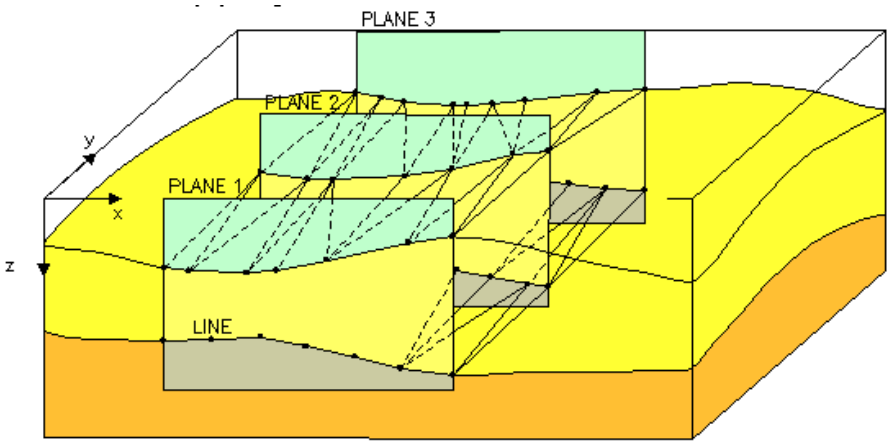

Fig.5.6 Illustration of 3-D model geometry for gravity computation with the software package IGMAS. (After Schmidt and Götze, 1998)

Initial density values for the modeled bodies are defined prior to the gravity modelling. By iteratively changing the geometry of the initial structure in accordance with the available constraining data incorporated in the IOGIS, the optimal fit between the observed Bouguer anomaly and the anomaly produced by the modelled

3-D density structure is achieved. This modelled anomaly is calculated from the density contrast between the modelled bodies and a layered background reference model.

5.5.2 Seismic-a priori information

The seismic data come from wide-angle seismic reflections, receiver functions, and tomography. These are used as a priori information for constructing the initial density structure.

5.5.2.1 The depth of Moho in the subduction zone

A seismic profile with 430 km length in central Tibet given by Teng et al. (1980a, 1980b) along the north-south direction near longitude 90° E provided the most detailed information for the crustal structure at that time. Teng et al. (1980a, 1980b) showed that the crust on two sides of the India-Yalunzambu suture (IYS) is significantly different. The crust is 70-73 km thick in the northern side of the IYS. A layer with P velocity of 6.0 ~ 6.2 km/s underlying a 4-5 km thick sedimentary layer, extends to a depth of about 45 km. A low-velocity layer of 5.6 km/s appears between the depth of 45 km and 55 km, underlain by a lower crust with about 7.2 km/s P wave velocity. The crust thins from 65 km to 45 km near Yadong in the south of IYS. In summary, the crust beneath the Himalaya is significantly thinner than the average crust in Tibet. The thinning of the crust continues southward to about 40 km under the Ganges Basin and to about 35 km under central India.

5.5.2.2 The Northern extent of the Indian Crust

The role of the Indian crust in doubling the thickness of the Tibetan crust is still a subject of debate. Makovsky's (1996) results tightened the geometrical constraint on the northern extent of the Indian crust (Fig.5.7). Three alternative conceptual models for the northern extent of Indian crust were discussed under the hypothesis that the Indian crust remains intact with a thickness of 30 to 40 km and that it penetrates north of the Tethyan Himalaya.

The first one is that the Indian crust flattens and underthrusts Asian crust to produce the double-thickness Tibetan crust (Fig.5.7, model 1) (Argand, 1924; Powell and Conaghan, 1973; Ni and Barazangi, 1984). The second model assumes that the Indian crust continues to dip to the north at the observed 7° to 10°, or only gradually steepens, and so underthrusts the IYS within the lower crust for about 100 km to the north but does not constitute the lower half of the Tibetan crust through central and northern Tibet (Fig.5.7, model 2) (Allègre et al., 1984; Harrison et al., 1992). In the last model the Indian crust is subducted into the mantle south of the IYS and does not constitute a part of the Tibetan crust (Fig.5.7, model 3) (Dewey and Burke, 1973; Molnar, 1988).

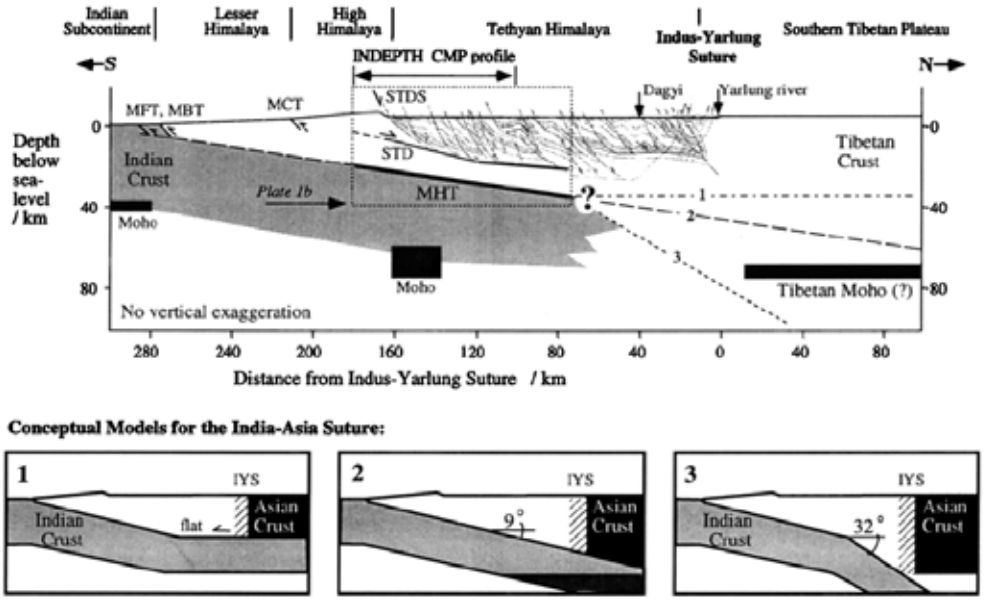

Fig.5.7 The model from INDEPTH-I projected onto a north-south line and combined into the general context of the Himalaya and southern Tibetan plateau.（After Makovsky, 1996）

The geometric constraints given by the INDEPTH-I wide-angle seismic reflection survey exclude the possibility of models 1 and 3. Therefore model 2 is preferred and it suggests that the Indian crust continues north of the Tethyan Himalaya and underthrusts the IYS within the lower crust. Makovsky (1996) observed the Main Himalayan Thrust (MHT) continuing with a uniform dip of 7° to 10° to a depth of about 40 km beneath the surface at a distance of only 70 km south of the IYS where

the Tibetan Plateau crust is 65 to 70 km thick.

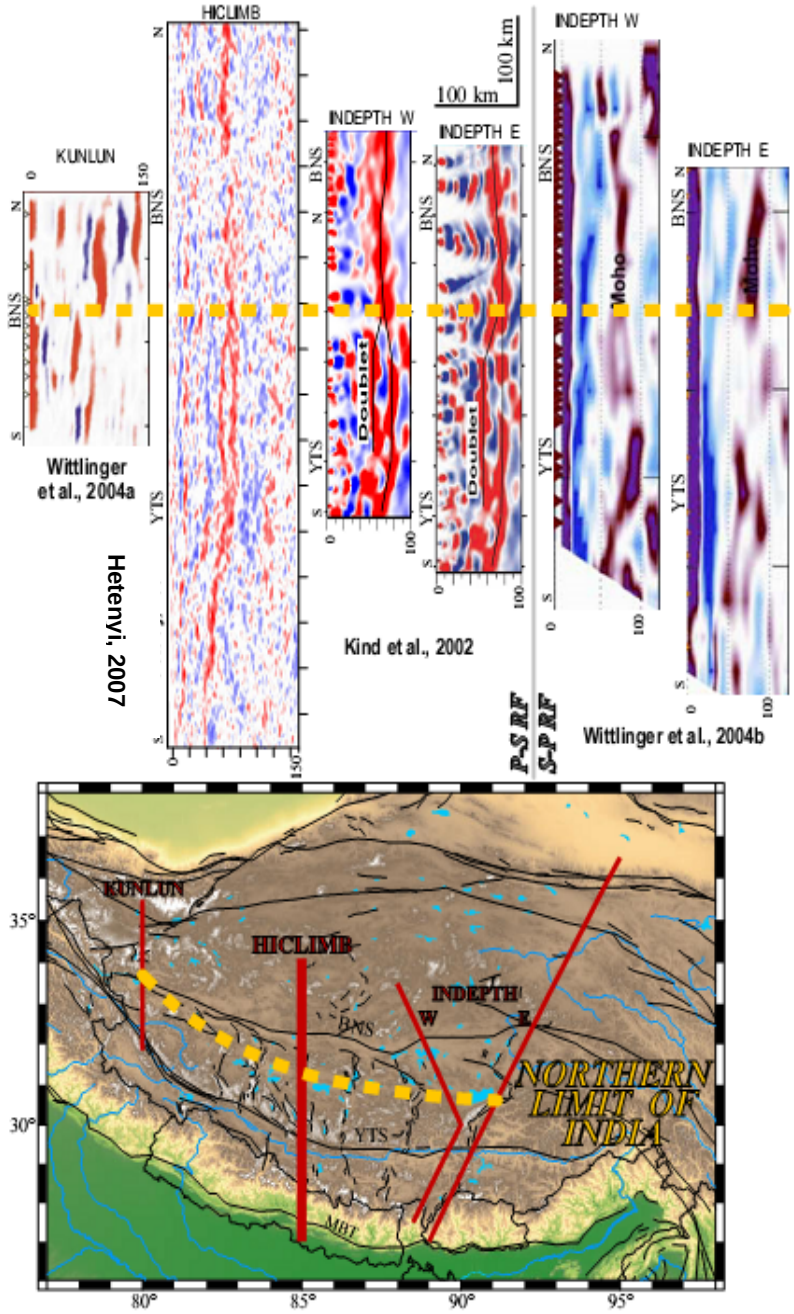

Fig.5.8 The northward extent of India. The Hi-CLIMB experiment's results (Nábělek et al., 2005) help to interpret profiles of earlier seismological experiments (in red lines) with less data at lower spatial resolution. The migrated profiles (top) constrain the position of the northern edge of India beneath the Tibetan Plateau(yellow dashed line) (After Hetenyi, 2007).

In addition, according to Hetenyi's study (2007), the results of Hi-CLIMB experiment gave a more appropriate answer to the northward extent of the India plate: the plate margin is located parallel to the Himalayan arc (Fig.5.8), and about ~450 km north of the Main Frontal Thrust. In the meantime, the comparison of six images

along four profiles shows that while the location where the Indian crust reaches its maximal depth can be approximately related to the Yarlung Tsangpo Suture, the position of the Banggong-Nujiang Suture with respect to the northern extent of the Indian lower crust is variable, with horizontal distances ranging between 0 and 150 km.

5.5.2.3 Layered crustal structure beneath Tibet

Seismic data provide valuable information not only on the geometry of crustal layers, but also on the depth distribution of P-wave velocities. In order to construct an initial density model, south-north trending velocity profiles (Fig.5.9) have been collected from:

- two deep seismic sounding profiles: Cuoqin-Sangehu (Line 8), Zhangmu- Cuoqin (Line 16);
- three near vertical deep seismic reflection profiles of INDEPTH project: Yadong-Namucuo (Line 1) from INDEPTH I and II, Deqin-Longwei Cuo (Line 10) from INDEPTH III;

Two east-west trending velocity profiles, Paiku Co-Puma Yumco (Zhang, 2002) (line 2) and Siling Co_Ya'anduo (Zhang, 2005) (line 3), will also be used to constrain the initial model and evaluate the final density model.

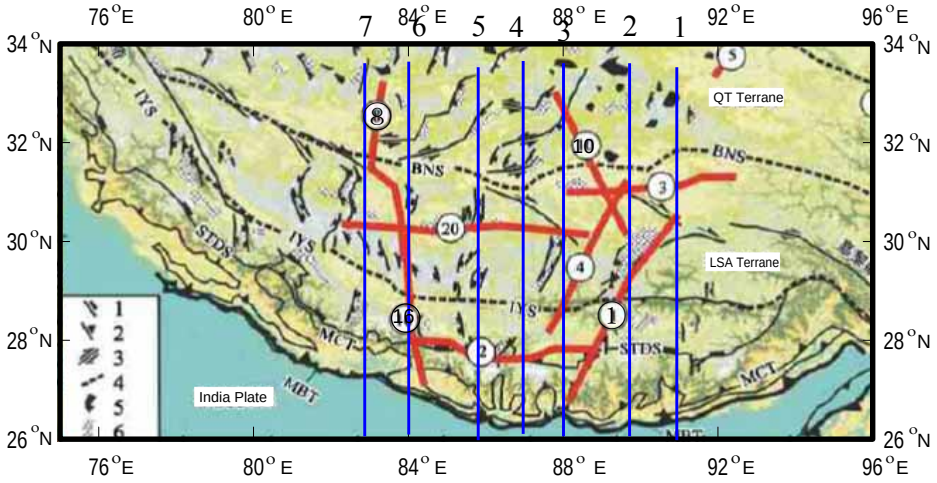

Fig.5.9 Red curves present location of studied seismic and seismological profiles. Seismic lines 1、2、8、10、3 and 16 are used in gravity modeling. Blue lines indicate the vertical planes used to construct the geometry and initial density structure of the 3-D model (Same as in Fig.5.5).

A 2-D velocity profile with 400km length located in 30.8° N—34.1° N and 84 ° E—85.2° E had been studied by wide-angle reflection seismics (Xiong et al., 1997). The profile showed the following crustal structure (Fig.5.10):

1) Thickness of the sediment layer: south of BNS, the sediment thickness is 9-11 km in Dongcuo basin and less than 6 km in Cuoqing basin. In Qiangtang terrane, the sediment is 3-4 km thick located in an uplift belt from Gaize to Lugu. In the north of Lugu, it is 7 km in the northern Qiangtang basin.

2) Upper/middle/lower crust: the upper crust is about 20 km thick with P-wave velocity range of 4.0-6.2 km/s. A 5-8 km thick low velocity zone (LVZ) with 5.8-5.9 km/s P-wave velocity shows a shear decollement zone. The middle crust is 11-22 km thick. A LVZ with 6.2-6.4 km/s P-wave velocity is found under the Dongcuo basin. This LVZ has high conductivity (Xiong et al., 1997) and relatively high Bouguer anomaly. The LVZ is inferred to be due to partial melting with the composition of mantle being basic-ultrabasic rock. This indicates that hot material from the deep mantle is transported to the crust under the Lhasa terrane.

3) Moho interface: in the north of the Lhasa terrane, the thickness is 75-78 km. The Moho interface in the Qiangtang terrane is at 65 km of depth, shallower than in the Lhasa terrane. Furthermore it presents a discontinuity.

4) The characteristic of BNS: the northward subduction of the mantle lid leads to BNS overturning northward.

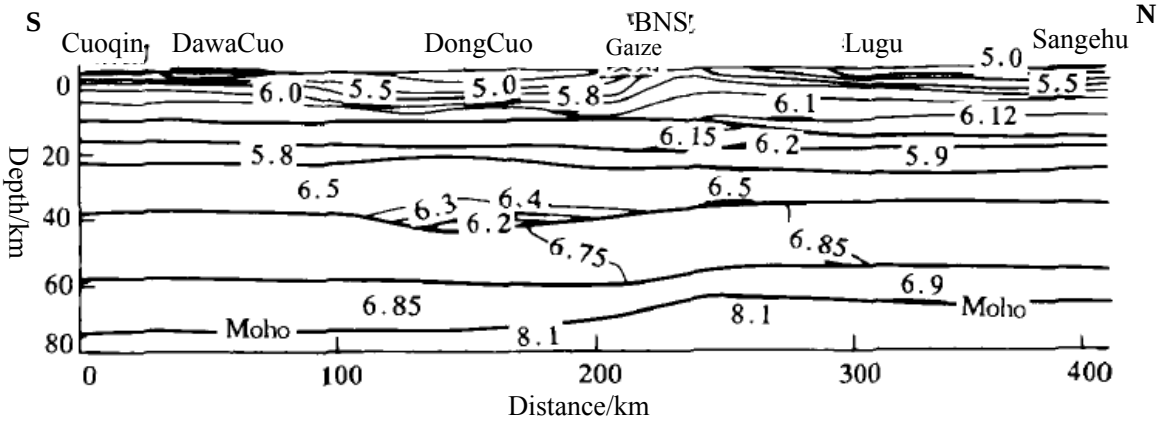

Fig.5.10 P-wave velocity profile (Line 8) located northwest of the study area. (After Xiong et al., 1997)

In the summer of 1998, project INDEPTH III recorded a 400 km length NNW–SSE wide-angle seismic profile in central Tibet, from the Lhasa terrane across the BNS at about 89.5° E and into the Qiangtang terrane (Fig.5.11). Analysis of the P-wave data reveals that: 1) the crustal thickness is 65±5 km beneath the profile; 2) there is no 20 km step in the Moho in the vicinity of the BNS, as has been suggested to exist along-strike to the east based on prior fan profiling; 3) a 20–35 km thick high P-wave velocity lower crustal layer is evident along the entire length of the profile; and 4) in contrast to the southern Lhasa terrane, there is no obvious evidence of a mid-crustal low-velocity layer in the P-wave data, although the data do not negate the possibility of such a layer of modest proportions.

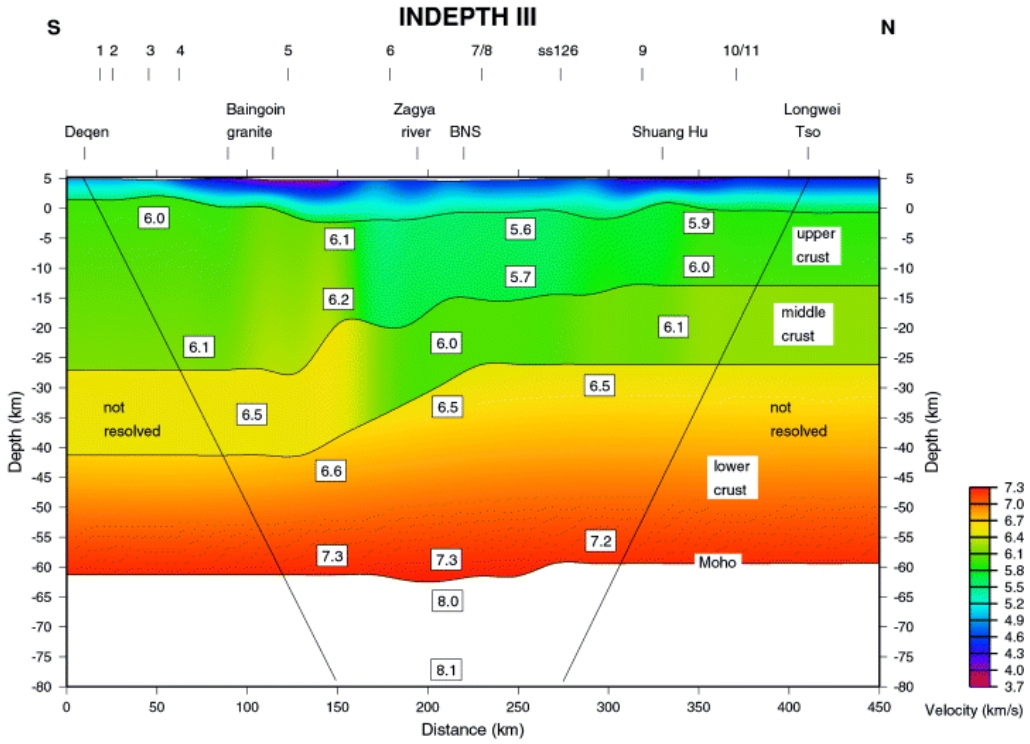

Fig.5.11 P-wave velocity model for the INDEPTH III profile (Line 10) in central Tibet. It will be used to control the structure in northeast part of the study area (After Zhao et al., 2001).

Based on wide-angle reflection/refraction seismic survey, Liu (2003, unpublished) proposed a profile (Line 16) from Zhangmu to Cuoqing in southwest Tibet (Fig. 5.12). A high velocity zone with 20-30 km width is located near Shaga. In the south of IYS, Peigu Cuo is located in a depression zone. However, in the north of IYS, the layers of

the entire Lhasa terrane is flat and only undulate in the shallow layers. The crust is 70-78 km thick and its average crustal P-wave velocity is 6.25-6.3 km/s. The P-wave velocity of the sediment layer varies in the range of 3.2 and 6.2 km/s. The upper crust thickness is 25-35 km and it is shallow in the southern part and thicker in the northern part of line 16. The middle crustal velocity is 5.8-6.5 km/s with 15-20 km thickness. A LVZ with 5.7-5.8 km/s P-wave velocity exists in the top of the middle crust. The lower crust is 25-30 km thick with about 6.8 km/s P-wave velocity. Moho interface is continuous beneath the IYS. It deepens from the south ending of the profile with 70 km depth to the northern ending with 78 km depth (near Dajia Cuo). The Moho interface deepens between Shaga and Dajia Cuo (along profile distance of 200 km) and rises abruptly to around 73 km over the distance of 250 km. The vertical offset of Moho interface is 5 km.

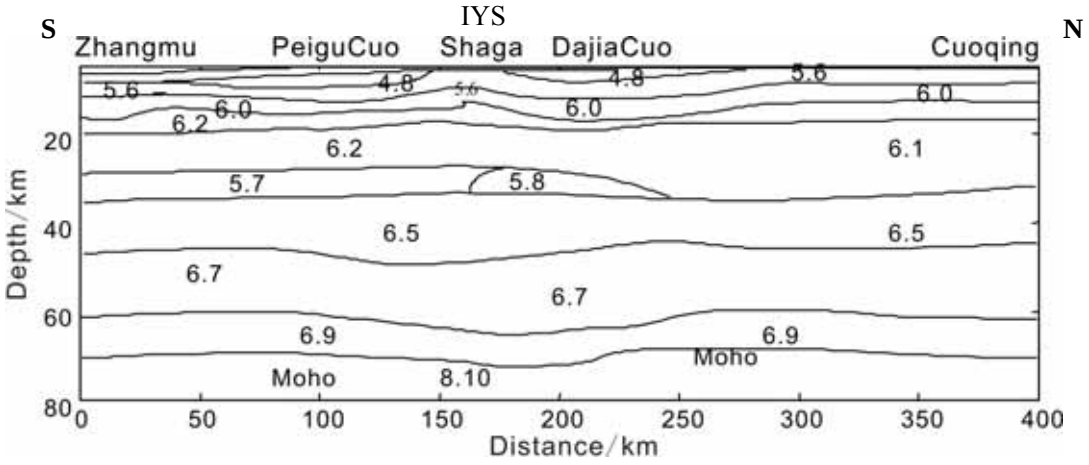

Fig.5.12 P-wave velocity model for the profile (Line 16) in southwest of the study area. (After Liu, 2003) (personal communication)

Another velocity model along seismic line 1 is obtained by reprocessing the INDEPTH I and II data using the ray tracing modeling method (Li, 2003). The INDEPTH seismic reflection profile (Fig.5.13) showed that the decollement beneath which Indian lithosphere underthrusts the Himalaya extends at least 225 km north of the Himalayan deformation front to a depth of ~50 km. Prominent reflections appear at depths of 15 to 18 km near where the decollement reflector apparently terminates. These reflections extend north of the IYS to the Damxung graben of the Tibet Plateau. Some of these reflections have locally anomalous amplitudes (bright spots) and

coincident negative polarities implying that they are produced by fluids in the crust. The presence of geothermal activity and high heat flow in the region of these reflections and the tectonic setting suggest that the bright spots mark granitic magmas derived by partial melting of the tectonically thickened crust. In addition, the crustal structure beneath the line 1 is depicted as follows:

1) at shallow depths (less than 20 km), P-wave velocity is higher between IYS and BNS than in Tethys Himalaya to the south of IYS;
2) at intermediate depths (20-40 km), the thickness of a LVZ (smaller than the middle crustal P-wave velocity with 6.4 km/s in continental crust, the offset is 0.1~0.2 km/s) increases northward and reaches 30 km of thickness.
3) The P-wave velocity is close to a normal value (6.7~6.9 km/s) in the lower crust of Lhasa terrane. It is underlain by a 20 km thick crustal and mantle mixture zone with 7.4 km/s P-wave velocity.

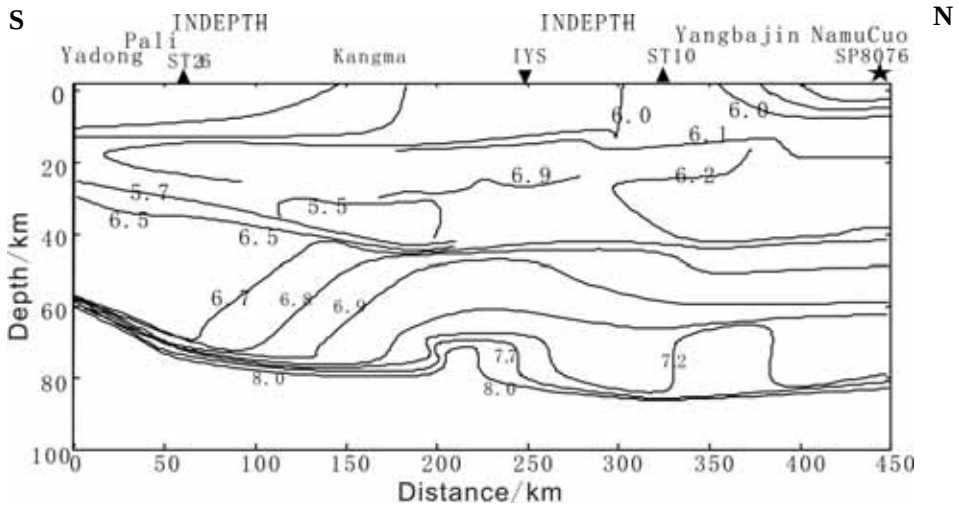

Fig.5.13 P-wave velocity model for the profile (Line 1) in southeast of the study area. (After Li, 2003)

The entire above seismic wave velocity interpretations are incorporated in this work in the process of constructing the 3-D gravity model for the transition zone between the Indian plate and the Eurasia plate. The modeling of potential fields will not only provide a more complete understanding of the crustal architecture, but also try to infer the physical properties and possible composition of anomalous crustal

materials.

5.5.2.4 Lithosphere-Asthenosphere boundary

As it is well known, the greatest density contrast in the lithosphere is located at the Moho interface, followed by the sediment-basement interface. Previous works (Jin et al., 1996; Braitenberg et al., 2000) have estimated the gravity effect of lithospheric thickening and have shown that over the Tibet plateau the gravity effect is almost constant, with variation of about 10mGal. Although the effect of the lithospheric thickening is very small, as the density contrast of the lithosphere to the asthenosphere (assumed as 0.03 g/cm^3) is less than one tenth of the value at the Moho (Shin, 2007), the asthenosphere layer is still considered in the modelling of this study.

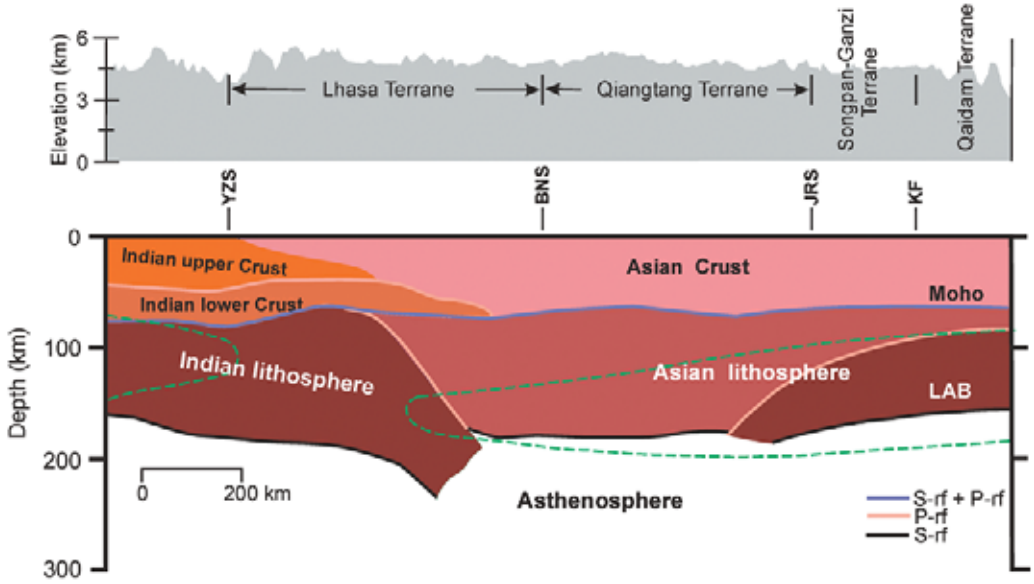

Fig.5.14 Sketch map of the collision of the Indian and Asian lithospheric plates from the results of S receiver function (S-rf) analysis and P receiver function (P-rf) results (After Kumar, 2006).

Kumar et al. (2006) presented a high-resolution image of the base of the lithosphere from S-to-P converted seismic waves, revealing the collision architecture of the Indian and Asian continental plates beneath the Tibet Plateau. The base of the Indian lithosphere dips northward from a depth of 160 km beneath the Himalayas to a depth of 220 km just south of the BNS. The base of the Asian lithosphere is nearly horizontal at the depth of 160-180 km from central to northern Tibet. There is a

vertical gap of about 50 km between Indian and Asian lithospheres. Fig.5.14 shows the subduction of both the Indian and Asian lithospheres. The Indian plate is penetrating into the mantle to the south of the Bangong suture (BNS). This lithospherical model will be used in our gravity modeling for the constraint of the lithosphere-asthenosphere boundary.

5.5.3 Model construction

An initial crustal model is constructed by compiling available seismic and other geophysical data. The degree of freedom in modifying the geometry of the crustal layers depends on the availability and quality of seismic data. The study area was modeled with 7 south–north oriented and c.a. 900 km long cross-sections, with spacing interval of 1 or 2 degree (Fig.5.5). From east to west, the model structure is c.a. 1000 km wide. To suppress edge effects, the density model was extended in all directions with the last given values for up to 1500 km. Depth extension is 260 km. None of the sections runs parallel to one of the seismic lines, but crosses them. The initial density model structure is taken from the seismic structure as given at these cross points. It also follows that the western part (to the west of 86° E) is best controlled by the seismic line 8 and 16. The eastern part (to the east of 86° E) is weakly controlled by the seismic line 10 and 1, i.e., the initial density profiles are constructed following four seismic lines (line 1、8、10 and 16): the north parts of planes p1-p4 are controlled by line 10, the south parts of p1-p4 (see Fig.5.9) by line 1; the north parts of p5-p7 (see Fig.5.9) are controlled by line 8, the south parts of p5-p7 by line 16.

5.5.3.1 Petrophysical parameters

Initial crustal densities have been calculated at some sites along 7 north-south trending profiles (see Fig.5.5) from the proposed seismic velocities (Vp and Vs) and using the velocity - density relation of Christensen and Mooney (1995). The values of the physical properties considered for each body are listed in Table 5.1.

Table 5.1 Physical parameters of the different bodies used in the initial modelling

Description	ρ(g/cm^3)	V(km/s)
Tertiary Indian foreland basin	2.45	Vs=2-2.75 (Mitra et al., 2005)
India UC-lesser Himalayan	2.7-2.89	Vs=3.5-3.8 (Mitra et al., 2005)
Greater Himalayan belt	2.75-2.91	Vs=3.4-3.8 (Mitra et al., 2005) Vp>5.7 (Hauck et al., 1998)
Tethyan Himalayan sequences	2.65-2.7	Vs=2.5-3.2 (Mitra et al., 2005) Vp=5.2 (Hauck et al., 1998)
Gangdese Batholith	2.75	
Lhasa terrane UC	2.7-2.93	Vp=6–6.5 (Meissner et al., 2004) Vp=6.1–6.5 (Zhao et al., 2001)
Qiangtang Basin, sediments	2.5-2.6	density (Haines et al., 2003) Vp~5.7 (Meissner et al., 2004)
Qiangtang terrane UC	2.64-3.01	density (Haines et al., 2003) Vp~5.8–7 (Meissner et al., 2004) Vp~5.6–6.5 (Zhao et al., 2001)
Songpan–Ganzi terran, Kunlun	2.6-2.85	Vp=5.4–6.2 (Jiang et al., 2006)
Qaidam Basin	2.4	Vp=5–5.5 (Zhao et al., 2006)
Qaidam–Qilian Shan UC	2.53-2.92	Vp=6–6.3 (Jiang et al., 2006) Vp=5.5–6.5 (Zhao et al., 2006) Vp=5.5–6.3 (Gao et al., 1999)
India LC	2.98	Vs=3.9 (Mitra et al., 2005)
Greater Himalayan LC	3.05	Vs=4–4.2 (Mitra et al., 2005)
Lhasa–Qiantang LC	3.05	density (Haines et al., 2003) Vp=6.6–7.1 (Meissner et al., 2004) Vp=7–7.3 (Zhang and Klemperer, 2005) Vp=6.5–7.3 (Zhao et al., 2001)
Qaidam–Qilian–Beishan LC	3.0	Vp=6.5–6.8 (Jiang et al., 2006)
Lithospheric mantle	3.2	

5.5.3.2 The reference model

The measured gravity is influenced by the mass of the entire Earth, whereas only a part of the Earth is considered (typically the upper tends to hundreds of kilometers) in density models. Hence, the modelled space does not include all the masses below and around the measurement points. For this reason, the levels of the observed and modelled values are not identical. Additionally, the use of absolute density values,

which are directly comparable with seismic velocities, increases the offset of the observed and modelled values even more. This offset can be computed and removed automatically by the IGMAS program. Another possibility to remove the offset is to introduce a reference model in the background of the density model (Ebbing et al. 2001). The reference model has a few layers representing the structure of the normal Earth, but extends to the same depth as the 3-D model and its densities are assigned negative values. The modelled densities are then relative to this reference model.

The selected reference model (parameters are listed in Table 5.2) is constrained by the studies of Christensen & Mooney (1995) and Rudnick & Fountain (1995). The densities of each layer of the reference model are also shown in Fig.5.15. The continental crust is divided into two layers with densities of –2.7 and –3.1 g/cm^3 for the upper and lower layer respectively. The upper crustal layer is 35 km thick and the lower crustal layer is 13 km thick, thus producing 48 km thick crust with an average density of –2.81 g/cm^3, which is closer with the global average (Christensen & Mooney 1995) and with the crustal structure of the orogens. The mantle extends to a depth of 260 km and its density is set to be –3.32 g/cm^3.

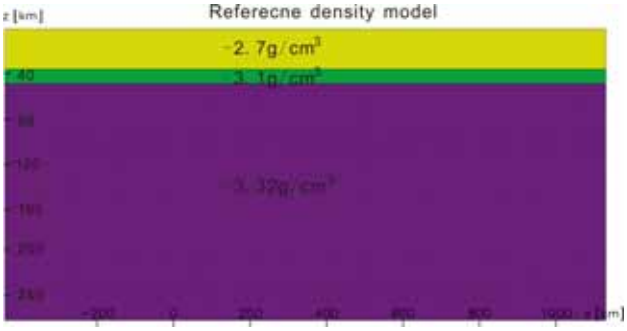

Fig.5.15 The reference model has a three layers representing the structure of the normal Earth

Table 5.2 Depth and density parameters of the reference model used for gravity modelling

	Depth (km)	Density (g/cm^3)
Upper crust	0-35	-2.7
Lower crust	35-48	-3.1
Mantle	48-260	-3.32

5.5.3.3 Initial density structure (model I)

An initial crustal model based mainly on available seismic data was constructed to start the lithosphere modelling. The geometry of the different crustal layers inferred from seismic profiles was discussed in the section 5.4.2. The gravity anomaly was calculated for the initial density structure (Fig.5.16) according to the relationship

between velocity and density in Table 5.1. The gravity stations are placed at their measurement heights above sea level, but the topographic body was not included in the model because its effect on the gravity attraction was already subtracted by the Bouguer and terrain corrections. The modeling result shows that the initial density model does not match the observed data completely. It demands further modelling by adjusting geometry of interfaces and inverting densities iteratively.

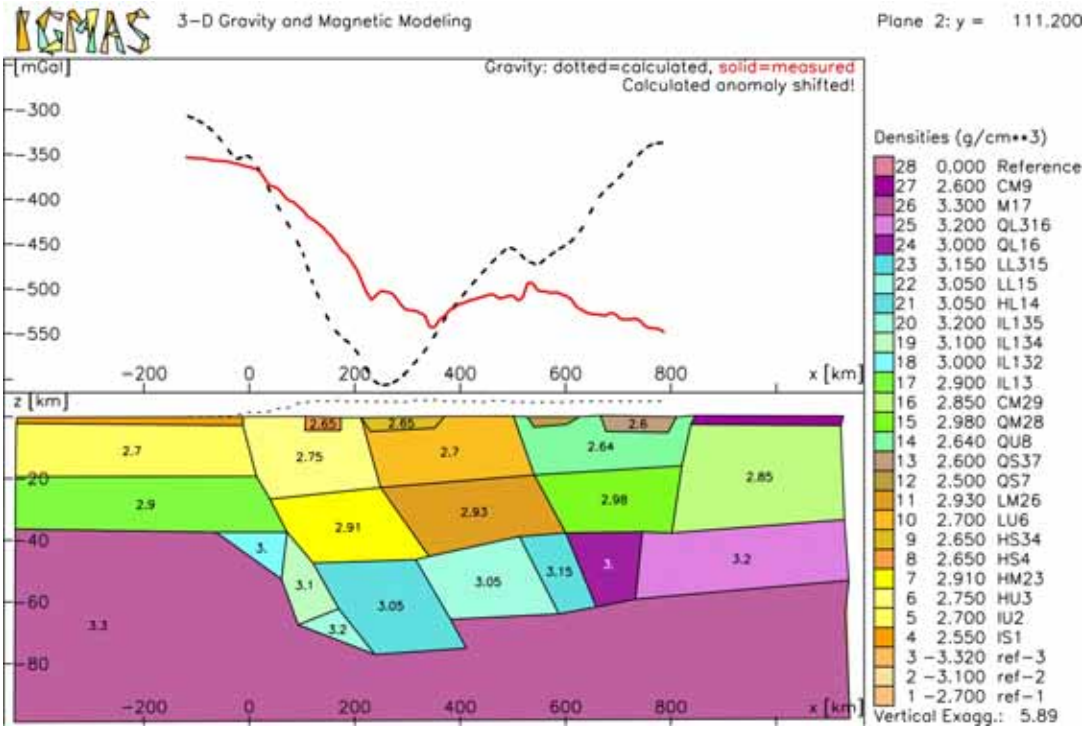

Fig.5.16 The eastern cross-section of the initial model. Densities are deduced from P-wave velocity following Table 5.1.

Velocities in the upper crust are mainly influenced by the presence of cracks and fractures, possibly filled with fluids, that decrease the observed seismic velocities. Therefore, if a standard density-velocity relationship is applied, the densities obtained might be underestimated.

5.6 Modelling Results

5.6.1 Preliminary density model with fixed geometry structure

In the initial model, the unit QL316 (Qaidam lower crust, for details see the

caption of Fig.5.19) should be noticed for its high density value (3.2 g/cm^3). Since seismic and seismological investigations have proposed a thick crust over 40 km and unit QL316 is located in the lower crust, the density of unit QL316 should be decreased in order to match the gravity field. The optimal value is estimated to be 3.05 g/cm^3. In order to fit the observed Bouguer anomaly data, the interfaces have been changed by less than 2 km. Cross-section of a better fitting density structure is shown in Fig. 5.17.

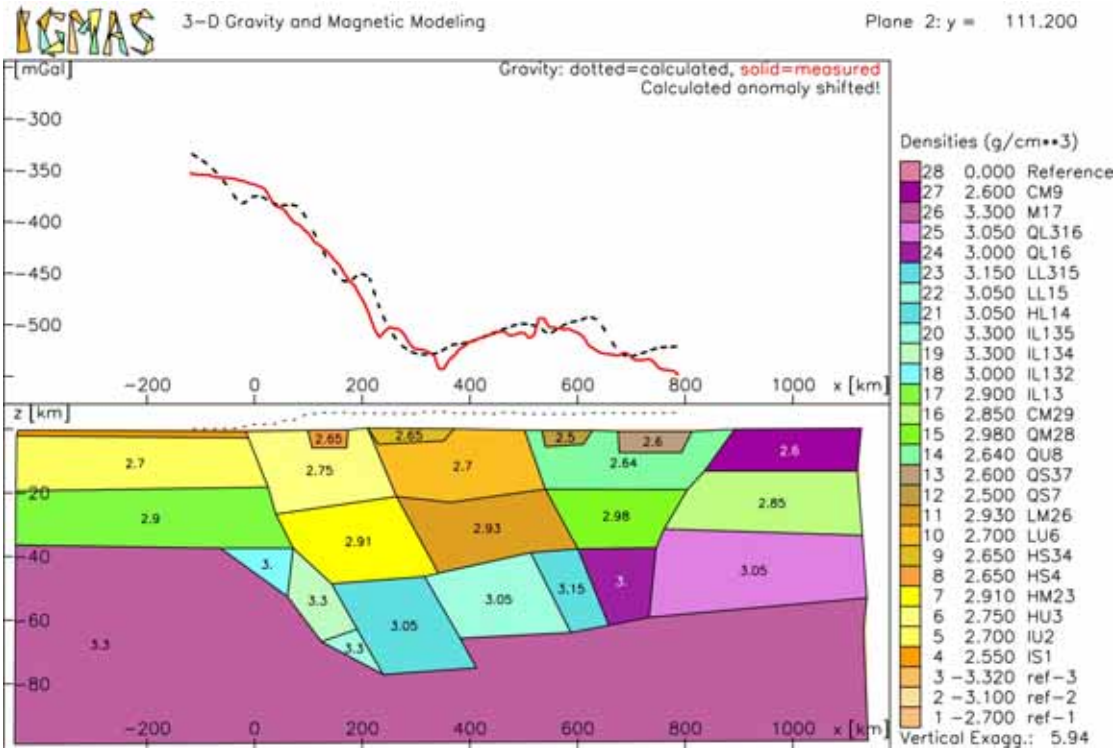

Fig.5.17 The eastern cross-section of model II. Density of some units and the geometry of interfaces have been changed with respect to model I.

The model II is in good agreement with the observed data with the exception of some misfits that are either local or at the border of the model. The main negative anomalies of the contact zone between the Indian and Eurasia plates are properly reproduced. The residuals of observed and calculated Bouguer anomalies are around zero with a standard deviation of 31.4 mGal, which is 5.4% of the maximum Bouguer anomaly (-580 mGal) and the correlation coefficient is 0.9 between the observed and calculated Bouguer anomaly. We determine the final geometry of the crustal structure from the model II.

The accuracy of the 3-D density model presented is quantified in terms of how well it reproduces the observed gravity anomalies. However, this does not say anything about the validity of the modelled structures, particularly in the areas where no other geophysical data are available. Due to the non-uniqueness of the interpretation of potential fields, other models with different structure and density distribution could also reproduce the observed anomalies with the same accuracy, although they would be hardly probable, due to the fact that continuity of the crustal structure and of its layers exists. The further evaluation of the model needs integration with reliable geological and geodynamical information. Due to the fact that densities in middle crust and lower crust are higher than global average values, eclogitization will be discussed in the next section.

5.6.2 Absence or presence of eclogitization

Eclogitization beneath Tibet is a subject of broad interest in the field of earth sciences. Previous studies have shown that eclogitization of the lower crust is a key process in support of the high elevation of both Himalayas and Tibet (Bousquet et al., 1997; Henry et al., 1997; Cattin et al., 2001; Tiwari et al., 2006; Hetenyi, 2007 (Fig.5.18)). In the north of the Himalaya, the lower Indian crust is characterized by a high-velocity region consistent with the formation of eclogite and a high-density material whose presence affects the dynamics of the Tibetan plateau (Schulte-Pelkum, 2005). However, several seismic studies have inferred abnormally low, rather than increased, velocities for the Tibetan lower crust (Sapin et al., 1997; Cotte et al., 1999; Zhao et al., 1996), suggesting an absence of eclogite. Gravity modeling will be an extra constraint on the absence or presence of eclogitization in this study.

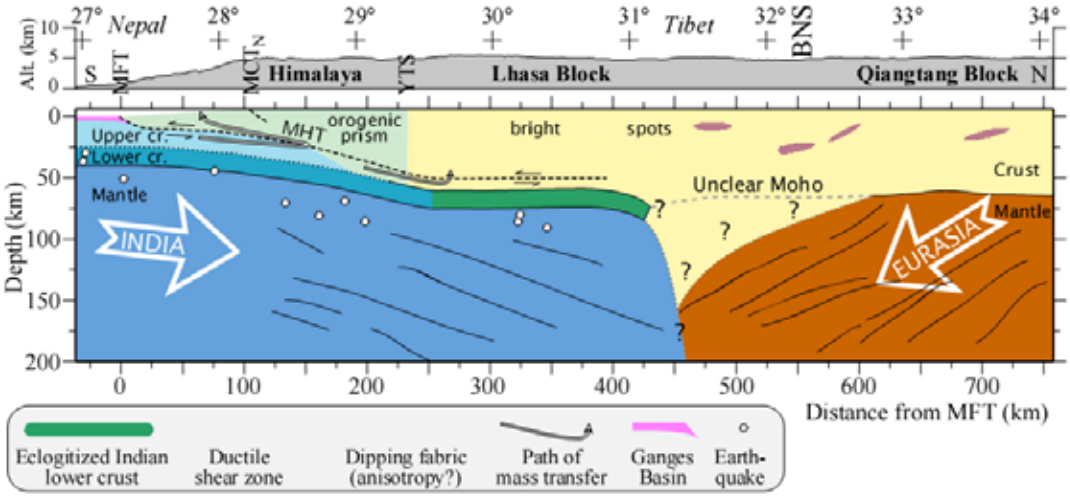

Fig.5.18 Interpretative scheme of the India-Eurasia collision zone as seen by the Hi-CLIMB experiment. The Indian lithosphere goes underneath the Tibetan Plateau at ~450 km, including its lower crust which undergoes eclogitization. (After Hetenyi, 2007)

An end-member model (Fig.5.19) is designed with eclogite in the lower crust, with the same geometry as in model II. The calculated gravity anomaly is larger than the observed data, when using the model with lower crustal density over 3.3 g/cm^3 beneath the Himalaya and Lhasa terrane. In order to match the calculated gravity anomaly with the observed data, the lower crustal densities are reduced. Finally, model III is created and its average lower crustal density is less than 3.2 g/cm^3. Fig. 5.20 presents the eastern profile with the whole lithosphere structure of model III.

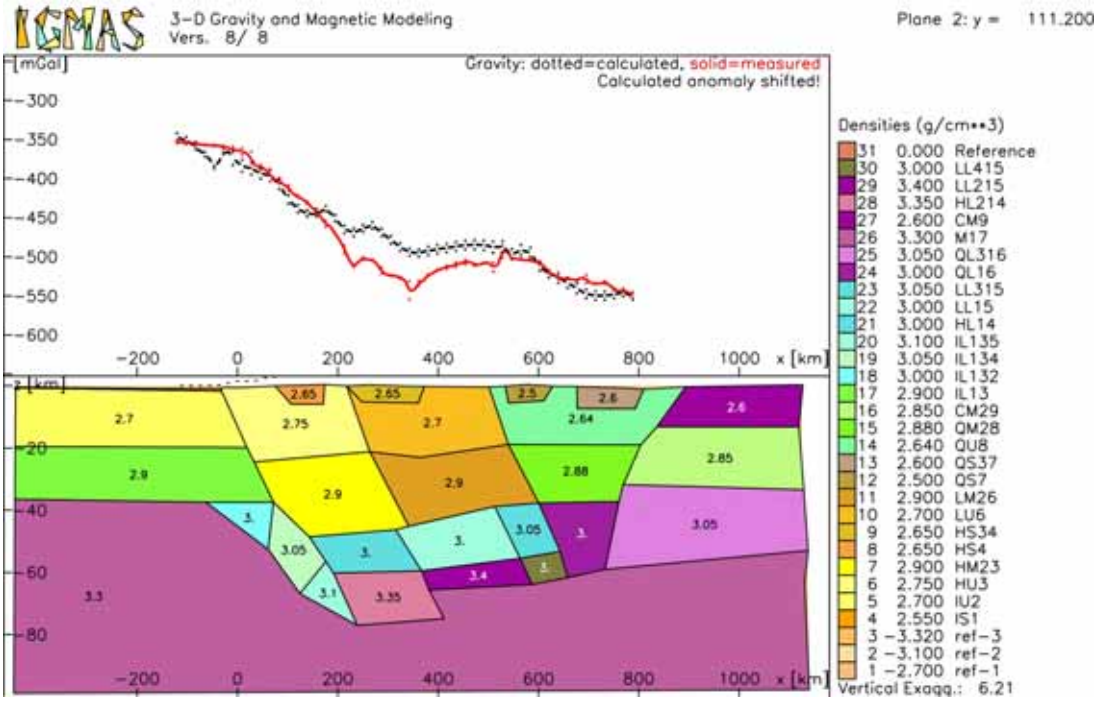

Fig.5.19 An end-member model for the eclogitization of lower crust.

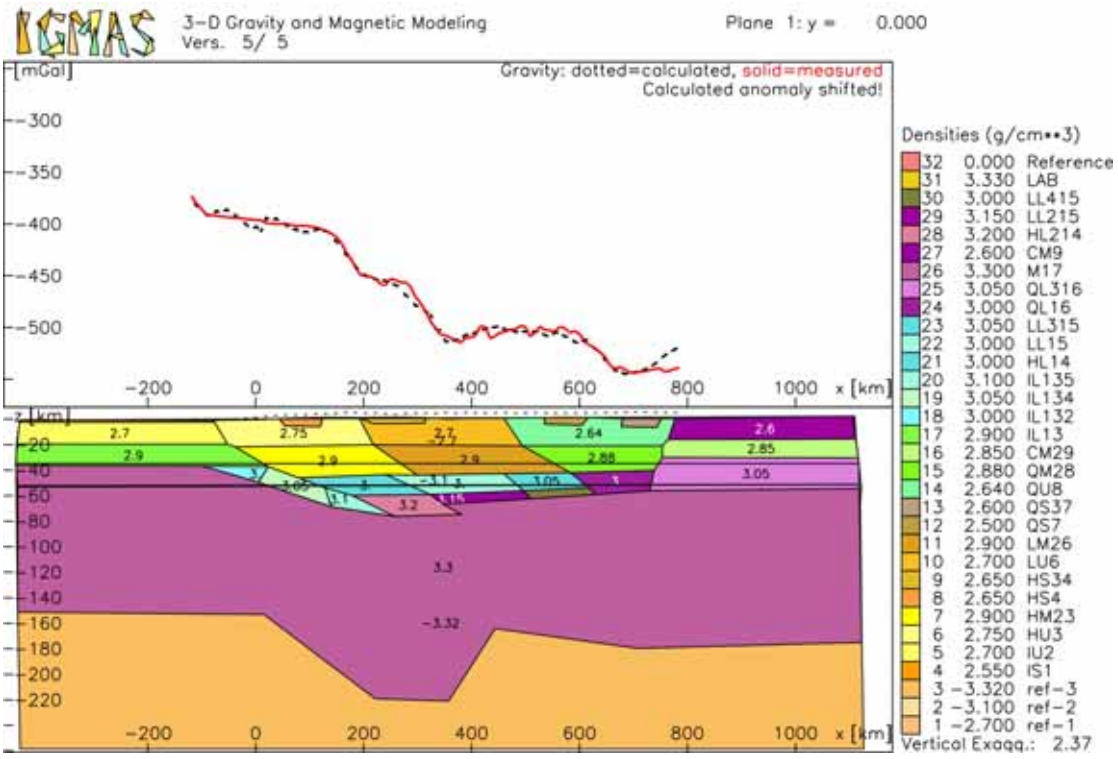

Fig.5.20 The eastern profile with the deep lithosphere structure of model III.

Model III is our preferred model after several tests following a trial-and-error approach. The calculated Bouguer anomaly is in good agreement with the observed

data, with the exception of few local misfits. A comparison between the observed and calculated gravity anomaly maps over the 3-D model is shown in Fig. 5.21 a). The main negative anomalies of the contact zone between the Indian and Eurasia plates are properly reproduced like in model II. The histogram (Fig. 5.21 b)) shows a tight concentration of residuals around zero with a standard deviation of 29.45 mGal, 5.1% of the maximum Bouguer anomaly (-580 mGal) and correlation coefficient is 0.9 between the observed and calculated gravity anomaly data. Fig.5.22 shows the unit IL13 has maximum volume and mass.

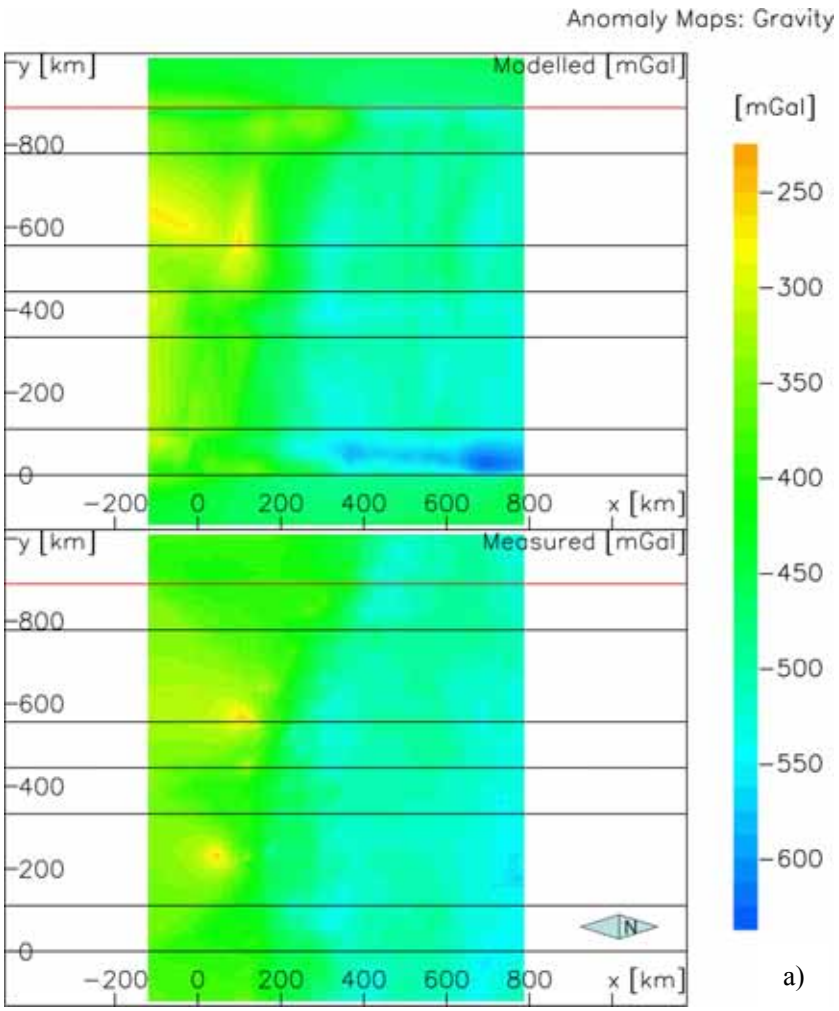

a)

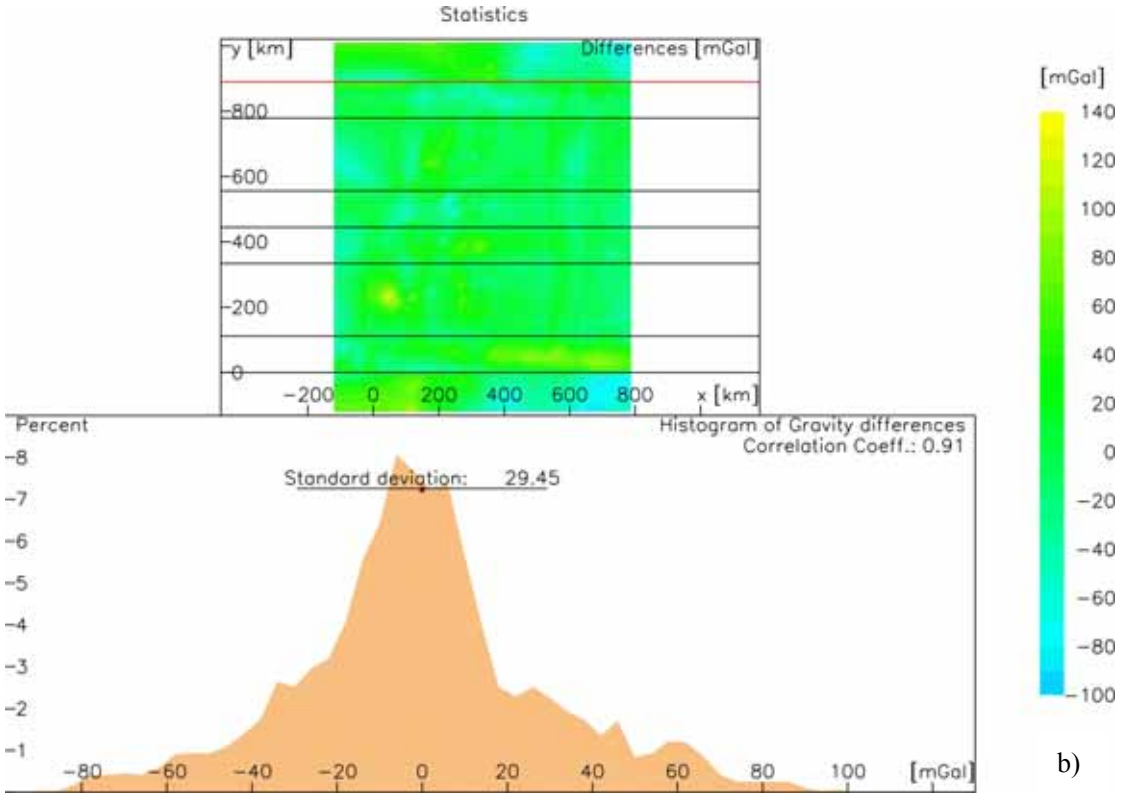

b)

Fig.5.21 a)Observed and calculated gravity anomalies for model III in the study area. b) Mismatch between observed and calculated anomalies and histogram of gravity difference. Black lines still indicate the vertical planes used to construct the geometry of the 3-D model.

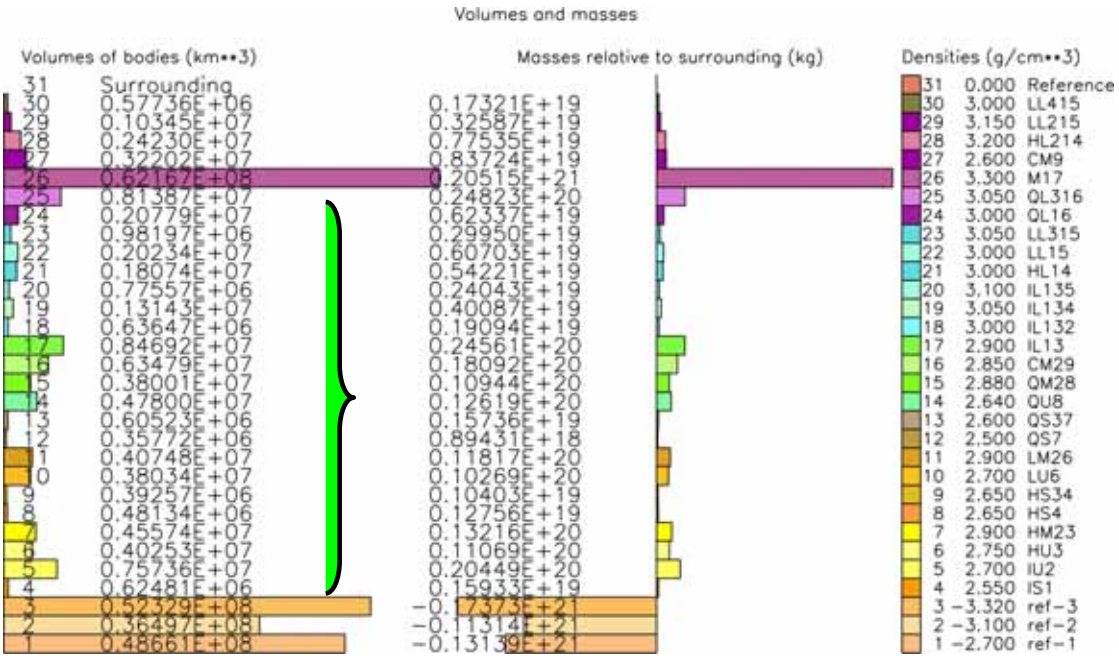

Fig.5.22 Statistics of volumes and masses for all units.

5.7 Discussion and conclusions

A 3-D crustal model has been derived for the transition zone between the Indian plate and the Eurasia plate beneath Tibet. The model is seismically constrained and explains the main gravimetric anomalies over the area. The tectonic implications of this study are discussed hereafter.

5.7.1 Model evaluation by comparison with other geophysical data

The boundaries between the density layers of the model match well with the interfaces of the shear wave velocities gradient. The crustal velocities of inset (2) (Fig.5.23 a)) are from INDEPTH III (Zhao et al., 2001) and density was calculated using the velocity-density regression parameters of Christensen and Mooney (1995). The average Moho depths of Lhasa terrane and Qiangtang terrane in model III are close to the result of INDEPTH III experiment. The modelled densities are slightly lower than those deduced from the velocity-density regression parameters. Comparing the modelled structure with a east-west profile (inset (3) in Fig.5.23 a)), which intersects the velocity profile at km 260, which corresponds to km 435 of the density profile, we find that the offsets are less than 4 km.

In Fig.5.23 b), the interfaces of the top of the lower crust and Moho have 2km offset with respect to the result of the receiver function (Yuan et al., 1997). Through the sensitivity test of gravity modeling, we find that the anomaly is not sensitive to the 2km offset in the depth of ~70 km. So this offset is negligible when applying the gravity method.

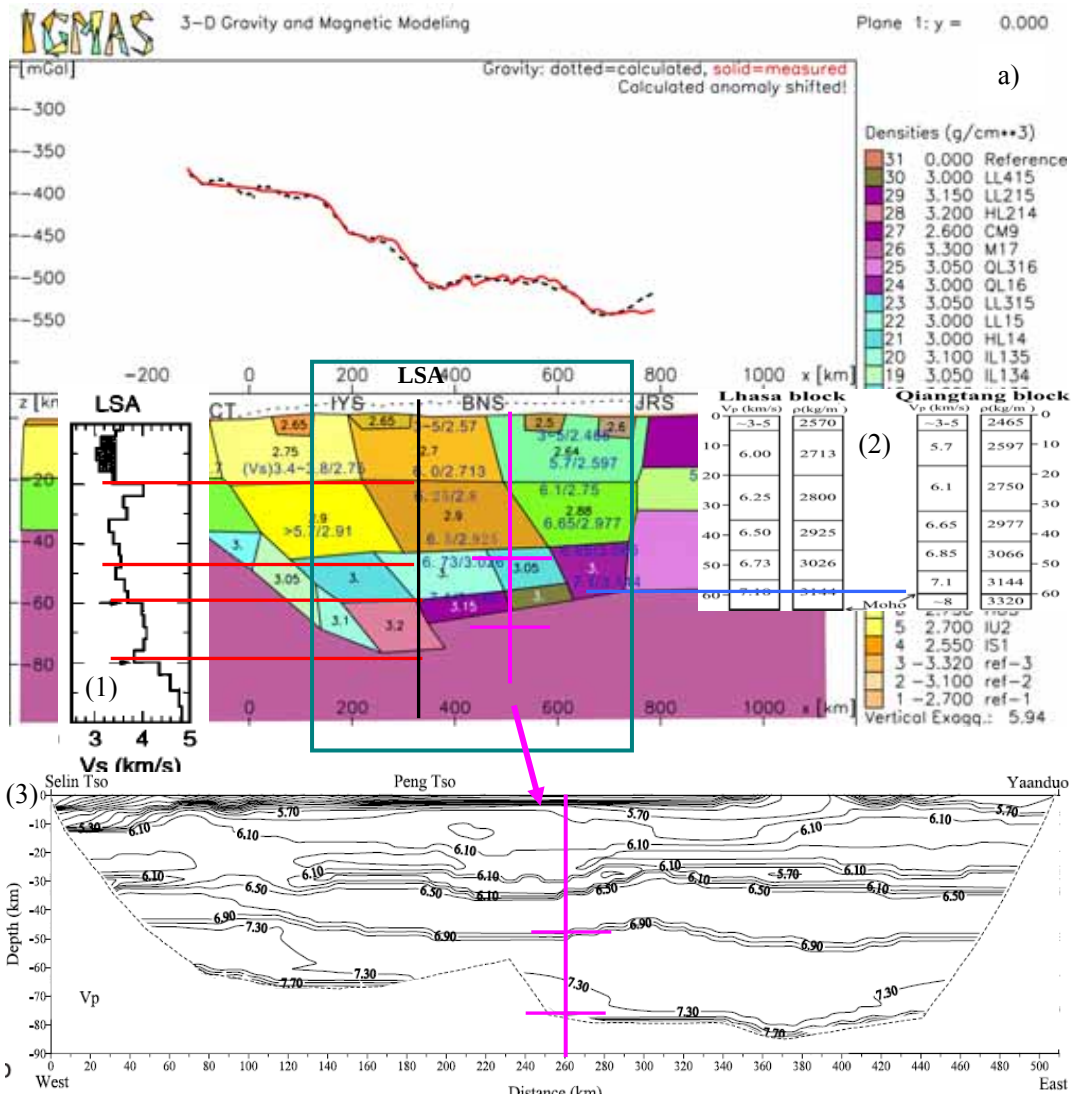

Fig.5.23 a) Basemap shows profile P1 of the modelled density structure with black numbers as densities and blue numbers as the seismic-wave velocities and its deduced densities. Black line shows the position referred in inset (1); Blue rectangle marks the area referred in inset (2). Left inset (1) is a 1-D shear wave velocity (after Yuan et al., 1997) for permanent station LSA using receiver function method. Right inset (2) is velocity (Vp) and density (ρ) columns for the Lhasa and Qiangtang blocks (after Haines et al., 2003). The bottom figure (3) is 2-D east-west P-wave velocity profile of wide angle seismic reflection experiment (Zhang et al., 2001). Detailed explanation see text. b) Basemap shows profile P2 of the modelled density structure. Inset shows the 1-D velocity-depth of the receiver function study.

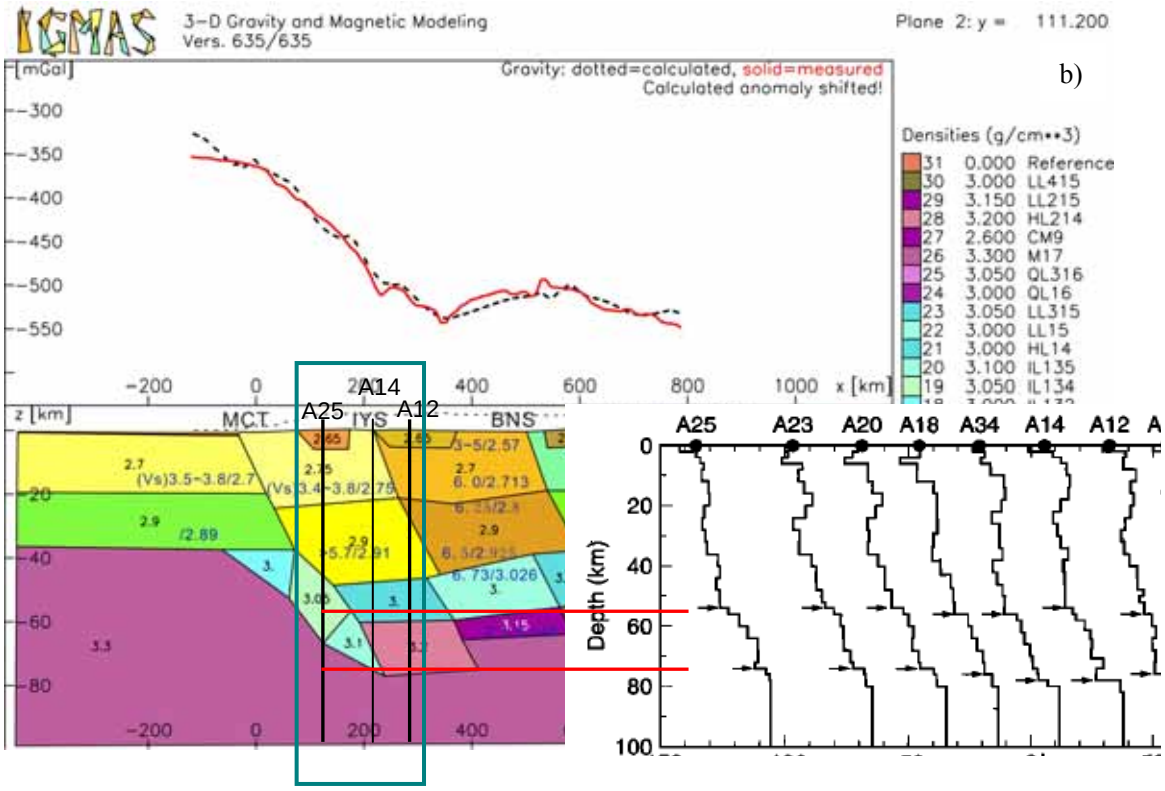
3-D Gravity and Magnetic Modeling
Vers. 635/635
Plane 2: y = 111.200
b)
Gravity: dotted=calculated, solid=measured
Calculated anomaly shifted!
[mGal]
Densities (g/cm**3)
31 0.000 Reference
30 3.000 LL415
29 3.150 LL215
28 3.200 HL214
27 2.600 CM9
26 3.300 M17
25 3.050 QL316
24 3.000 QL16
23 3.050 LL315
22 3.000 LL15
21 3.000 HL14
20 3.100 IL135
19 3.050 IL134
x [km]
z [km]
MCT
IYS
BNS
A25
A14
A12
A25 A23 A20 A18 A34 A14 A12
Depth (km)

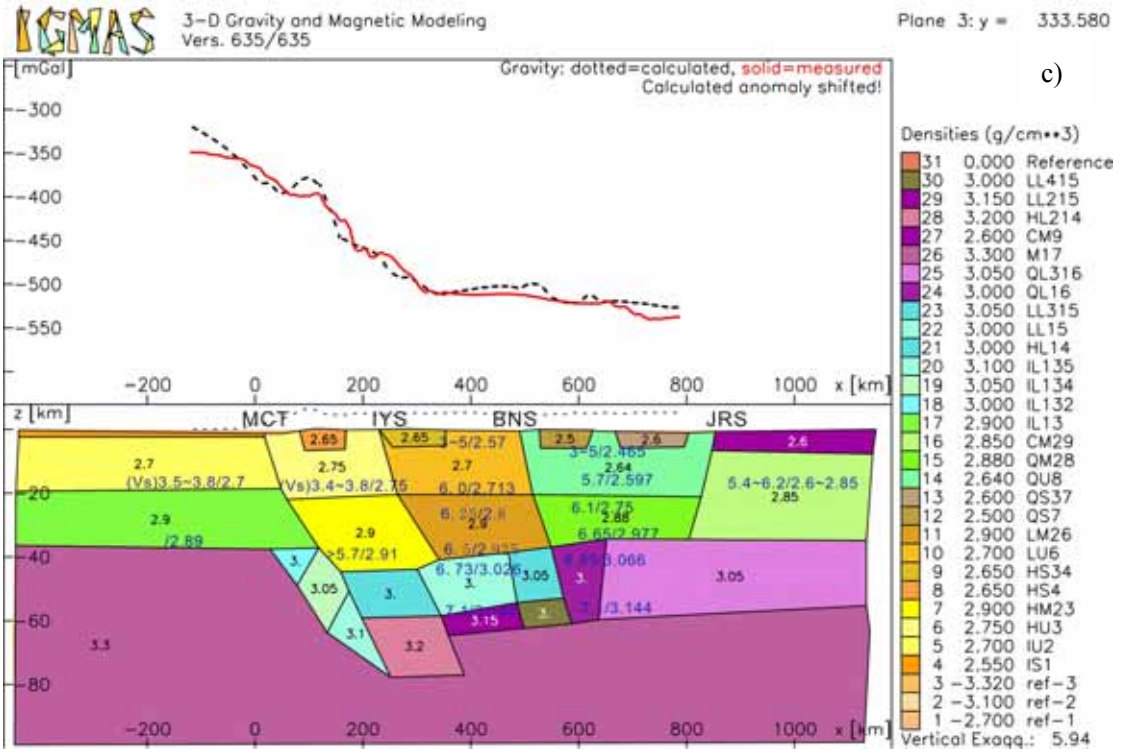
3-D Gravity and Magnetic Modeling
Vers. 635/635
Plane 3: y = 333.580
c)
Gravity: dotted=calculated, solid=measured
Calculated anomaly shifted!
[mGal]
Densities (g/cm**3)
31 0.000 Reference
30 3.000 LL415
29 3.150 LL215
28 3.200 HL214
27 2.600 CM9
26 3.300 M17
25 3.050 QL316
24 3.000 QL16
23 3.050 LL315
22 3.000 LL15
21 3.000 HL14
20 3.100 IL135
19 3.050 IL134
18 3.000 IL132
17 2.900 IL13
16 2.850 CM29
15 2.880 QM28
14 2.640 QU8
13 2.600 QS37
12 2.500 QS7
11 2.900 LM26
10 2.700 LU6
9 2.650 HS34
8 2.650 HS4
7 2.900 HM23
6 2.750 HU3
5 2.700 IU2
4 2.550 IS1
3 -3.320 ref-3
2 -3.100 ref-2
1 -2.700 ref-1
Vertical Exagg.: 5.94
x [km]
z [km]
MCT
IYS
BNS
JRS

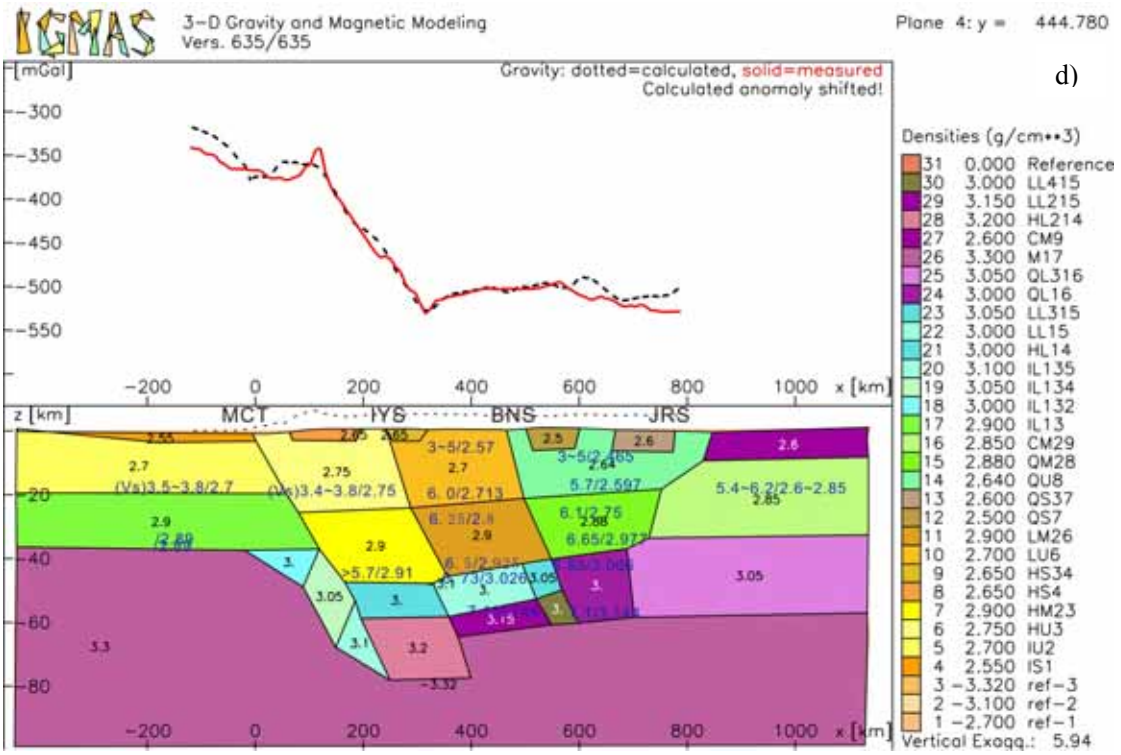
3-D Gravity and Magnetic Modeling
Vers. 635/635
Plane 4: y = 444.780
Gravity: dotted=calculated, solid=measured
Calculated anomaly shifted!
[mGal]
MCT
IYS
BNS
JRS
z [km]
x [km]
Densities (g/cm**3)
31 0.000 Reference
30 3.000 LL415
29 3.150 LL215
28 3.200 HL214
27 2.600 CM9
26 3.300 M17
25 3.050 QL316
24 3.000 QL16
23 3.050 LL315
22 3.000 LL15
21 3.000 HL14
20 3.100 IL135
19 3.050 IL134
18 3.000 IL132
17 2.900 IL13
16 2.850 CM29
15 2.880 QM28
14 2.640 QU8
13 2.600 QS37
12 2.500 QS7
11 2.900 LM26
10 2.700 LU6
9 2.650 HS34
8 2.650 HS4
7 2.900 HM23
6 2.750 HU3
5 2.700 IU2
4 2.550 IS1
3 -3.320 ref-3
2 -3.100 ref-2
1 -2.700 ref-1
Vertical Exagg.: 5.94

d)

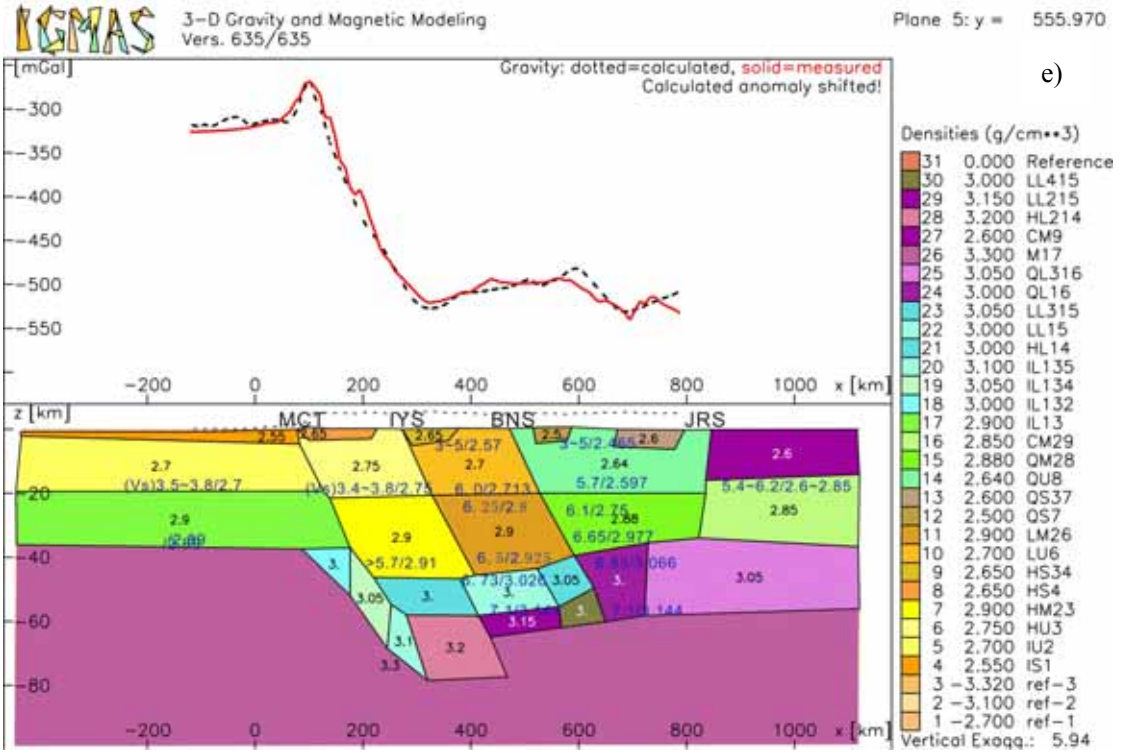
3-D Gravity and Magnetic Modeling
Vers. 635/635
Plane 5: y = 555.970
Gravity: dotted=calculated, solid=measured
Calculated anomaly shifted!
[mGal]
MCT
IYS
BNS
JRS
z [km]
x [km]
Densities (g/cm**3)
31 0.000 Reference
30 3.000 LL415
29 3.150 LL215
28 3.200 HL214
27 2.600 CM9
26 3.300 M17
25 3.050 QL316
24 3.000 QL16
23 3.050 LL315
22 3.000 LL15
21 3.000 HL14
20 3.100 IL135
19 3.050 IL134
18 3.000 IL132
17 2.900 IL13
16 2.850 CM29
15 2.880 QM28
14 2.640 QU8
13 2.600 QS37
12 2.500 QS7
11 2.900 LM26
10 2.700 LU6
9 2.650 HS34
8 2.650 HS4
7 2.900 HM23
6 2.750 HU3
5 2.700 IU2
4 2.550 IS1
3 -3.320 ref-3
2 -3.100 ref-2
1 -2.700 ref-1
Vertical Exagg.: 5.94

e)

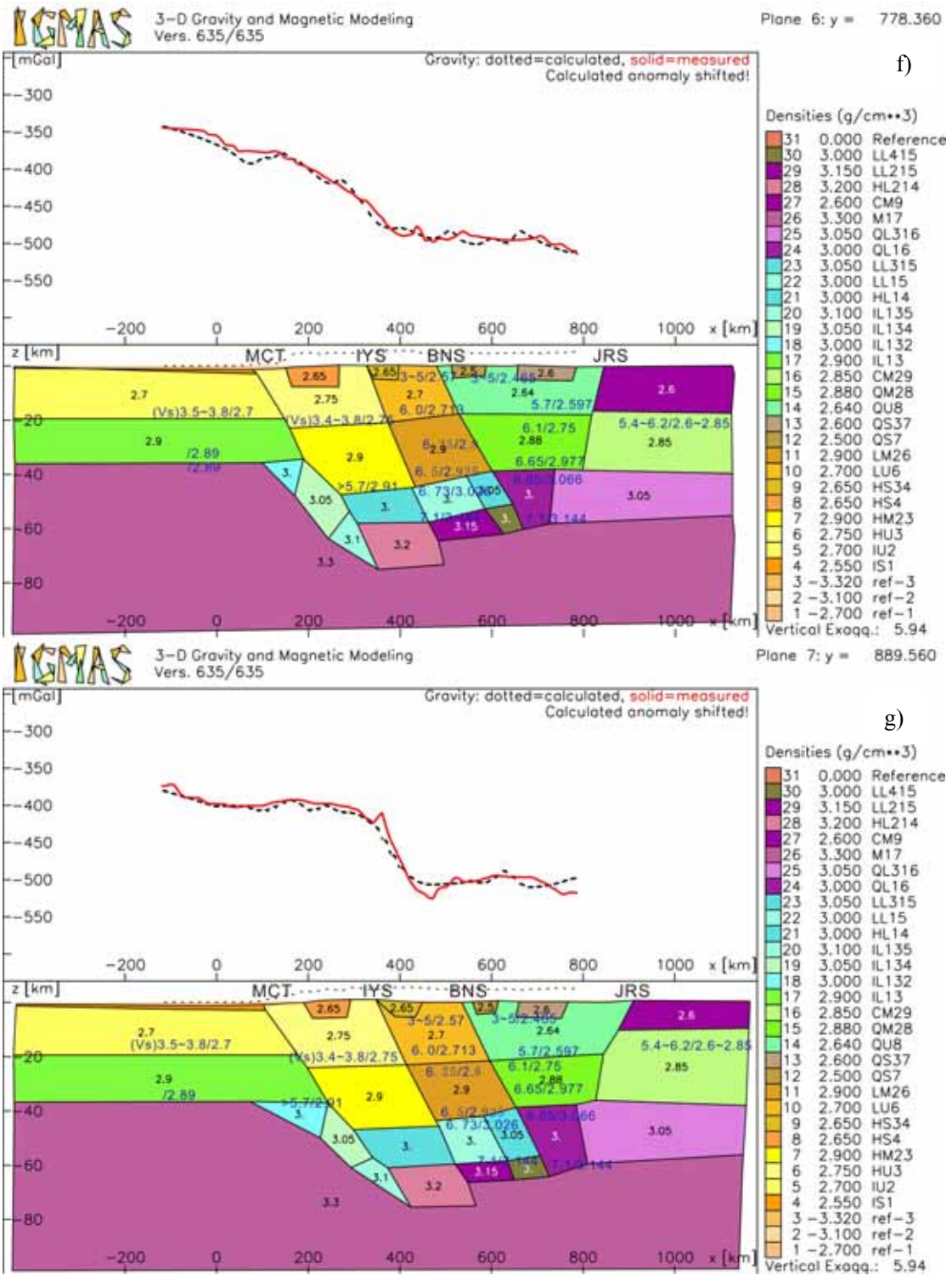

Fig.5.23 a)-g) Cross-sections of the final density model (model III). IS1—Indian foreland basin; IU2—Indian upper crust; HU3—Himalaya upper crust; HM23-- Himalaya middle crust; HS4—Himalaya sediments; HS34--north Himalaya sediments; LU6—Lhasa terrane upper crust; LM26-- Lhasa terrane middle crust; QS7—Qiangtang terrane sediments; QS37—north Qiangtang terrane sediments; QU8—Qiangtang upper crust; QM28—Qiangtang middle crust; CM29 Chaidam middle crust; IL13 , IL132, IL134, IL135— Indian lower crust; HL14-- Himalaya lower crust; LL15-- Lhasa terrane lower crust; LL315 –north Lhasa terrane lower crust; QL16-- Qiangtang lower crust; QL316—Chaidam lower crust; M17—upper mantle; CM9 –Chaidam

upper crust.

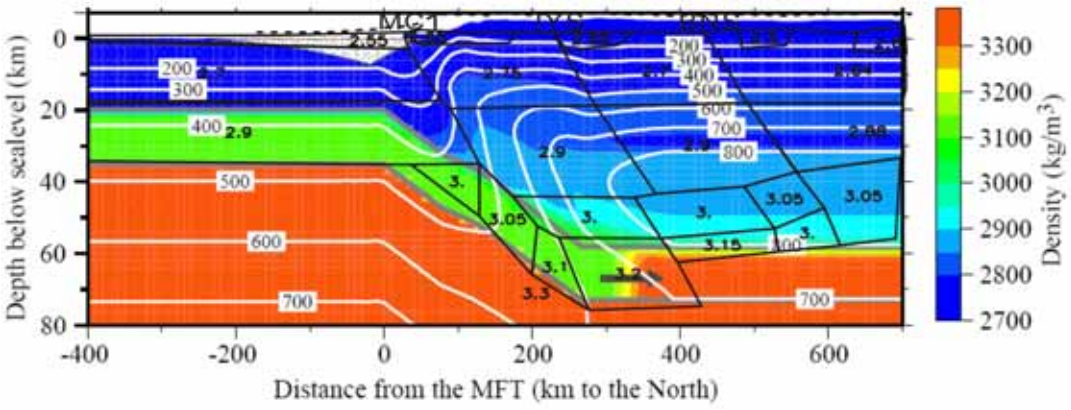

Fig.5.24 Black curves mark the geometry of density structure as described by plane 5 of model III and the black number is the density in g/cm^3. The basemap is after Hetenyi (2007), which shows the best fit density-model based on: 1) the thermal field from thermo-kinematic modelling (white contours and value in ° C, A=2.5μWm^{-3} and q=15mWm^{-2}); 2) petrogenetic grids corresponding to a mafic lower crust with 1 wt.% water content ; 3) eclogitization exists at 300 km distance away. The arrow marks the path of the Indian lower crust and the place where transformation into eclogite takes place. The colored densities of the upper crust and the mantle are based on the petrogenetical grids of Bousquet et al. (1997).

5.7.2 Characteristics of the crustal structure

The east and west profiles have the following characteristics in common:

1) Crustal thickness: in the south of IYS, the crustal thickness is > 70 km in the Himalaya block. Moho interface is at 73-79 km of depth and the average is 76 km of depth in the east. Moho interface is at 70-78 km depth and the average is 73 km depth in the west.

2) The shape of Moho interface: the depth of the Moho interface increases northward. In the south of the study area, Moho interface is discontinuous near the sutures when moving from the eastern to the western profiles.

The east and west profiles have the following different characteristics, mainly located near the sutures:

1) Moho interface in the south of IYS. Moho interface is at 73-79 km depth and the average is 76 km depth in the east. Moho interface is at 70-78 km depth and the average is 73 km depth in the west. This shows depth of Moho interface is deeper in

the east than west. The depth is 78 km in the east (Pumoyong Cuo, the distance is 70 km along Yadong-Namu Cuo profile) and is 70 km in the west (Peigu Cuo). The whole Moho interface shows that crustal thickness of Himalaya block thins from east to west and declines northward.

2) Moho interface beneath sutures. In the east, the Moho interface beneath the sutures presents a complex folded Moho and the Moho declines northward entirely. However, it just shows a simple folded Moho in the west.

Comparing the east and west cross-sections, the dip angle of the Moho interface is larger in the middle of the study area. The former is ~8.5° and the latter is ~16.7° (Fig.5.25). That is to say, the Indian plate collides with the Eurasia plate with a more gentle angle of inclination in east and west, while steeper in the middle part.

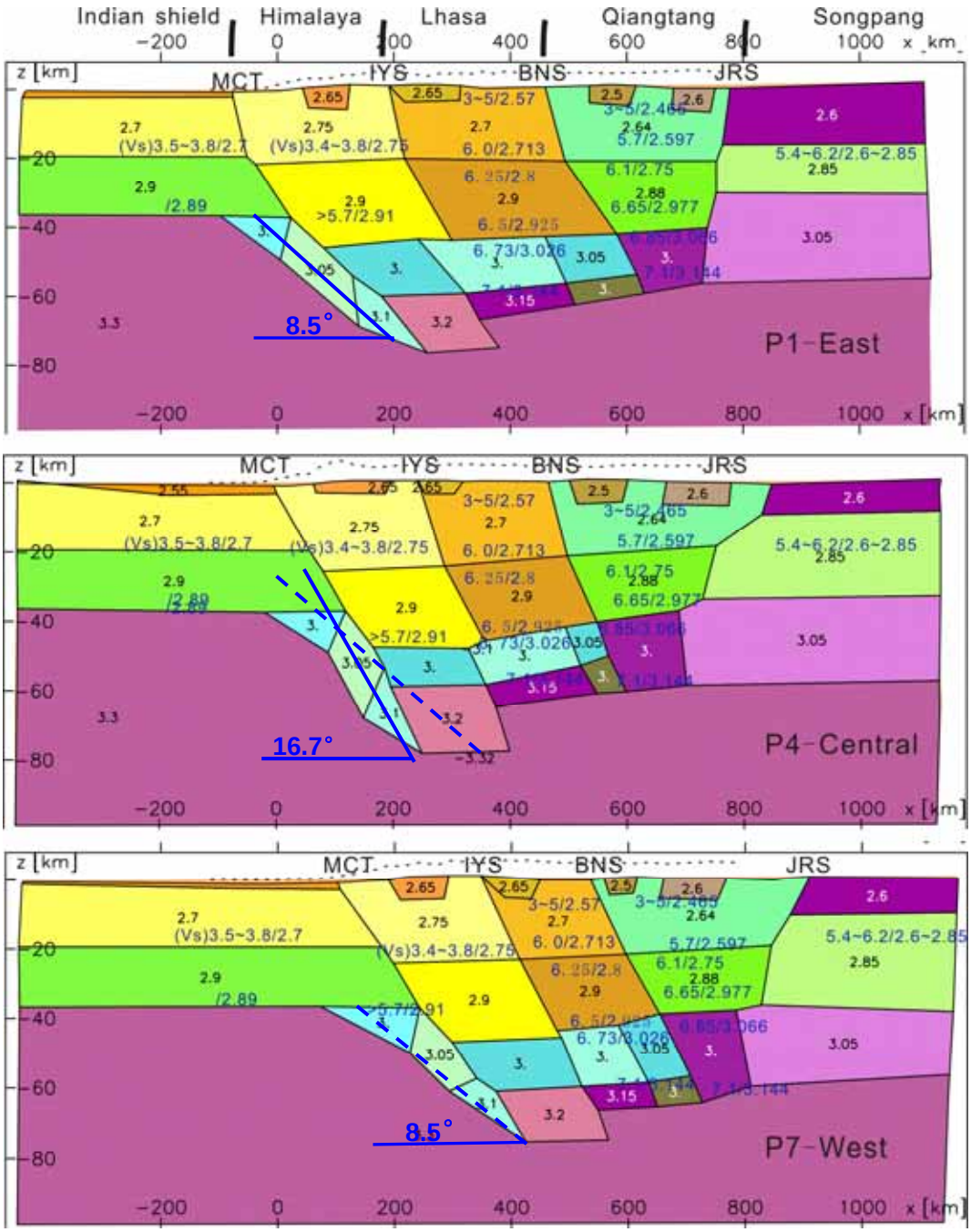

Fig.5.25 Three profiles of model III. P1 stands for the eastern, P4 for the central and P7 for the western profile, respectively

Deep seismic sounding survey in the Kashmir Himalaya (Kaila and Narain, 1976) shows a Moho dipping toward the north-northeast direction, at an average angle of 15-20° . Hauck et al. (1998) and Schulte-Pelkum et al. (2005) proposed that the Moho dips with an angle of few degrees northwards beneath the Sub and Lesser Himalaya and steepens to about 15° beneath the greater Himalaya. Tiwari (2006) suggested MBT and MCT dip with an angle of 22° and 16° to the north,

respectively. Similarly, our gravity modeling shows that the Indian shield underthrusts the plate with a slightly steeper angle beneath the central part than beneath the eastern and western parts in central-south Tibet. Fig.5.26 shows the flexure of the Moho interface of our model.

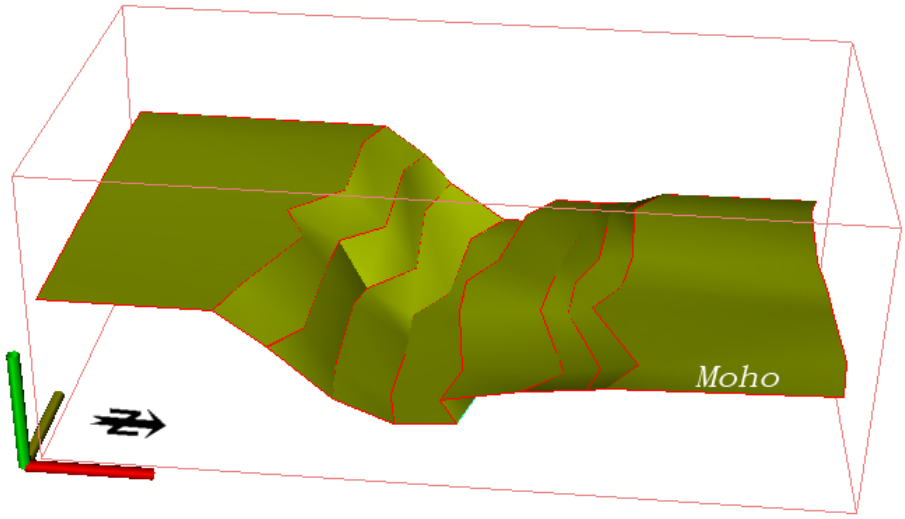

Fig.5.26 Moho interface of model III

5.7.3 Absence or presence of eclogitization in the lower crust?

There are three different opinions about the eclogitization in the lower crust of Tibet. The first one (Le Pichon et al.,1997; Schulte-Pelkum et al., 2005) supports the presence of eclogite beneath the Himalaya. Based on a receiver function study and observed fast P-wave velocities in the lower crustal, Schulte-Pelkum et al. (2005) argue that the lower crust is partially (~30%) eclogitized just South of the IYS, and that the eclogitization process is governed by water availability. This implies that the lower-crust material reaches the eclogite facies via granulite facies conditions, as shown in Le Pichon et al. (1997) for geotherms established after more than ~20 My of relaxation. However, the latter study also shows that the geotherm may follow an amphibolite-eclogite and even a blueschist–eclogite path for shorter relaxation times between ~10 – 20 My and less than ~10 My, respectively.

Based on thermo-kinematic modelling, Henry et al. (1997) proposed that the high

altitude of the Himalayas is related to the absence of eclogites beneath the mountain range. Eclogites would not have been formed due to the fast rates of underthrusting of relatively cold material.

The third study is in support of the ecologitization beneath Lhasa terrane (Tilmann et al., 2003; Cattin et al., 2001; Tiwari et al.,2006). Seismic tomography of the upper mantle in central Tibet revealed a subvertical high velocity zone beneath the northern Lhasa terrane that probably represents the front of detaching Indian mantle lithosphere (Tilmann et al., 2003). Furthermore, based on gravity data combined with numerical modelling, Cattin et al. (2001) showed that eclogitization does not take place under the High Himalayan range as expected from a steady-state local equilibrium assumption, but rather further North beneath the Tibetan Plateau. More recently, Tiwari et al. (2006) showed that gravity and magnetic anomalies across Sikkim can be explained with a model in which the crust beneath Tibet (between 56 and 72 km depth) is eclogitized ~100 km north of the IYS.

Mengel & Kern (1990) proposed that the P-wave velocity of eclogite in lower crust is 6.8-7.6 km/s and density is 3.15-3.6 g/cm^3. According to the modelled density structure, our result shows that the lower crustal densities are smaller than 3.2 g/cm^3 and suggests the absence of eclogite or partial eclogitization due to delamination under the central-south Tibet.

Chapter 6

Seismicity and crustal composition of the Central-South Tibet

6.1 Abstract

The study of the Bouguer anomaly has helped to determine the lateral density variations in the crust of central and southern Tibet. Seven density profiles revealed the east-west variation of the crustal structure in central and southern Tibet. The goals of this study are to ascertain the east-west difference of seismicity in central and southern Tibet and its relation with the crustal structure. Furthermore, this seismicity study is anticipated to help determine the earthquake hazard potential of this area.

The crustal composition of the study area was deduced by comparing the calibrated velocities with the laboratory data set published by Christensen and Mooney (1995). We found that the composition of the upper crust might be one or a mixture of: 1. metagraywacke, andesite and granite-granodiorite beneath the Qiangtang terrane; 2. granite- granodiorite and granite gneiss beneath the Lhasa terrane; 3. biotite gneiss and phyllite beneath the Himalaya. These results indicated that the upper crust is felsic. Meanwhile, the composition of the lower crust has also been constrained by the same data set used for the upper crust and has shown that the composition of the lower crust is made of amphibolite facies. The composition of the lower crust might be one or a mixture of: 1. amphibolite and greenschist facies basalt beneath the Qiangtang terrane; 2. gabbro-norite-troctolite and mafic granulite beneath the Lhasa terrane. Because the composition of the middle crust cannot be well constrained by the above data set (measured velocities are larger than the laboratory velocities), the data set published by Rudnick & Fountain (1995) is used for comparison. It indicates that the composition of the middle crust is granulite facies and might be pelitic gneisses. Granulite facies used to be interpreted as residues of

partial melting, which coincides with the previous study on partial melting in the middle crust. Amphibolite facies are thought to be produced after delamination.

6.2 Seismicity

6.2.1 Fault plane solution

Focal mechanisms of the seismic events since 1976 in the study area (26°N-34°N and 82°E -92°E) are retrieved from the Harvard Centroid Moment Tensor catalog. Most of the events are strike-slip fault or normal fault mechanisms (Fig.6.1), as reported by Molnar and Lyon-Caen (1989). Strike-slip focal mechanisms indicate N-S shortening and E-W extension in the western part of the plateau, swinging through NE-SW shortening to E-W shortening and N-S extension on the eastern margin. Normal fault mechanisms indicate a more consistent pattern of E-W to ESE-WNW extension. One of the most striking aspects of the seismicity is the strong correlation between the mode of faulting and the surface elevation. Reverse faulting is confined to regions on the margins of the plateau, in the Himalaya, the Nan Shan, and the Longmen Shan (the latter two areas are not shown in Fig. 1), with surface elevations less than 3000 m; normal fault mechanisms are confined to the high plateau where elevations exceed 4000 m (Molnar and Lyon-Caen, 1989). The crustal shortening occurs by left and right-lateral strike slip on northeasterly and northwesterly trending planes, respectively, and not by thrust faulting (Molnar, 1992).

6.2.2 Distribution of epicenters

Seismicity since 1910 is obtained from the International Seismological Center (ISC) earthquake catalog. The distribution of epicenters and magnitude of the events near profile 2 (between longitude 89.5°E and 90.5°E), profile 4 (between longitude 86.5°E and 87.5°E) and profile 7 (between longitude 82.5°E and 83.5°E) have been collected (Fig.6.2). The data from the ISC catalog suggest that presently recorded seismicity along these profiles occurs in a series of clusters in space. The seismically active sections are located near Rikaze in the vicinity of profile 2, Dingri of profile 4

and west of Zhongba of profile 7, where a gravity low or a gravity gradient belt is found.

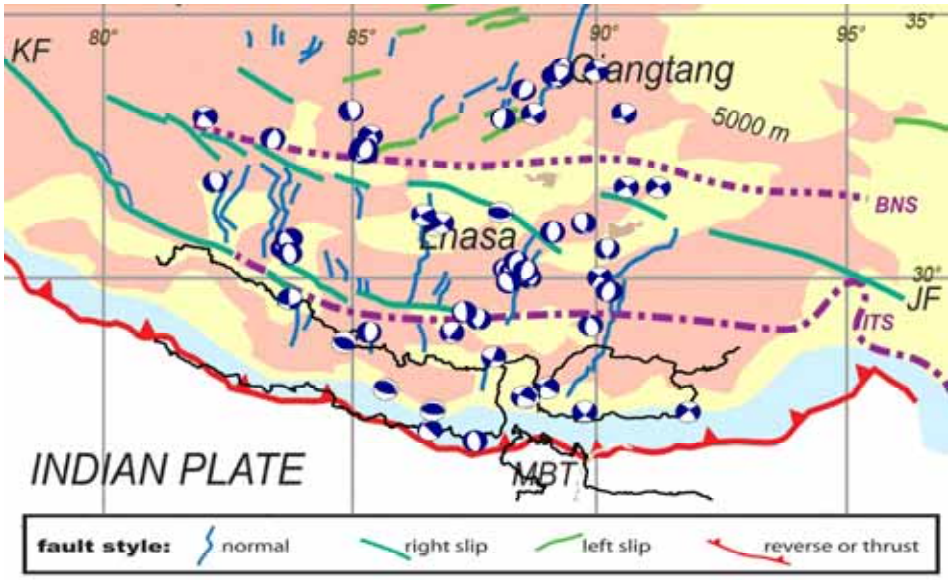

Fig.6.1 Focal mechanisms of events since 1976 are given by Harvard Centroid Moment Tensor catalog. Strike-slip and normal fault mechanisms are confined to the plateau, thrust faulting is confined to regions in the Himalaya.

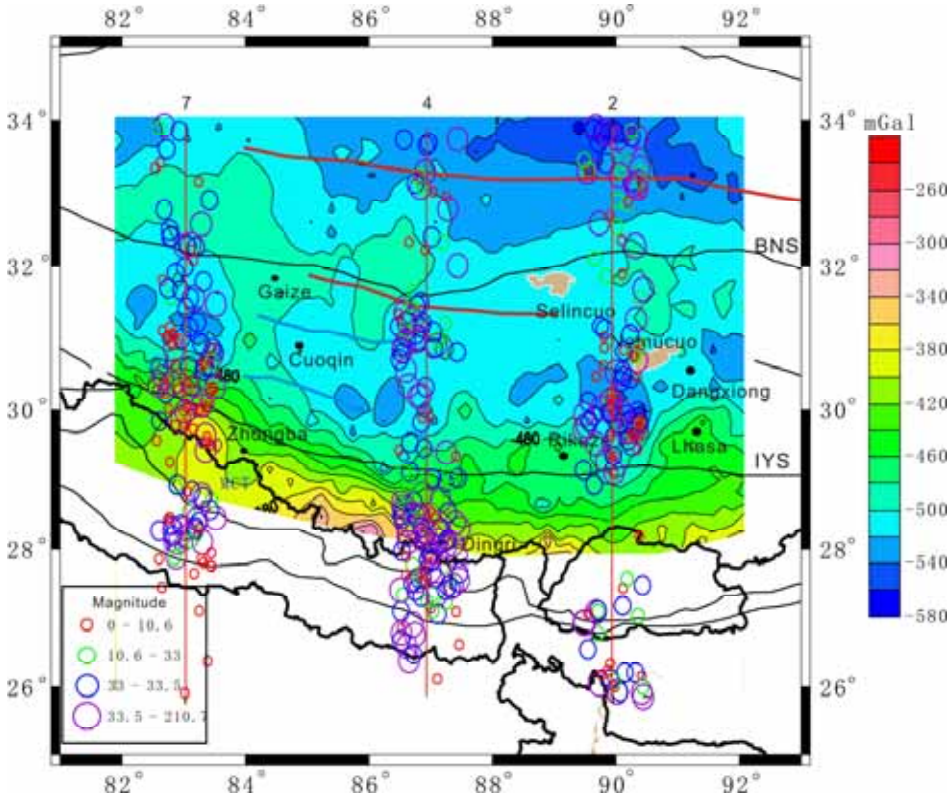

Fig.6.2 Bouguer anomaly and distribution of earthquake hypocenters within a band ~50km on each side of the east, middle and west profiles (red line). Open circles are events and are scaled by magnitude. Red curves are strike-slip faults. Blue curves are thrust faults. Filled black circles mark geographical location of cities.

6.2.3 Statistical evaluation of seismicity

The relation between the event magnitude and the released energy can be calculated starting from the hypothesis that the elastic energy radiated by an earthquake propagates uniformly in all directions (Panza, 2006). To calculate the seismic energy of the single event, the most used relation is that proposed by Gutenberg and Ricthter (1956 a,b):

$$\text{Log}(\ E_i\ (\text{erg})) = 11.4 + 1.5\text{Ms} \tag{6.1}$$

where E_i is the energy associated to the i-th event. Where necessary, magnitudes Mb and Ml have been transformed into Ms using the relations of Peishan and Haitong (1989).

To analyze the dependence of seismicity on position, the seismicity along the east profile (profile2) is discussed as an example. The seismic energy versus spatial distance along the profile has been calculated, grouping the events with epicenters located in intervals of 25km, 40km and 50km, respectively:

$$E_n(erg) = \sum_{i=1}^{m} E_i(erg) \tag{6.2}$$

where m is the number of the events of n-th interval and it has been represented as $\log(E_n/A_{min})$ where A_{min} (erg) is the minimum E_n, computed in one of the considered depth intervals. In this case, the minimum energy is 2.5×10^{20} erg.

The histograms of cumulative count (Fig.6.3) and seismic energy distribution (Fig.6.4) have similar trends along the profile for the three step-sizes (25km, 40km and 50km). A large number of earthquakes occurred in the domains of 200-400 km and 600-800 km along the profile and reach maximum values in the locations ~300 km and ~720 km (grouped by 25 km or 40 km) along the east profile. Seismic energy is low near position 100 km.

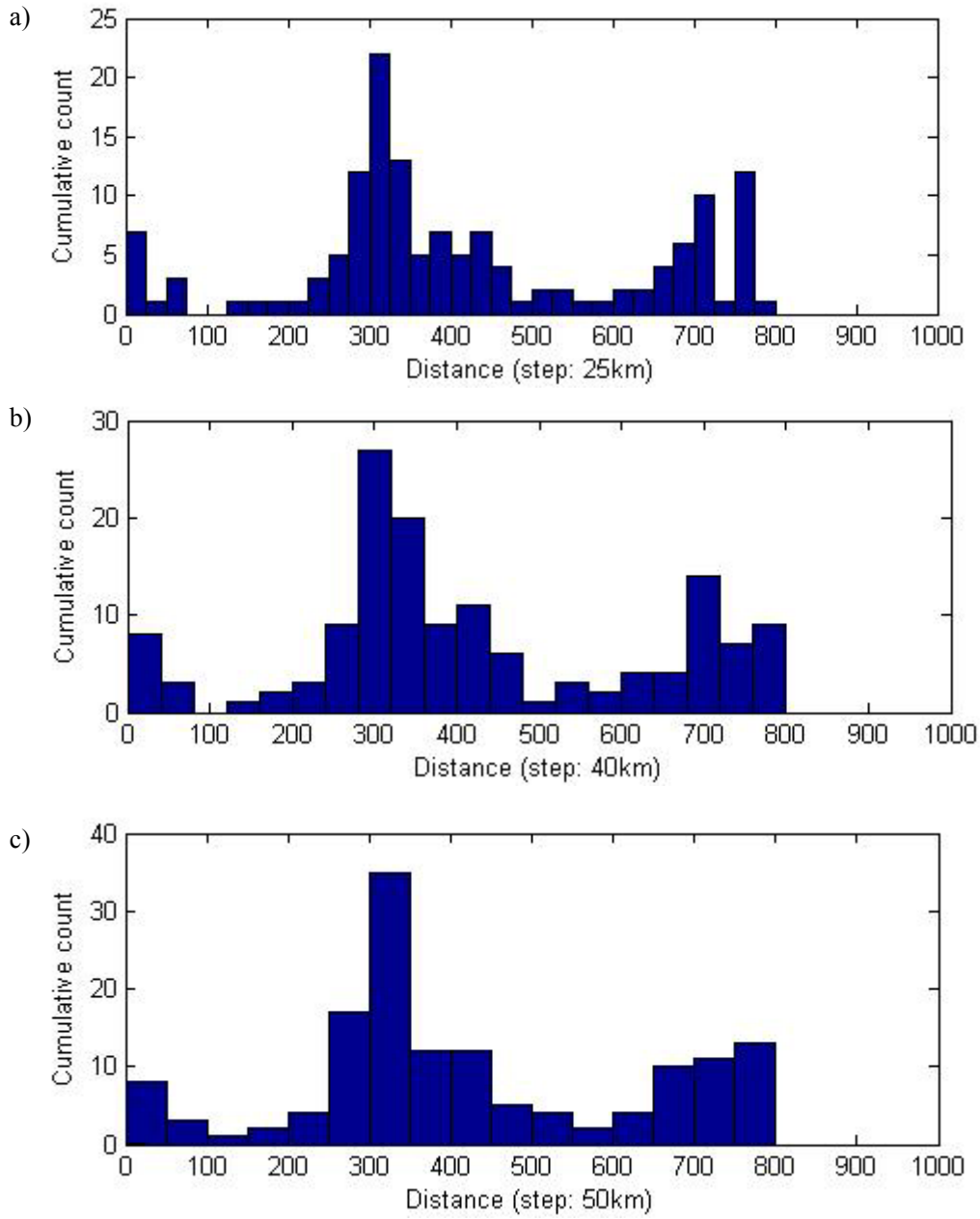

Fig.6.3 The cumulative count of seismic events along the profile, a) grouped by 25km, b) grouped by 40 km, c) grouped by 50km intervals. The distributions are similar when the interval is > 25 km.

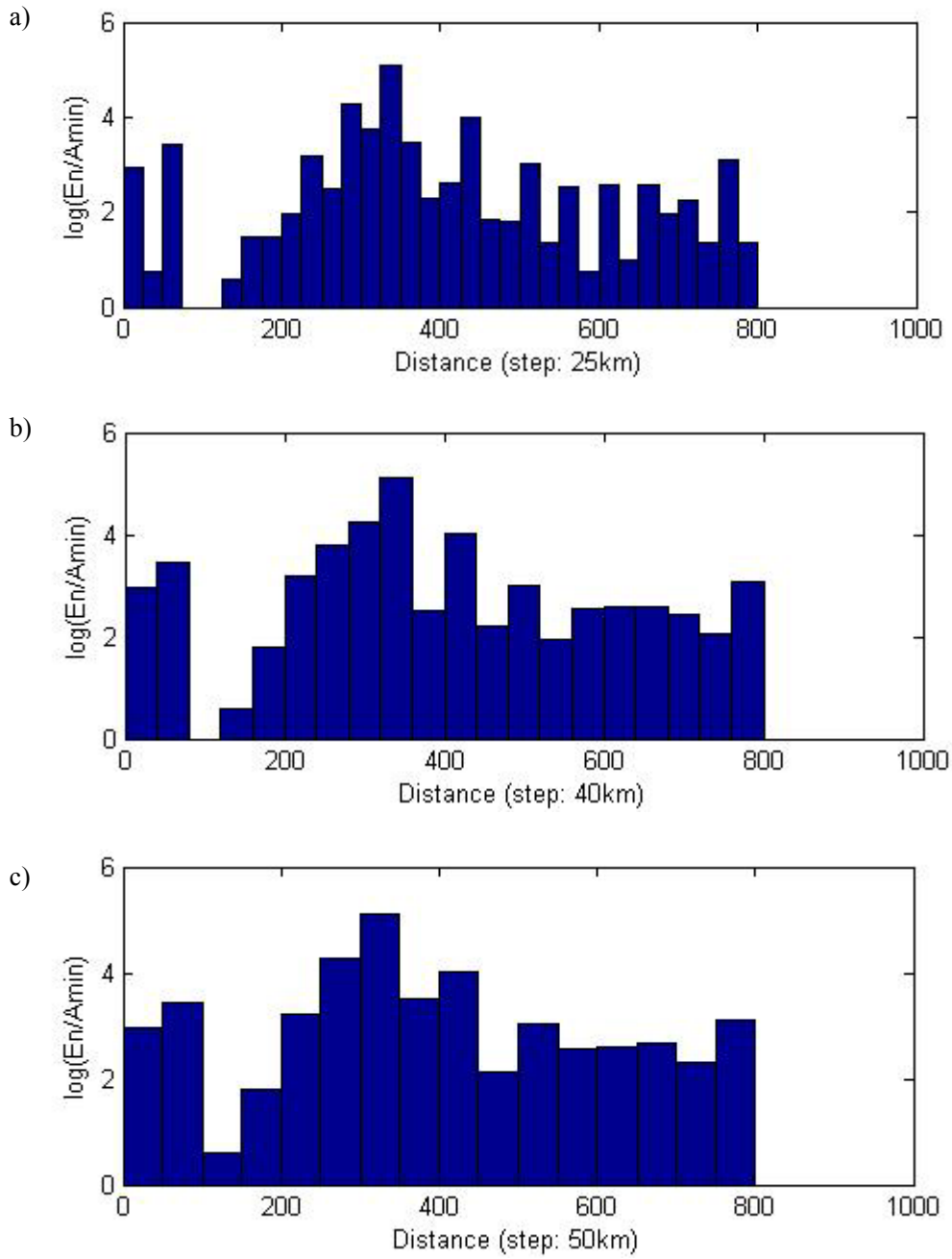

Fig.6.4 Same as Fig.6.3 but for seismic energy distribution, represented as $\log(E_n/A_{min})$ vs. spatial distance

6.2.4 Correlation between crustal structure and seismicity

The ISC catalog reports the majority of the events having focal depths shallower than 33 km. All the seismicity occurs within the upper and middle crust beneath the Lhasa terrane and Qiangtang terrane. However, because of the absence of nearby stations, depths of earthquakes are poorly constrained for the public catalog. Almost all the studies of earthquake relocation support the fact that ninety-nine percent of the

local earthquakes have focal depth shallower than 25km. The shallow earthquake focal depths are consistent with high temperatures and proposed ductile or aseismic behavior in the lower crust of the eastern and western parts of central Tibet.

To get more detailed knowledge of seismicity, it is better to group the data by intervals < 25km. The seismicity grouped at 10km intervals along east, middle and west density profiles are shown in Fig. 5. In the east profile, seismic energy concentrates in the Tethys Himalya, southern Lhasa terrane and central Qiangtang terrane; in the central portion, seismic energy concentrates in the northern Indian shield and northern Lhasa terrane; in the west, the energy focuses in the northern Indian shield and southern Tibet.

Although Tibet is sliced by several near east-west trending sutures, a large number of north-south tectonics should also be noticed as another main geological characteristic. The elevations are higher in eastern and western Tibet than in central Tibet. The topography undulates slightly in central Tibet, while with greater amplitude in the east and west. The north-south extension of Tibet is 400-500km, one third of the width as in the center.

At present, there are hardly any geological surveys on the north-south tectonics leading to the east-west variation of surface geology, because the geoscientists have been paying more attention to the east-west trending tectonics. However, considering the potential field, we find that Bouguer anomalies decrease from west to east and change abruptly near longitude 83.5° E, 86° E and 90.5° E (Fig. 2) in support of a east-west variation in Tibet.

In addition, east-west trending variation of crustal structure, inferred from the gravity field and from wide-angle reflection/refraction seismic surveys and seismic tomography, can be the cause of the east-west variation of seismicity. The study of body wave tomography (Zhou, 1996) reveals higher velocity in the upper crust of central Tibet and lower velocity in east and west. Reversely, lower velocity is found in the lower crust and upper mantle of central Tibet and higher velocity in the east and west Tibet. The crustal structure modeled by gravity data also presents east-west trending differences in Tibet (Fig.6.5). The Indian shield underthrusts with different

angles beneath Tibet and flexes weaker in east and west with respect to central Tibet.

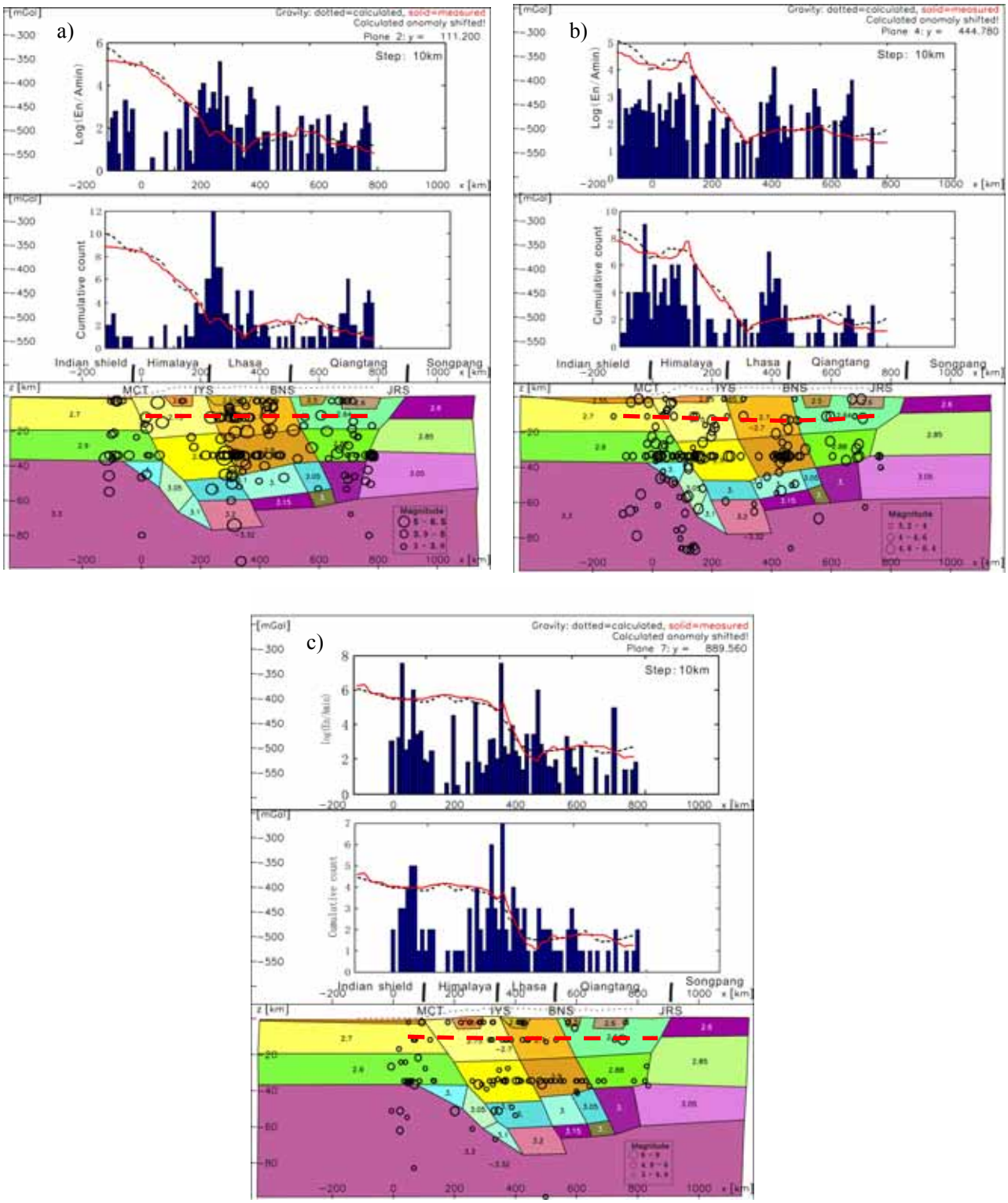

Fig.6.5 Combined analysis of gravity and seismicity. In the east profile (plane 2), strong seismic energies concentrate in the Tethys Himalya, southern Lhasa terrane and central Qiangtang terrane. Strong seismic energies assemble in the northern Indian shield and northern Lhasa terrane in the central portion (plane 4). In the west (plane 7), the energies focus in the northern Indian shield and southern Tibet.

6.3 Composition of the crust in central-south Tibet

6.3.1 Dependence of the seismic wave velocity on P-T conditions

Because pressure and temperature can strongly influence the seismic velocities of crustal rocks, it was necessary to correct the crustal refraction data to a common pressure and temperature for purposes of comparison (Rudnick and Fountain, 1995). In order to make valid comparisons of the Vp and density values with similar quantities from laboratory measurements, the present-day pressure and temperature conditions within the crust must be considered.

Considering numerical laboratory experiments, Kern (1985, 1988) proposed the integral formula for the relationship between seismic wave (P-wave) velocity, temperature and pressure as follows:

$$V(z) = V(0) + \int_0^z [(\frac{\partial V}{\partial P})_T \frac{dP}{dz} + (\frac{\partial V}{\partial T})_P \frac{dT}{dz}]dz . \quad (6.3)$$

Then, Eq. (6.3) can be simplified as

$$V_z = V_0 + dV/dP \cdot \Delta P + dV/dT \cdot \Delta T , \quad (6.4)$$

where dV/dP, dV/dT are the temperature and pressure coefficient, respectively. Theoretically, V_0 is the velocity at a certain temperature and pressure.

A typical pressure derivative for Vp is used here, determined at confining pressures above 400 MPa (~2.0×10^{-4} km/(s • MPa)) and a typical temperature derivative (~-4.0×10^{-4}km/s •° C^{-1}) for crustal rocks (Christensen and Mooney, 1995; Rudnick and Fountain, 1995). Therefore, Eq. (6.4) can be rewritten as

$$V_0 = V_z - [2(P_z - 600) - 4(T_z - 20)]\cdot 10^{-4} . \quad (6.5)$$

6.3.2 Calibrated P-wave velocity and crustal composition

6.3.2.1 Velocity calibration

Firstly, in order to calibrate all the P-wave velocities to a standard pressure of 600 MPa and room temperature, the crustal temperatures are estimated from the thermal modeling result (Hetényi et al., 2007; Jiménez-Munt et al., 2008) and pressure of each

layer is determined by its depth and the density obtained from gravity modeling. By recalculating the P-wave velocities for each layer using the derivatives given above, the velocities can then be compared with laboratory measurements of ultrasonic velocities, which are generally performed at room temperature. Table 6.1 lists the published velocities for the units used in the compilation as well as the velocities calibrated to room temperature and 600 MPa confining pressure.

The results from modeling the thermal evolution (Hetényi et al., 2007; Jiménez-Munt et al., 2008) show that the imbricated thrust yields a thermal structure in general agreement with the observations: high heat flow in south-central Tibet, high temperature in the middle crust of the Himalaya region, low-velocity and high-conductivity zones, presence of leucogranites and inverted metamorphism, and low temperatures in the upper mantle beneath the Himalaya region corresponding to high seismic velocities. The studied area has a relatively hot middle crust and cold mantle, which result from shear heating and advective cooling both due to active thrusting.

Secondly, the pressure in the deep crust can be calculated easily by the formula $P=\rho gz$, where ρ has been obtained by gravity modeling. It is an advantage to replace the average crustal density by the density values which have been estmated; g is gravity acceleration and equal to 9.81 m/s^2, z stands for depth.

By recalculating the P-wave velocities for each layer using the derivatives given above, the P-wave velocities can then be compared with laboratory measurements of ultrasonic velocities, which are generally performed at room temperature. Table 6.1 lists the published velocities for the units used in the compilation, as well as the P-wave velocities (Vp) (Table 6.1). The latter have been calibrated (Vp') to a standard pressure of 600 MPa and room temperature using the pressure derived from the density model and published temperature data using Eq. (6.5).

6.3.2.2 Composition of the upper crust

Fig.6.6 shows the calculated densities and velocities for the different bodies of the study area and laboratory data set. Every line corresponds to one of the bodies of our

density model (see e.g. Fig. 5.20). As shown in Fig. 6.7(a), Metagraywacke (MGW), Andesite (AND) and Granite-granodiorite (GRA) are the main composition of QU8. Although the curves of Granite-granodiorite (GRA), Granite-gneiss (GGN) and Quartzite (QTZ) are around the lines of LU6 and IU2, the velocities of Quartzite (QTZ) are lower than the calibrated velocities of LU6 and IU2. Therefore, we think LU6 and IU2 are composed of Granite-granodiorite (GRA), Granite-gneiss (GGN). Gravity anomaly is greater in Himalaya than in Tibet, so the material of Himalaya is denser than that of Tibet. According to Fig.6.7 (a), the composition of HU6 is denser than LU6 and QU8 beneath the Tibet, and possibly is made of Biolite (Tonalite) Gneiss (BGN) and Pyroxenite (PYX). Paragranulite (PGR) and Felsic Granulite (FGR) are excluded for their higher density than HU6.

6.3.2.3 Composition of the middle crust

Due to the fact that the calibrated middle crustal velocities are higher than those of the rock types, whose densities are around the range of densities of QM28, HM23 and LM26 (see Fig.6.7(b)), we cannot determine the composition of these middle crustal units. It demands a more valid technique to determine the composition of middle crust.

We used the data set of Rudnick & Fountain (1995) for further comparison. Figure 6.8 shows the calculated densities and velocities for the different bodies of the study area and laboratory data set of Rudnick & Fountain (1995). As shown in a zoom figure (Fig.6.9) of Fig.6.8, it indicates the middle crust is intermediate granulite facies and might be pelitic gneisses.

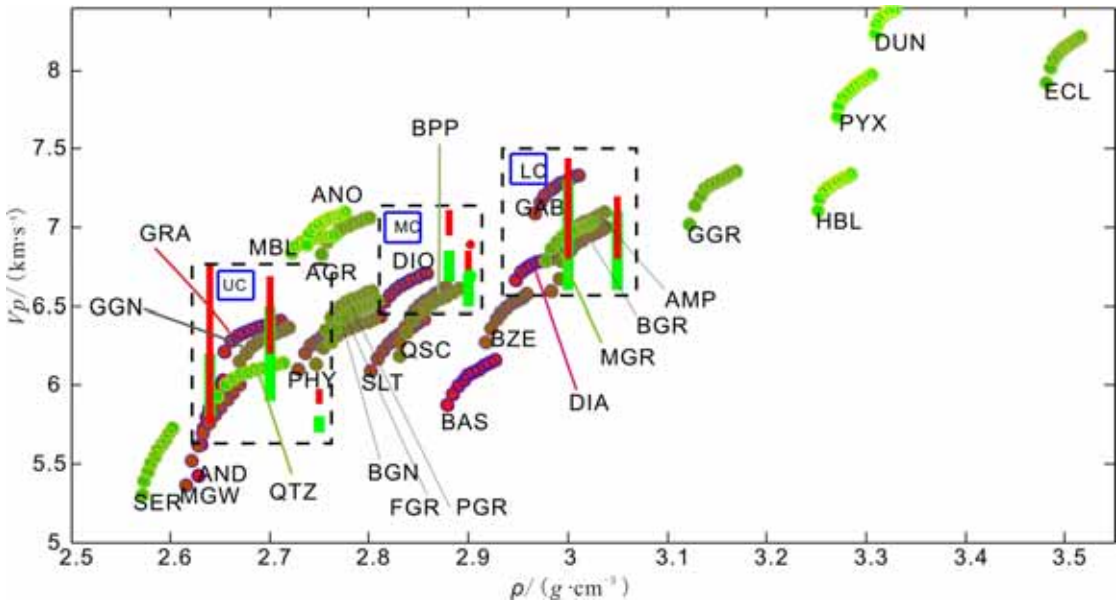

Fig.6.6 Thick green lines show density of gravity modelling and the range of published P-wave velocities and thick red lines show the calibrated values of P-wave velocities at room temperature and 600 MPa pressure. Filled points present the densities and velocities of 29 rock types at room temperature and 600 MPa pressure. Dashed rectangles show the cluster of different crustal layers, UC is upper crust, MC is middle crust and LC is lower crust, respectively.

* Andesite (AND), Basalt (BAS), Diabase (DIA), Granite-granodiorite (GRA), Diorite (DIO), Gabbro-norite-troctolite (GAB), Metagraywacke (MGW), Slate (SLT), Phyllite (PHY), Prehnite-Pumpellyite Facies Basalt (BPP), Greenschist Facies Basalt (BGR), Granite-gneiss (GGN), Biolite (Tonalite) Gneiss (BGN), Mica Quartz Schist (QSC), Amphibolite (AMP), Felsic Granulite (FGR), Paragranulite (PGR), Anorthositic Granulite (AGR), Mafic Granulite (MGR), Serpentinite (SER), Quartzite (QTZ), Zeolite Facies Basalt (BZE), Mafic Garnet Granulite (GGR), Mafic-eclogite (ECL), Calcite Marble (MBL), Anorthosite (ANO), Hornblendite (HBL), Pyroxenite (PYX), Dunite (DUN)

6.3.2.4 Composition of the lower crust

As seen in Fig.6.7(c), the lower crustal rocks of IL13, HL14, LL15 and QL16 are possibly a mixture of Gabbro-norite-troctolite (GAB), Mafic Granulite (MGR) and Diabase (DIA). Amphibolite (AMP) and Greenschist Facies Basalt (BGR) are excluded also for their higher densities. But AMP and BGR might be the composition of IL134, LL215 and LL315.

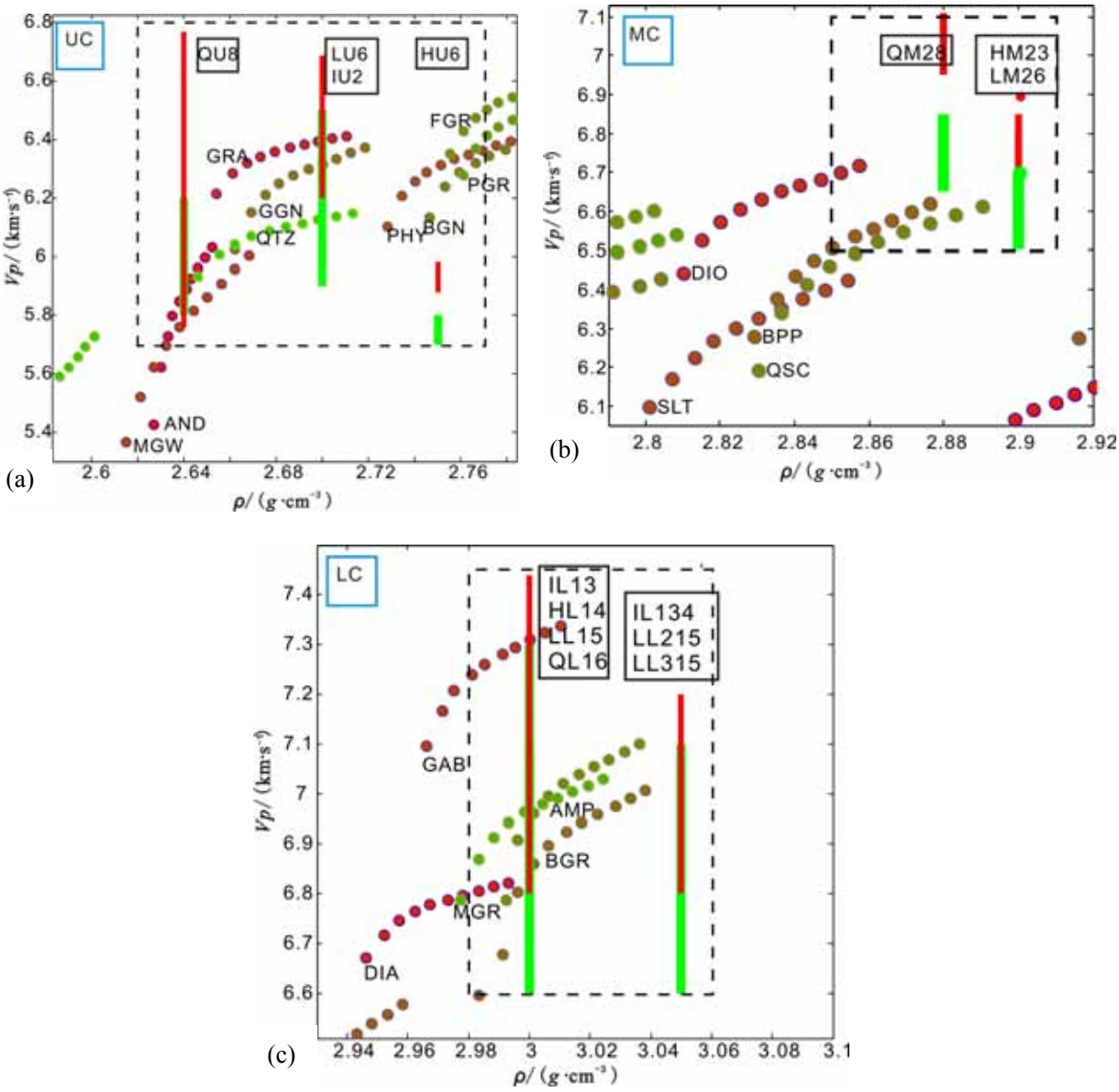

Figure.6.7 Zoom on Fig6.6 for the part of (a) upper crust (UC), (b) middle crust (MC) and (c) lower crust (LC), respectively.

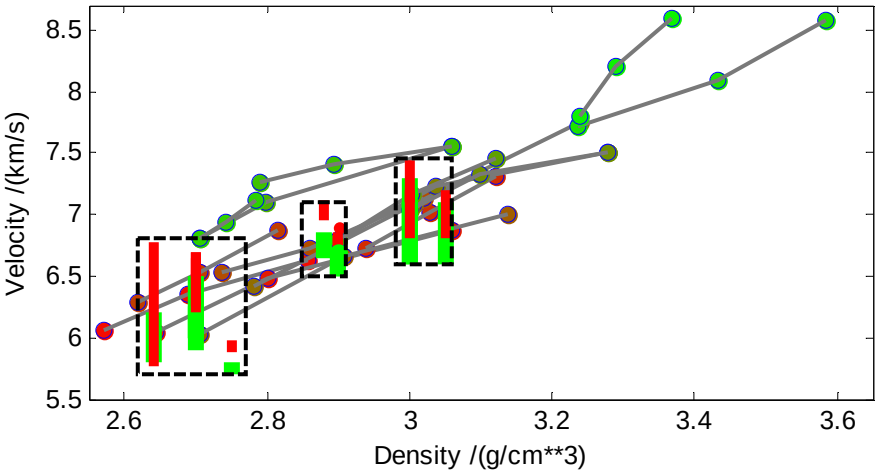

Fig.6.8 Same as Fig.6.6, thick green lines show density of gravity modelling and the range of published P-wave velocities and thick red lines show the calibrated values of P-wave velocities at room temperature and 600 MPa pressure. Filled points present the densities and velocities at room temperature and 600 MPa pressure from the data set of Rudnick & Fountain (1995).

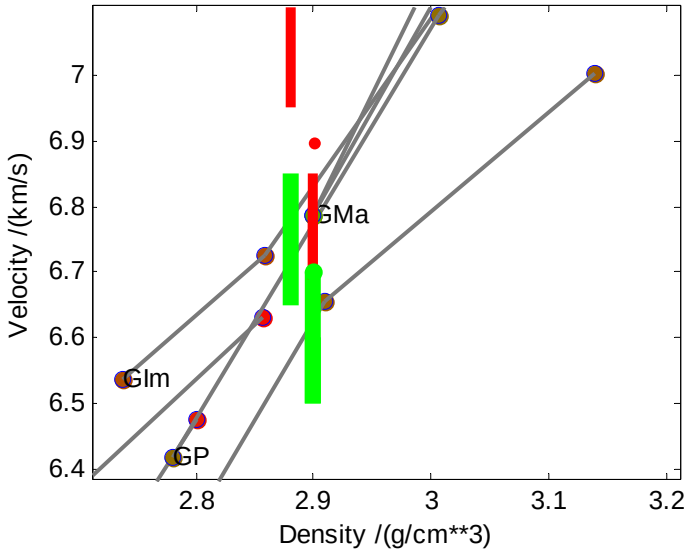

Fig.6.9 Zoom in Fig.6.8 for the part of MC. (GMa-Mafic Granulite Facies, GIm-Intermediate Granulite Facies, GP-Pelitic gneisses)

Table 6.1 Physical parameters of the different bodies used in the density modelling. We give the name of the body, the density, the published in situ velocity, the temperature, and the calibrated velocity

Unit	ρ(g/cm^3)	Vp(km/s)	Temp. (° C)	Vp'(km/s)
IS1	2.55	**3.59-4.6**	50-150[a]	3.72-4.75
IU2	2.7	**5.9-6.5**	150-250[a]	6.04-6.64
HU3	2.75	>5.7 (Hauck et al., 1998)	<400	>5.88
HM23	2.9	**6.5**	<600[a, c]	6.69
HS4	2.65	**4.2-5.3**	**50-180**	4.32-5.45
HS34	2.65	**4.2-5.3**	**50-180**	4.32-5.45
LU6	2.7	6-6.5 (Meissner et al., 2004; Zhao et al., 2001) 6-6.25 (Haines, 2003)	<600[c]	6.2-6.69
LM26	2.9	6.5-6.73 (Haines, 2003) 6.5-6.7 (Meissner et al., 2004)	800[c]	6.69-6.85
QS7	2.5	4-5 (Haines, 2003)	<200[b]	4.13-5.15
QS37	2.6	4-5 (Haines, 2003)	<200[b]	4.13-5.15
QU8	2.64	~5.8–6.2 (Meissner et al., 2004) ~5.6–6.5 (Zhao et al., 2001) 5.7-6.1 (Haines, 2003)	200-600[a, c]	5.76-6.77
QM28	2.88	6.65-6.85 (Haines, 2003)	800[c]	6.95-7.11
IL13/132 /134/135	2.9/3.0 3.05/ 3.1	**6.7**	350-450[a, c]	6.9
HL14/214	3.0, 3.2	**6.9-7.3**	700-800[b]	6.97-7.44
LL15/215	3.0, 3.15	6.6–7.1 (Meissner et al., 2004) 7–7.3 (Zhang and Klemperer, 2005) 6.5–7.3 (Zhao et al., 2001)	1000-1100[b] 700-800[c]	6.8-7.2
LL315	3.05	6.6–7.1 (Meissner et al., 2004) 7–7.3 (Zhang and Klemperer, 2005) 6.5–7.3 (Zhao et al., 2001)	1000-1100[b] 700-800[c]	6.8-7.2
QL16	3.0	6.6–7.1 (Meissner et al., 2004) 7–7.3 (Zhang and Klemperer, 2005) 6.5–7.3 (Zhao et al., 2001) 7.1 (Haines, 2003)	1000-1100[b] 700-800[c]	6.8-7.2

Descriptions of each unit: IS1—Indian foreland basin; IU2—Indian upper crust; HU3—Himalaya upper crust; HM23-- Himalaya middle crust; HS4—Himalaya sediments; HS34--north Himalaya sediments; LU6—Lhasa terrane upper crust; LM26-- Lhasa terrane middle crust; QS7—Qiangtang terrane sediments; QS37—north Qiangtang terrane sediments; QU8—Qiangtang upper crust; QM28—Qiangtang middle crust; CM29 Chaidam middle crust; IL13 , IL132, IL134, IL135—Indian lower crust; HL14-- Himalaya lower crust; LL15-- Lhasa terrane lower crust; LL315 –north Lhasa terrane lower crust; QL16-- Qiangtang lower crust; QL316—Chaidam lower crust; M17—upper mantle; CM9 –Chaidam upper crust. Black body texts for Vp are deduced from Vs from Mitra et al., 2005. The superscript a-Brewer et al., 2006; b-Jiménez_Munt et al., 2008 ; [c]-Hetenyi et al., 2007

Chapter 7

Conclusions

Using gravity anomaly observations and surface waves data, a 3D density model of central-south Tibet is proposed and the characteristics of the seismic anisotropy gradient are discussed in this study. The main results are summarized as follows:

1. QL waves have been identified from the seismograms of selected paths recorded by the Tibetan station CAD, and are utilized to determine the variation of the uppermost mantle anisotropy of the Tibetan plateau. The location of the azimuthal anisotropy gradient is estimated from the group velocities of Rayleigh wave, Love wave and QL wave. We find that a predominant south-north lateral variation of azimuthal anisotropy is located in correspondence of the Tanggula mountain, and a predominant east-west lateral variation of azimuthal anisotropy is found to the north of the Gandese mountain (near 85° E longitude and 30° N latitude) and near the Jinsha river fault (near 85° E longitude and 35° N latitude).

2. The spatial resolution of the QL analysis is such that the identified anisotropies can only marginally be used in the setup of the 3D density model. Rather, the 3D density model was constrained by reviewing all available active seismic and passive seismological results on the velocity structure of crust and lower lithosphere in Tibet. The velocities were converted to density applying experimental and theoretical results regarding the mutual relation between the two quantities.

3. We have produced a full high resolution seismological compatible 3D density model of south central Tibet. Of general interest is the observation, that our constrained density model has a value smaller than 3.2 g/cm^3 in the lower crust of Tibet. This fact suggests absence of eclogite or partial eclogitization due to delamination under the central-south Tibet.

4. The final density model shows that the dip angle of the Moho interface is near to 8.5° in the eastern and western part of south central Tibet, which is smaller than the one found in the central part (~16.7°). We may infer that the Indian lithosphere underthrusts the Tibetan lithosphere gently in the eastern and western part of the central-south Tibet, while steeper in the central part, which indicates increased flexural rigidity of the lithosphere in the eastern and western parts of the study area.

5. Our work allows to give indications regarding the composition of the upper crust, which might be one or a mixture of: 1. metagraywacke, andesite and granite-granodiorite beneath the Qiangtang terrane; 2. granite- granodiorite and granite gneiss beneath the Lhasa terrane; 3. biotite gneiss and phyllite beneath the Himalaya. These results indicated that the upper crust is felsic. The composition of the middle crust is granulite facies and might be pelitic gneisses. Granulite facies used to be interpreted as residues of partial melting, which coincides with the previous study on partial melting of the middle crust. Amphibolite facies are thought to be produced after delamination. The composition of lower crust might be one or a mixture of: 1. amphibolite and greenschist facies basalt beneath the Qiangtang terrane; 2. gabbro-norite-troctolite and mafic granulite beneath the Lhasa terrane.

References

Allègre, C. J., et al., Structure and evolution of the Himalaya-Tibet orogenic belt. Nature, 1984. 307,17-22

Argand, E., La tectonique de l'Asie, in 13th Internationa Geological Congress, B russels, 1924. pp. 170-372

Barazangi M., Ni J., Velocities and propagation characteristics of Pn and Sn beneath the Himalayan Arc and Tibetan plateau: possible evidence for underthrusting of Indian continental lithosphere beneath Tibet. Geology, 1982. 10(4): p. 179-185.

Berteussen K.-A., Levshin A.L., and L.I. Ratnikova, 1983. Regional studies on the crust in Eurasia with surface waves recorded by the NORSAR group. In Mathematical Models of the structure of the Earth and the Earthquake Prediction, Comput. Seismology, 14, Allerton Press, NY, 106-116.

Bostock M.G. Surface wave scattering from 3-D obstacles. Geophys. J. Int., 1991. 104, 351~370

Bostock M.G., Kennett B.L.N. Multiple scattering of surface wave from discrete obstacles. Geophys. J. Int., 1992. 108, 52~70

Bousquet R, G.B., Henry P, et al, Kinematic, thermal and petrological model of the Central Alps: lepontine metamorphism in the upper crust and eclogitisation of the lower crust. Tectonophysics, 1997. 273: p. 105-127.

Bousquet, R., Goffé, B., Henry, P., Le Pichon, X., Chopin, C.. Kinematic, thermal and petrological model of the Central Alps: lepontine metamorphism in the upper crust and eclogitisation of the lower crust. Tectonophysics, 1997. 273, 105–127

Braitenberg C., M. Zadro., J. Fang et al., Gravity inversion in Qinghai-Tibet Plateau. Phys. Chem. Earth, 2000. 25(4): p. 381-386.

Braitenberg C., Y. Wang, J. Fang, H. T. Hsu, Spatial variations of flexure parameters over the Tibet-Qinghai plateau. Earth and Planetary Science Letters, 2003. 205: p. 211-224.

Breunig, M., A. B. Cremers, H. J. Götze et al., Geologic mapping based on 3D models using an interoperable GIS. GIS J. Spatial Inf. Decis. Making, 2000. 13: p. 12-18.

Brocher, T.M. Empirical relations between elastic wavespeeds and density in the Earth's crust, Bull. seism. Soc. Am., 2005. 95(6), 2081–2092

Bungum H and J Capon. Coda pattern and multipath propagation of Rayleigh waves at NORSAR. Phys. Earth and Planet. Inter., 1974, 9: 11-127

Burtman, V. S., and P. Molnar. Geological and geophysical evidence for deep subduction of continental crust beneath the Pamir. Spec. Pap. Geol. Soc. Am., 1993. 281, 76

Cattin R., Martelet G., Henry P., et al., Gravity anomalies, crustal structure and thermo-mechanical support of the Himalaya of Central Nepal. Geophys. J. Int, 2001. 147: p. 381-392.

Chen J Y, Zhang Z J, Liu E R. Anisotropic inversion of traveltimes and polarization of wide-angle seismic data using simulated annealing. Journal of Seismic Exploration, 2006. 15(2): p. 101-118

Chen P. Scaling law and its applications to earthquake statistical relations. Tectonophysics, 1989. 166: 53-72

Chen W. P., P. Molnar. Constraints on the seismic wave velocity structure beneath the Tibetan

Plateau and their tectonic implications. Journal of Geophysical Research, 1981. 86, 5937.

Chen Y, Zhang Z J, Tian X B. Complex polarization analysis based on windowed Hilbert transform and its application. Chinese J. Geophys. (in Chinese), 2005. 48(4), 889~895

Christensen N. I., Mooney W.D., Seismic velocity structure and composition of the continental crust: a global view. Journal of Geophysical Research, 1995. 100(No. B7): p. 9761-9788.

Chun, K.Y., T. Yoshii, Crustal structure of the Tibetan Plateau: A surface-wave study by a moving window analysis. Bull. Seismol. Soc. Am., 1977. 67, 735.

Chung S. L., Chua M.F., Zhang Y., et al., Tibetan tectonic evolution inferred from spatial and temporal variations in post-collisional magmatism. Earth-Science Rev., 2005. 68: p. 173-196.

Cotte N., e.a., Determination of the crustal structure in southern Tibet by dispersion and amplitude analysis of Rayleigh waves. Geophys. J. Int, 1999. 138: p. 809-819.

Crampin S. Distinctive particle motion of surface waves as a diagnostic of anisotropic layering. Geophys. J. R. astr. Soc., 1975, 40: 177~186

Dewey, J. F., and Kevin C. A. Burke. Tibetan, Variscan and Precambrian reactivation: Products of continental collision. J. Geol., 1973. 81,683-692

Dewey, J.F., J. M. Bird, Mountain belts and the new global tectonics. Journal of Geophysical Research, 1970. 75: p. 2625.

Dricker I G, Roecker S W. Lateral heterogeneity in the upper mantle beneath the Tibetan plateau and its surroundings from SS-S travel time residuals. J. Geophys. Res., 2002, 107, 2305, doi:10.1029/2001JB000797

Dziewonski, A., S. Bloch, and M. Landisman. A technique for analysis of transient seismic signals, Bull. Seismol. Soc. Am., 1969. 59, 427–444

Ebbing J., B.C., Gotze H. J., Forward and inverse modelling of gravity revealing insight into crustal structures of the Eastern Alps. Tectonophysics, 2001. 337: p. 191-208.

Engdahl E. R., V.d.H.R., Buland R., Global teleseismic earthquake relocation with improved travel times and procedures for depth determination. Bull. Seismol. Soc. Am., 1998. 88: p. 722-743.

Florsch N., Fäh D., Suhadolc P. and Panza G. F. Complete synthetic seismograms for high-frequency multimode SH-waves. Pure and Applied Geophys. 1991. 136: 529-560

Friederich, W. Wave-theoretical inversion of teleseismic surface waves in a regional network: phase-velocity maps and a three-dimensional upper-mantle shear-wave-velocity model for southern Germany. Geophys. J. Int., 1998. 132, 203~225

Friederich, W., Wielandt, E. & Stange, S. Multiple forward scattering of surface waves: comparison with an exact solution and Born single-scattering methods. Geophys. J. Int., 1993. 112, 264~275

Galve A., S.M., Hirn A., et al., Complex images of Moho and variation of Vp/Vs across the Himalaya and South Tibet, from a joint receiver-function and wide-angle-reflection approach. Geophys. Res. Lett, 2002. 29(2182. doi:10.1029/2002GL015611).

Götze, H.J., B. Lahmeyer, Application of three-dimensional interactive modeling in gravity and magnetics. Geophysics, 1988. 53: p. 1096-1108.

Götze, H.J., Uber den Einsatz interaktiver Computeraphik im Rahmen 3-dimensionaler Interpretationstechniken in Gravimetrie und Magnetik. Habil. Schrift, 236 pp., Tech. Univ. Clausthal, ClausthalZellerfeld, Germany, 1984.

Gutenberg B., Richter C. F., Earthquake magnitude, intensity, energy and acceleration. Bull.

Seismol. Soc. Am., 1956b. 46: 105-145

Gutenberg B., Richter C. F., The energy of earthquakes. Q. J. Geol. Soc. London, 1956a. 112: 1-14

Gyorgy Hetenyi, R.Cattin, F. Brunet, et al., Density distribution of the India plate beneath the Tibetan plateau: Geophysical and petrological constraints on the kinetics of lower-crustal eclogitization. Earth and Planetary Science Letters, 2007. 2007(264): p. 226-244.

H. Lyon-Caen, P. Molnar, Gravity anomalies, flexure of the Indian plate and the structure, support and evolution of the Himalaya and Ganga Basin, Tectonics 4 (1985) 513–538.

Hacker, B.R., Abers, G.A. Subduction factory 3: an excel worksheet and a macro for calculating the densities, seismic wave speeds, and H2O content of minerals and rocks at pressure and temperature. Geochem. Geophys. Geosys., 2004. 5(1),Q01005.doi:10.1029/ 2003GC000614

Haines S. S., Klemperer S.L., Brown L., et al., INDEPTH III seismic data: From surface observations to deep crustal processes in Tibet. Tectonics, 2003. 22(1001. doi:10.1029/2001TC001305).

Harrison T. M., P. Copeland, W. S. F. Kidd, and A. Yin, Raising Tibet. Science, 1992. 255, 1663-1670

Hauck M. L., Nelson K.D., Brown L. D., et al., Crustal structure of the Himalayan orogen at ~90°east longitude from Project INDEPTH deep reflection profiles. Tectonics, 1998. 17: p. 481-500.

Helene Lyon-Caen, P.Molnar, Constraints on the structure of the Himalaya from an analysis of gravity anomalies and a flexural model of the lithosphere. Journal of Geophysical Research, 1983. 88(B10): p. 8171-8191.

Henry P., Le Pichon X., Goffe B., Kinematic, thermal and petrological model of the Himalayas: constraints related to metamorphism within the underthrust Indian crust and topographic elevation. Tectonophysics, 1997. 273: p. 31-56.

Herrmann R B, Ammon C J. Computer programs in seismology----surface waves, receiver functions and crustal structure. 2002, http://www.eas.slu.edu/People/RBHerrmann/index.html

Hetenyi, G., Evolution of deformation of the Himalayan prism: from imaging to modelling. PHD thesis, 2007.

Hirn A., e.a., Seismic anisotropy as an indicator of mantle flow beneaht the Himalayas and Tibet. Nature, 1995. 375(571-574).

Holmes, A., Principles of Physical Geology. 2nd ed., Ronald Press, New York, 1965.

Hsu, H.T., Lu, Y., The regional geopotential model in China. Bollettino di geodesia e Scienze Affiini, 1995. LIV(N.2): p. 161-175.

Huang W. C., Ni J.F., Tilmann F., et al., Seismic polarization anisotropy beneath the central Tibetan Plateau. Journal of Geophysical Research, 2000. 105(B12): p. 27979-27989.

Huang Z X, Peng Y, Luo Y, et al. Azimuthal anisotropy of Rayleigh waves in East Asia. Geophysical Research Letters, 2004, 31, doi:10.1029/2004GL020399

Huang Zhong-xian. Surface waves in the laterally heterogeneous earth: a review. Progress in Geophysics (in Chinese), 1995. 10(1): 46~55

Isacks B. L., and M. Barazangi. Geometry of Benioff zones: Lateral segmentation and downwards bending of subducted lithosphere, in Island Arcs, Deep Sea Trenches, and Back-Arc Basins, Maurice Ewing Ser., Vol. 1, edited by M. Talwani and W. C. Pitman, 1977. pp. 99-114, AGU, WashingtonD, .C.

Jimenez-Munt I., M.Fernandez., Jaume Verges, et al., Lithosphere structure underneath the Tibetan Plateau inferred from elevation, gravity and geoid anomalies. Earth and Planetary Science Letters, 2008. 267: p. 276-289.

Jiang M, Xu Z Q, Hirn A, et al. Teleseismic anisotropy and corresponding features of the upper mantle in Tibet Plateau and its neighboring areas. Acta Geoscientia Sinica, 2001, 22(2): 111~116

Jiang M., Galve A., Hirn A., et al., Crustal thickening and variations in architecture from the Qaidam Basin to the QangTang (North-Central Tibetan Plateau) from wide-angle reflection seismology. Tectonophysics, 2006. 412: p. 121-140.

Jin Y., McNutt M.K., Zhu Y. S., Mapping the descent of Indian and Eurasian plates beneath the Tibetan Plateau from gravity anomalies. Journal of Geophysical Research, 1996. 101: p. 11275-11290.

Jull M, Kelemen P.B., On the conditions for lower crustal convective instability. Journal of Geophysical Research, 2001. 106(6423-6446).

Kaila, K.L., H. Narain, Evolution of the Himalaya based on seismo-tectonics and deep seismic soundings. presented at the Himalaya Geology Seminar, sponsor, Geological Survey of India, Dehli, 1976.

Kennett, B.L.N. Engdahl, E.R. & Buland R.. Constraints on seismic velocities in the Earth from travel times. Geophys J Int, 1995. 122, 108-124.

Kennett, B.L.N., 1998. Guided waves in three-dimensional structures, Geophys. J. Int., 133, 159–174

Kind R., Y.X., Saul J., et al., Seismic images of crust and upper mantle beneath Tibet: Evidence of Eurasian plate subduction. Science, 2002. 298(5596): p. 1219-1221.

Kind, R., Ni, J., Zhao, W., et al.. Evidence from earthquake data for a partially molten crustal layer in Southern Tibet. Science, 1996. 274, 1692–1694

Kobayashi R, Nakanishi I. Location of Love-to-Rayleigh conversion due to lateral heterogeneity or azimuthal anisotropy in the upper mantle. Geophysical Research Letters, 1998, 25(7): 1067-1070

Kobayashi R. Polarization anomalies of Love waves observed in and around Japan. Earth Planets Space, 2002, 54: 357~365

Kosarev G., Kind R., Sobolev S. V., Seismic evidence for a detached Indian lithospheric mantle beneath Tibet. Science, 1999. 283(5406): p. 1306-1309.

Lander A V. Recording identification and measurements of surface wave parameters In Seismic surface waves a laterally inhomogeneous Earth. Keilis-Borok, V. I. (Ed.), Kluwer Publ., Dordrecht, 1989, 129-182

Laske G. Global observation of off-great circle propagation of long period surface waves. Geoph. J. Int. 1995, 123: 245-259

Le Fort, P., Himalaya: The collided range. Present knowledge of the continental arc. Am. J. Sci., 1975. 275A, 1.

Le Pichon, X., Henry, P., Goffé, B. Uplift of Tibet: from eclogites to granulites. Tectonophysics, 1997. 273, 57–76

Levin V, Park J, Lucente F P, et al. End of subduction in northern Apennines confirmed by observations of quasi-Love waves from the great 2004 Sumatra-Andaman earthquake. Geophysical Research Letters, 2007, 34, doi:10.1029/2006GL028860

Levin V, Park J, Margheriti L, et al. Structure and texture of the upper mantle beneath Northern Apennines: evidence from quasi-Love waves. Geophysical Research Abstracts, 2006, 8, 1607-7962 /gra / EGU06-A-05413

Levin V., Park J., Quasi-Love phases between Tonga and Hawaii: Observations, simulations, and explanations, J. Geophys. Res, 1998. 103, 24321-24331

Levshin, A.L., Berteussen, K.-A., 1979. Anomalous propagation of surface waves in the Barents Sea as inferred from NORSAR recordings. Geoph. J. R. astr. Soc., 56, 97-118.

Levshin A L., L Ratnikova and J Berger. Peculiarities of surface wave propagation across Central Eurasia. Bull Seism. Soc. Am., 1992, 82: 2464-2493

Levshin A L., M H Ritzwoller and L I Ratnikova. The nature and cause of polarization anomalies of surface waves crossing northern and central Eurasia. Geophys. J. Int., 1994, 117: 577-590

Levshin, A., H. Ratnikova, and J. Berger. Peculiarities of surface-wave propagation across central Eurasia, Bull. Seismol. Soc. Am., 1992. 82,2464–2493

Li Q S. The lithosphere structure of continental-continenatl collision in Tibet studied by seismology. PHD thesis. 2003

Liu E R, Queen J H, Zhang Z J. Simulation of multiple scattering of elastic waves by spatially distributed inclusions. Sciences in China (Series E), 2000. 43(4), 387-394

Liu K, Zhang Z J, Hu J F. Frequency band-dependence of S-wave splitting in China mainland and its implications. Science in China(Series D), 2001, 44（7）: 659~665

Lu Q T, Jiang M, Ma K Y, et al. The deformation characteres of Qinghai-Xizang lithosphere: implication from earthquake mechanism and seismic anisotropy. Geological Review, 1997, 43(4): 337~346

Lu Z W, Gao R, Li Q S et al. Geophysical survey and geodynamic study of crust and upper mantle in the Qinghai-Tibet Plateau. Chinese J Geophys (in Chinese), 2006. 49(3): 753-770.

Maggi A., Jackson J.A., Mckenzie D., et al., Earthquake focal depths, effective elastic thickness, and the strength of the continental lithosphere. Geology, 2000. 28(6): p. 495-498.

Makovsky Y., Klemperer S., Huang L. et al.. Stuctural elements of the southern Tethyan Himalaya crust from wide-angle seismic data. Tectonics, 1996. 15(5): 997-1005

Maupin, V. A multiple-scattering scheme for modelling surface wave propagation in isotropic and anisotropic three-dimensional structures. Geophys. J. Int., 2001. 146, 332~348

McLennan, S., Continental crust. In: W.A. Nierenberg, Encyclopedia of Earth System Science. Academic Press, San Diego, 1992. 1: p. 581-592.

McNamara D E, Owens T J, Silver P G, et al. Shear wave anisotropy beneath the Tibetan Plateau. Journal of Geophysical Research, 1994, 99: 13655~13665

McNamara D. E., Walter W.R., Owens T. J., et al., Upper mantle velocity structure beneath the Tibetan Plateau from Pn travel time tomography. Journal of Geophysical Research, 1997. 102: p. 493-505.

Meissner R., Tilmann F., Haines S., About the lithospheric structure of central Tibet, based on seismic data from the INDEPTH III profile. Tectonophysics, 2004. 380: p. 1-25.

Minster, J.B., T. H. Jordan, Present-day plate motions. Journal of Geophysical Research, 1978. 83, 5331.

Mitra S., Priestley K., Bhattacharyya A. K., et al., Crustal structure and earthquake focal depths beneath northeastern India and southern Tibet. Geophys. J. Int, 2005. 160: p. 227-248.

Molnar, P. A review of geophysical constraints on the deep structure of the Tibetan plateau, the

Himalaya and the Karakoram, and their tectonic implications. Philos. Trans. R. Soc. 1988. London, A326, 33-88

Molnar, P., W. P. Chen, T. J. Fitch et al., Structure and tectonics of the Himalaya: A brief summary of relevant geophysical observations. Collog. Int. C. N. R. S., 1977. 268, 463.

Monsalve G., S.A., Rowe C., et al., Seismic structure of the crust and the upper mantle beneath the Himalayas: Evidence for eclogitization of lower crustal rocks in the Indian Plate. Journal of Geophysical Research, 2008. 113(doi:10.1029/2007JB005424).

Monsalve G., Sheehan A., Schulte-Pelkum V., et al., Seismicity and one-dimensional velocity structure of the Himalayan collision zone: Earthquakes in the crust and upper mantle. Journal of Geophysical Research, 2006. 111(B10), B10301.

Nábělek, J.L., Vergne, J., Hetényi, G., 2005. Project Hi-CLIMB: a synoptic view of the Himalayan collision zone and Southern Tibet. EoS Trans. AGU 86 (52) Fall Meet. Suppl., Abstract T52A-02.

Nelson K. D., Zhao W., Brown L. D., et al., Partially molten middle crust beneath southern Tibet: synthesis of project INDEPTH results. Science, 1996. 274: p. 1684-1688.

Ni J. and M. Barazangi. Seismotectonics o f the Himalayan collision zone: Geometry of the underthrusting Indian Plate beneath the Himalaya. J. Geophys Res., 1984. 89, 1147-1163

Oda H, Onishi S. The effect of regional variation of lattice preferred orientation on surface waveforms. Geophys. J. Int., 2001, 144: 247~258

Owens T. J., Zandt G., Implications of crustal property variations for models of Tibetan plateau evolution. Nature, 1997. 387: p. 37-43.

Panza G. F. Synthetic seismograms: the Rayleigh waves modal summation. J. Geophysics, 1985. 58: 125-145.

Panza G. F., Romanelli F. and Vaccari, F. Seismic wave propagation in laterally heterogeneous anelastic media : Theory and applications to seismic zonation, Advances in Geophysics, Academic Press, 2000. 43, 1-95

Panza G. F., Doglioni C., Levshin A. Asymmetric ocean basins. Geology. 2010, 38(1): 59-62

Park J, Yu Y. Anisotropy and coupled free oscillations: simplified models and surface wave observations. Geophys. J. Int., 1992, 110: 401~420

Park, J. Synthetic seismograms from coupled free oscillations: effects of lateral structure and rotation. J.Geophys.Res., 1986, 91: 6441~6464

Paulssen H., Levshin A L., Lander A V. Snieder R. Time and frequency dependent polarization analysis: anomalous surface wave observations in Iberia. Geoph. J. Int., 1990, 103: 483-496

Pei S P, Zhao J, Sun Y, et al. Upper mantle seismic velocities and anisotropy in China determined through Pn and Sn tomography. J. Geophys. Res., 2007, 112, doi:10.1029/2006JB004409

Powell C. M. and P. J. Conaghan. Plate tectonics and the Himalayas. Earth Planet. Sci. Lett., 1973. 20, 1-12

Powell, C.M., P. J. Conaghan, Plate tectonics and the Himalayas. Earth and Planetary Science Letters, 1973. 20, 1.

R. S. Rajesh, D.C.Mishra. Admittance analysis and modelling of satellite gravity over Himalayas-Tibet and its seismogenic correlation. CURRENT SCIENCE, 2003. 84(2): p. 224-230.

Ribe N. M., Christensen U. R. Three-dimensional modeling of plume-lithosphere interaction. J. Geophys. Res, 1994. 99, 669

Rudnick R. L., Fountain D.M., Nature and composition of the continental crust: a lower crustal

perspective. Rev. Geophys., 1995. 33: p. 267-309.
Saito, M. Disper80: a subroutine package for the calculation of seismic normal mode solutions. Seismological Algorithms, 1988. 293-319
Spain M., Hirn A., Seismic structure and evidence for eclogitization during the Himalayan convergence. Tectonophysics, 1997. 273: p. 1-16.
Schmidt, S., H. J. Götze, Interactive visualization and modification of 3D models using GIS functions. Phys. Chem. Earth, 1998. 23: p. 289-296.
Schulte-Pelkum V., Monsalve G., Sheehan A., et al., Imaging the Indian subcontinent beneath the Himalaya. Nature, 2005. 435(7046): p. 1222-1225.
Shapiro, N. M., M. H. Ritzwoller. Monte-Carlo inversion for a global shear velocity model of the crust and upper mantle. Geophys. J. Int., 2002. 151, 88-105
Snieder, R. 3-D linearized scattering of surface waves and a formalism for surface wave holography. Geophys. J. R. astr. Soc., 1986. 84, 581~605
Sun W. (1989) Bouguer gravity anomaly map of the P. R. of China, Chinese Academy of Geoexploration, Beijing.
Takeuchi H. and Saito M. Seismic surface waves, Methods of computational physics. Academic Press, New York, 1972. 11, 217-295
Tanimoto T. The azimuthal dependence of surface wave polarization in a slightly anisotropic medium. Geophys. J. Int., 2004, 156: 73~78
Teng, J., et al., Characteristic of the geophysical fields and plate tectonics of the Qinghai-Xizang Plateau and its neighboring regions. Acta Geophys. Sinica, 1980a. 23, 254.
Teng, J., et al., Explosion seismic study for velocity distribution and structure of the crust and upper mantle from Damzung to Yadong of Xizang Plateau. Proceedings of Symposium on Qinghai-Xizang Plateau (Abstracts), 1980b. P. 81, Academia Sinica, Beijing.
Tilmann F., Ni J., Team I. I. S., Seismic imaging of the downwelling Indian lithosphere beneath central Tibet. Science, 2003. 300(5624): p. 1424-1427.
Tiwari V. M., V. Rao, Mishra D. C., et al., Crustal structure across Sikkim, NE Himalaya from new gravity and magnetic data. Earth and Planetary Science Letters, 2006. 247: p. 61-69.
Toksoz, M.N., A. Hsui, Crustal evolution and thermal state of Tibet. Proceedings of Symposium on Qinghai-Xizang Plateau (Abstracts), 1980. p. 91, Academia Sinica, Beijing.
Trampert J., Deschamps J., Resovsky J., et al., Probabilistic Tomography Maps Chemical Heterogeneities Throughout the Lower Mantle. Science, 2004. 306: 853 – 856.
Unsworth M., Wei W., Jones A. G., et al., Crustal and upper mantle structure of northern Tibet imaged with magnetotelluric data. Journal of Geophysical Research, 2004. 109, B02403(doi:10.1029/2002JB002305).
Van der Lee, S. Observations and origin of Rayleigh-wave amplitude anomalies. Geophys. J. Int., 1998. 135, 691~699
Villasenor A., Ritzwoller M.H., Levshin A. L., et al., Shear velocity structure of central Eurasia from inversion of surface wave velocities. Phys. Earth Planet. Inter., 2001. 123: p. 169-184.
Wang, P., P. Molnar, Constraints on the seismic wave velocity structure beneath the Tibetan Plateau. Proceedings of Symposium on Qinghai-Xizang Plateau (Abstracts), 1980. p. 84, Academia Sinica, Beijing.
Wei W., Unsworth M., Jones A., et al., Detection of widespread fluids in the Tibetan crust by magnetotelluric studies. Science, 2001. 292: p. 716-718.

Wittlinger G., Farra V., Vergne J., Lithospheric and upper mantle stratifications beneath Tibet: New insights from Sp conversions. Geophys. Res. Lett, 2004. 31(19): p. L19615.

Wittlinger G., Vergne J., Tapponnier P., Teleseismic imaging of subducting lithosphere and Moho offsets beneath western Tibet. Earth and Planetary Science Letters, 2004. 221(1-4): p. 117-130.

Woodhouse J H, Dahlen F A. The effect of a general aspherical perturbation on the free oscillations of the Earth. Geophys. J. R. astr. Soc., 1978, 53: 335~354

Wu Q, Zeng R, Zhao W. Oblique tectonic and continental-continental collision in the upper mantle of Himalaya-Tibet plateau. Science in China(Series D), 2004, 34(10): 910~925

Wu Q, Zeng R. The crustal structure of Qinghai-Xizang Plateau inferred from broadband teleseismic waveform. Chinese J. Geophys. (in Chinese), 1998, 41(5): 669~679

Xiong S. B., Liu H.B., Crustal structure in the west Tibetan plateau. Chinese Science Bulletin (in Chinese), 1997. 42(12): p. 1309-1312.

Xiong S. B., Teng J.W., Yin Z. X., The thickness of the crust and undulation of discontinuity in Xizang(Tibet) plateau. Chinese J. Geophys. (Acta Geophysica Sinica) (in Chinese), 1985. 28: p. 16-27.

Y. Jin, M.K. McNutt, Y.S. Zhu, Mapping the descent of Indian and Eurasian plates beneath the Tibetan Plateau from gravity anomalies, J. Geophys. Res. 101 (1996) 11275–11290.

Yang X, Jin Z, Ma J, et al. Genesis of SKS splitting in the north-central Qinghai-Xizang Plateau: melt alignment enhanced lithosphere anisotropy. Chinese J. Geophys. (in Chinese), 2002, 45(6): 821~831

Yu Y, Park J, Wu Francis. Mantle anisotropy beneath the Tibetan Plateau: evidence from long-period surface waves. Physics of Earth and Planetary Interiors, 1995, 87: 231~246

Yu Y, Park J. Hunting for azimuthal anisotropy beneath the Pacific Ocean region. Journal of Geophysical Research, 1994, 99: 15399~15421

Yu Y, Park J. Upper mantle anisotropy and coupled-mode long-period surface waves. Geophys. J. Int., 1993, 114: 473~489

Zhang J, Ma Z J. East-West Segmentation of the Tibetan Plateau and Its Implication. Acta Geologica Sinica, 2004, 78(2): 218~228

Zhang P Z, Shen Z K, Wang M, et al. Continuous deformation of the Tibetan Plateau from global positioning system data. Geology, 2004, 32(9): 809~812

Zhang S F, Zhang Z. Surface wavefield and dynamic analysis for three-dimensional abnormal structures with homogenous background velocity model. Chinese J. Geophys. (in Chinese), 2008, 51(4): 1180~1187

Zhang Z J, Klemperer S.L., West-east variation in crustal thickness in northern Lhasa block,central Tibet,from deep seismic sounding data. J Geophys Res, 2005(110): p. doi:10.1029/ 2004JB003139.

Zhang Z J, Li Y K, Teng J W et al. Crustal structure of seismic velocity in southern Tibet and east-westward escape of the crustal. Sciences in China (Series D), 2002. 32(10), 793-798

Zhang Z J, Li Y K, Wang G J, et al. East-west crustal structure and “down-bowing” Moho under the northern Tibet revealed by wide-angle seismic profile. Science in China(Series D), 2002, 45（6）: 550~558

Zhang Z J, Teng J W, Li Y K, et al. Crustal structure of seismic velocity in southern Tibet and east-westward escape of the crustal material. Science in China(Series D), 2004, 47（6）: 500~506

Zhang Z. J., Teng J.W., Li Y. K., et al, Crustal velocity structure and eastward escaping of crustal material in the southern Tibet--An example revealed by wide-angle seismic profile between Peikucuo and Pumoyongcuo. Science in China(Series D) (in Chinese), 2002. 32(10): p. 793-798.

Zhao W. J., Mechie J., Brown L. D., et al., Crustal structure of central Tibet as derived from INDEPTH wide angle seismic data. Geophys. J. Int., 2001. 145: p. 486-498.

Zhao W., M.J., Brown L. D., et al., Crustal structure of central Tibet as derived from project INDEPTH wide-angle seismic data. Geophys. J. Int, 2001. 145: p. 486-498.

Zhao L S., Sen M., Stoffa P. et al., Application of very fast simulated annealing to the determination of the crustal structure beneath Tibet. Geophys. J. Int, 1996. 125: p. 355-370.

Zhang Z J, Zhang X, Badal J. Composition of the crust beneath southeastern China derived from an integrated geophysical data set. J. Geophys. Res., 2008, doi:10.1029/2006JB004503